


8-2018

# High-Sn-content GeSn Alloy towards Room-temperature Mid Infrared Laser

Wei Dou

*University of Arkansas, Fayetteville*

Follow this and additional works at: <http://scholarworks.uark.edu/etd>

 Part of the [Electromagnetics and Photonics Commons](#), and the [Electronic Devices and Semiconductor Manufacturing Commons](#)

---

## Recommended Citation

Dou, Wei, "High-Sn-content GeSn Alloy towards Room-temperature Mid Infrared Laser" (2018). *Theses and Dissertations*. 2849.  
<http://scholarworks.uark.edu/etd/2849>

This Dissertation is brought to you for free and open access by ScholarWorks@UARK. It has been accepted for inclusion in Theses and Dissertations by an authorized administrator of ScholarWorks@UARK. For more information, please contact [scholar@uark.edu](mailto:scholar@uark.edu), [ccmiddle@uark.edu](mailto:ccmiddle@uark.edu).

High-Sn-content GeSn Alloy towards Room-temperature Mid Infrared Laser

A dissertation submitted in partial fulfillment  
of the requirements for the degree of  
Doctor of Philosophy in Engineering

by

Wei Dou  
Shandong University  
Bachelor of Science in Physics, 2010  
University of Chinese Academy of Sciences  
Master of Science in Electrical Engineering, 2013

August 2018  
University of Arkansas

This dissertation is approved for recommendation to the Graduate Council.

---

Shui-Qing (Fisher) Yu, Ph.D.  
Dissertation Director

---

Gregory J. Salamo, Ph.D.  
Dissertation Co-Director

---

Simon S. Ang, Ph.D.  
Committee Member

---

Hameed A. Naseem, Ph.D.  
Committee Member

## **Abstract**

Si photonics is a rapidly expanding technology that integrates photonic circuits onto a Si substrate. The integration of Si electronics and photonics has been a successful technology for a wide range of applications. Group-IV alloy GeSn has drawn great attentions as a complementary metal–oxide–semiconductor compatible optoelectronic material for Si photonics. The devices based on GeSn alloy could be monolithically integrated into well-established and high-yield Si integrated circuits, which is favorable for chip-scale Si photonics featuring smaller size, lower cost, and higher reliability.

The relaxed GeSn with high material quality and high Sn composition is highly desirable to cover mid-infrared wavelength. A systematic study of GeSn strain relaxation mechanism and its effects on Sn incorporation during the epitaxy via chemical vapor deposition was conducted. It was discovered that Sn incorporation into Ge lattice sites is limited by high compressive strain rather than historically acknowledged chemical reaction dynamics, which was also confirmed by Gibbs free energy calculation. Following the discovered growth mechanism, a world-record Sn content of 22.3% was achieved. Even higher Sn content could be obtained if further continuous growth with the same recipe is conducted.

The GeSn laser with higher Sn content is highly desired to cover longer wavelength in mid-infrared. This work demonstrated optically pumped edge-emitting GeSn lasers under two different pumping lasers with 1064 and 1950 nm wavelengths. The device structure featured Sn compositional graded with the maximum Sn content of 22.3%. Under the 1950 nm pumping laser, the GeSn laser achieved the world-record near room temperature lasing (270 K). The corresponding lasing wavelength has been extended up to 3442 nm, an unprecedented GeSn lasing wavelength so far in the world.

The GeSn/GeSn/GeSn single and double quantum wells were also investigated to further improve laser performance. The unintentional Ge interlayer between barrier and well region of QW structure was removed by introducing the GeSn with variable Sn content as the buffer layer. As a result, the QW structure was demonstrated as the true type-I and direct bandgap structure, which is advantageous for the optoelectronic devices.

## **Acknowledgements**

Firstly, I would like to give my sincere gratitude to my advisor, Dr. Shui-Qing (Fisher) Yu for his expertise, support, and guidance of the research and my dissertation. During my five years of doctoral research, Dr. Yu provided tremendous opportunities allowing me to grow from a research beginner to a research scientist. He also inspired me in all the aspects of my studies and in my experiments. His enthusiasm and dedication on the research has encouraged me to keep learning not only in the research field but also in other aspects of life. The experience and knowledge I gained during my PhD study is a priceless treasure that I will cherish for my whole life.

Secondly, my profound gratitude goes to my dissertation committee members: Dr. Gregory J. Salamo, Dr. Hameed A. Naseem, and Dr. Simon Ang. Without their endless encouragement and insightful comments, it would have been impossible for me to keep my dissertation on the right track. Your patience and kindness is a great honor and a precious memory for me.

I also hugely appreciate Dr. Mourad Benamara who shared the marvelous expertise of TEM with me. He is dedicated to the role as a TEM specialist and thoroughly trained me in TEM skills. I also give special thanks to Dr. Andrian Kuchuk for offering his immense knowledge of XRD on my dissertation. The time I spent with him was delightful and wonderful.

My appreciation extends to Joe Margetis and Dr. John Tolle from the ASM Company for the CVD growth of samples. Special mention goes to Dr. Baohua Li and Dr. Wei Du for their help in paper writing and discussions. I also would like to thank my CVD growth team members: Perry Grant, Bader Alharthi, and Joshua Grant for their countless help during the CVD growth and machine maintenance. It was a great pleasure to work with them. I also appreciate the following colleagues: Liang Huang, Aboozar Mosleh, Seyed Amir Ghetmiri, Sattar Al-Kabi, Yiyin Zhou, Thach Pham,

Huong Tran, Grey Abernathy for their support. I spent a wonderful time working on experiments with them throughout my dissertation.

Finally, from the bottom of my heart, I give huge appreciation to my lovely wife Lihua (Rita) Yang. The journey of PhD study would not have been possible without her support both emotionally and financially. I deeply appreciate all the sleepless night she sacrificed accompanying with me. As a soul mate, she encouraged me not to give up under any circumstances. She also believed in me and wanted the best of me. I would also thank my other families for their endless support of my education. Their encouragement has been vital as I pursue my dreams.

The work in this dissertation was partially supported by Air Force SBIR Phase I and Phase II Projects " Epitaxial Technologies for SiGeSn High Performance Optoelectronics Devices" under contract numbers FA9550-14-C-0044 and FA9550-16-C-0016 (PI: Dr. Baohua Li from Arktonics LLC and Program manager: Dr. Gernot S. Pomrenke from Air Force Office of Scientific Research). Any opinions, findings, and conclusions or recommendations expressed in this material are those of the author and do not necessarily reflect the views of the Air Force. The work is also supported by the National Science Foundation (NSF) under contract number DMR-1149605. Any opinions, findings, and conclusions or recommendations expressed in this material are those of the author and do not necessarily reflect the views of the NSF. Support is also appreciated from Air Force Office of Scientific Research (AFOSR) under contract number FA9550-14-1-0205. Any opinions, findings, and conclusions or recommendations expressed in this material are those of the author and do not necessarily reflect the views of the AFOSR. Final National Aeronautics and Space Administration Established Program to Stimulate Competitive Research (NASA EPSCoR) under contract number NNX15AN18A. Any opinions, findings, and conclusions or

recommendations expressed in this material are those of the author and do not necessarily reflect the views of the NASA.

## Table of Contents

Chapter 1. Introduction.....	1
1.1. Motivation.....	1
1.2. Growth technology for GeSn.....	4
1.3. Growth mechanism of GeSn.....	7
1.4. Progress of GeSn laser.....	12
Chapter 2. High quality Ge and GeSn by UHV-CVD.....	15
2.1. Ultra-high vacuum chemical vapor deposition (UHV-CVD).....	15
2.2. Two-step Ge buffer on Si.....	16
2.2.1. Ge growth on Si.....	16
2.2.2. Raman characteristics.....	17
2.2.3. Photoluminescence (PL) characteristics.....	19
2.2.4. Etch pit method.....	25
2.3. Hot-filament-assisted CVD growth of Ge on Si.....	26
2.4. Plasma-enhanced CVD growth of GeSn on Si.....	31
2.5. GeSn growth on Ge buffer.....	37
Chapter 3. Band structure of GeSn.....	41
3.1. K.P method for GeSn band structure.....	41
3.1.1. Kane Model.....	43
3.1.2. Luttinger-Kohn Model.....	44
3.2. Temperature-dependent bandgap of GeSn.....	47
3.3. Strain effects on the GeSn band structure.....	50
Chapter 4. High Sn-content GeSn by RP-CVD.....	55
4.1. Reduced-pressure chemical vapor deposition (RP-CVD).....	55
4.2. Growth methodology of high Sn-content GeSn.....	56
4.3. Sample characterization.....	58
4.3.1. Transmission electron microscopy (TEM) and Secondary ion mass spectrometry (SIMS).....	59
4.3.2. Photoluminescence (PL) characterization.....	61
4.3.3. Energy Dispersive X-ray Spectroscopy (EDX).....	62
Chapter 5. Strain relaxation analysis.....	65
5.1. Critical thickness analysis.....	66



5.2.	Calculations of elastic energy, effective stress, strain, and relaxation.....	67
5.3.	Dislocation configuration at GeSn/Ge interface .....	69
5.4.	Self-organized dislocation network.....	74
5.5.	Plan-view transmission electron microscopy (TEM) analysis.....	77
Chapter 6.	Gibbs free energy calculation .....	78
6.1.	Gibbs free energy calculation.....	78
6.2.	Binodal and spinodal curves .....	80
6.3.	Interplay between strain and Sn composition .....	81
Chapter 7.	High Sn-content GeSn Edge Emitting Laser .....	82
7.1.	Sample growth.....	82
7.2.	Structural material characterization .....	83
7.3.	The bandgap diagram calculation .....	85
7.4.	Photoluminescence (PL) measurement .....	86
7.5.	Optically pumped GeSn edge emitting laser.....	89
7.6.	Room temperature GeSn laser.....	92
Chapter 8.	Advanced GeSn/GeSn/GeSn Quantum Well (QW) .....	99
8.1.	Initial GeSn/GeSn/GeSn QW structure.....	99
8.1.1.	Transmission electron microscopy (TEM) characterization.....	101
8.1.2.	X-ray diffraction (XRD) analysis .....	102
8.1.3.	Photoluminescence (PL) characterization.....	104
8.1.4.	Discussion of optical properties of QW .....	108
8.2.	Optimized GeSn/GeSn/GeSn QW structure .....	110
8.2.1.	Strain balanced growth of QW .....	110
8.2.2.	Secondary ion mass spectrometry (SIMS) analysis.....	112
8.2.3.	PL measurement.....	114
8.2.4.	Band diagram calculation .....	115
Chapter 9.	Summary and Future work.....	116
9.1.	Summary .....	116
9.2.	Future work .....	120
References	.....	122
Appendix A	.....	122
Appendix B	.....	134
Appendix C	.....	136

Appendix D.....	138
Appendix E .....	139
Appendix F: All Publications Published, Submitted and Planned.....	140

## List of Figures

Figure 1.1 The schematic diagram of a complete set of silicon photonics transceiver. ....	1
Figure 1.2 (a) Band structure of bulk Ge shows the indirect bandgap characteristics. (b) GeSn with Sn content more than 8% exhibits the direct bandgap characteristics. (c) The transition between indirect and direct energy bandgap of GeSn as a function of Sn composition. ....	3
Figure 1.3 The overview of major achievements of GeSn growth since GeSn was first mentioned. Two growth techniques of MBE and CVD were mainly employed in the history of GeSn epitaxy. ....	5
Figure 1.4 Schematic mechanism of hydride elimination pathway describing GeH <sub>4</sub> chemisorption on the Ge (001) surface. ....	8
Figure 1.5 The possible reaction pathways of the SnCl <sub>4</sub> thermal decomposition. ....	9
Figure 1.6 The possible reaction pathways of the Ge <sub>2</sub> H <sub>6</sub> thermal decomposition. ....	11
Figure 1.7 The timeline of the development of laser of GeSn since 2013. ....	13
Figure 2.1 (a) The overview of customer-designed cold wall UHV-CVD system. (b) The schematic diagram of gas mixing system. ....	16
Figure 2.2 (a) The second step temperature V.S. the average growth rate. (b) The growth rate as a function of dilution ratio of GeH <sub>4</sub> and Ar. During the growth GeH <sub>4</sub> acts as a precursor of Ge buffer while Ar was used as the carrier gas. ....	17
Figure 2.3 Ge-Ge LO Raman shift and Si-Si TO Raman shift with different thickness of Ge film on Si. ....	18
Figure 2.4 The schematic diagram of PL mechanism of bulk Ge. The pathways of carriers were drawn on the Ge band structure. ....	19
Figure 2.5 The mechanism of carrier recombination in the presence of Shockley-Read-Hall (SRH) recombination centers. ....	20
Figure 2.6 Power-dependent PL spectra of (a) bulk Ge and (b) two step Ge films with thicknesses of 1 μm. (c) The peak intensity of sample 1,2 and bulk Ge as the function of pumping power. .	23
Figure 2.7 (a) Temperature- dependent PL measurements of the two step Ge sample on Si. (b) The PL spectra at logarithmic scale at different temperatures. (c) The corresponding integrated PL intensity and the peak positions of direct bandgap as a function of temperature. ....	25
Figure 2.8 The SEM Images of etch-pit method for Ge film on Si at different areas. ....	25
Figure 2.9 The schematic diagram of hot-filament assisted CVD. ....	26
Figure 2.10 (a) The Ge thickness V.S growth temperature using HFA-CVD growth under different power supplies of hot filament. (b) The pressure-dependent growth thickness of Ge under different power supplies of hot filament and dilution ratio of precursors. (c) The Ge thickness V.S dilution ratio between GeH <sub>4</sub> and Ar under different power supplies and growth pressures. ....	28
Figure 2.11 (a) The Raman spectra of 20 nm-thickness Ge on Si at three spots of substrate. (b) The Raman spectra of 52 nm-thickness Ge on Si. ....	30

Figure 2.12 (a) The schematic diagram of PE-CVD system. (b) The generation of plasma between cathode plate and wafer in the CVD process chamber. (c) The grown GeSn on Si wafer after PE-CVD growth. Different probing spots were marked on the wafer.....	32
Figure 2.13 Room temperature PLs of (a) sample 1 and (b) sample 2 at different probing spots on the wafer.....	34
Figure 2.14 The rock curves of XRD measurements at spots III and IV of (a) sample 1 and (b) sample 2. ....	35
Figure 2.15 Raman spectroscopy at the spots of I, II and III of sample 2. ....	37
Figure 2.16 (a) The Ellipsometry measurements at spots I and III of sample 2. (b) The data fitting of direct absorption coefficient for direct bandgap energy at the spot III of sample 2.....	37
Figure 2.17 The room-temperature PL spectra of GeSn and bulk Ge reference. ....	39
Figure 2.18 The data fitting of direct absorption coefficient for direct bandgap energy.....	39
Figure 2.19 The rocking curve of XRD along (004) plane for GeSn sample. ....	40
Figure 3.1 (a) parabolic model of two bands. (b) Kane model of four core bands. (c) Luttinger-Kohn model of the bands classified into A and B. ....	42
Figure 3.2 The band structure of the unstrained (a) bulk GeSn, (b) $\text{Ge}_{0.95}\text{Sn}_{0.05}$ and (c) $\text{Ge}_{0.85}\text{Sn}_{0.15}$ at room temperature. ....	47
Figure 3.3 The bandgap energy as the function of Sn concentration at the temperature of 300 and 10 K.....	48
Figure 3.4 The band structure of unstrained $\text{Ge}_{0.9}\text{Sn}_{0.1}$ at (a) room temperature (300 K) and (b) 10 K.....	50
Figure 3.5 The schematic diagram of (a) compressive strain (b) no strain and (c) tensile strain for the epitaxial growth.....	51
Figure 3.6 The band structure comparison of Ge bulk and compressive strained $\text{Ge}_{0.9}\text{Sn}_{0.1}$ at room temperature. ....	53
Figure 3.7 The energy change of $\text{Ge}_{0.9}\text{Sn}_{0.1}$ band edge as a function of compressive strain.....	54
Figure 3.8 The comparison of band structure between (a) unstrained and (b) compressively strained $\text{Ge}_{0.9}\text{Sn}_{0.1}$ at room temperature.....	55
Figure 4.1 The Epsilon® 2000 Plus RPCVD system from ASM company. ....	56
Figure 4.2 (a) Dark field TEM image of sample A. (b) SIMS of sample A. (c) TEM Image of sample D. (d) SIMS of sample D. (e) TEM image of sample E. (f) SIMS of sample E.....	59
Figure 4.3 (a) Temperature-dependent photoluminescence (PL) of sample E from 10 to 300 K. The insert: temperature-dependent peak shift. (b) The integrated PL intensity and The full width of half maximum (FWHM). ....	61
Figure 4.4 EDX-STEM results show Sn composition curves (a), (c), (e), (g), and (i) as function of scanning depth for samples A, B, C, D, and E, respectively. Bright fields of cross sectional TEM images of sample A, B, C, D, and E are shown in (b), (d), (f), (h), and (j), respectively. ....	63

Figure 4.5 The symmetric $2\theta$ - $\omega$ scans (a), (c), and (e) along (004) plane for sample A, D, and E, respectively. RSMs of XRD (b), (d), and (f) at the asymmetric (224) for sample A, D, and E, respectively. ....	65
Figure 5.1 Critical thicknesses calculation for GeSn on Ge buffer based on Matthews and Blakeslee (M-B) model and People and Bean (P-B) model. ....	66
Figure 5.2 (a) Elastic energy and effective stress of Sample A were plotted as a function of thickness. (b) Strain and relaxation as a function of thickness were drawn. ....	69
Figure 5.3 (a) The HRTEM image at the GeSn/Ge interface of sample B. (b1) Zoomed-in image of area A. (b2), (b3) The inverse FFT images. (c1) Zoomed-in image of area B. (c2), (c3) The Inverse FFT images. ....	70
Figure 5.4 (a) Zigzagged intrinsic stacking faults at the GeSn/Ge interface of sample B. (b) Zoomed-in TEM image of area A. The insert is inverse FFT images. (c) Thompsons tetrahedron diagram. (d) In zoomed-in image of area B. (e) The glide motion of top atoms. ....	72
Figure 5.5 (a) Dark field TEM images of sample B. (a1) Zoom-in TEM image of area A. (b) The schematic diagram of half loop nucleation. (c) The formation of Lomer dislocation. ....	75
Figure 5.6 (a) Bright field plan-view TEM image of GeSn/Ge interface. (b) Plan view TEM image of the top GeSn layer. ....	77
Figure 6.1 (a) Plots of Gibbs free energy $\Delta G_0 = 0$ and $\Delta G_s = 0$ . (b) Gibbs free energy plot at $T=400^\circ\text{C}$ with ( $G_s$ ) and without strain ( $G_0$ ). ....	79
Figure 6.2 Temperature-composition ( $T - x$ ) phase diagram of GeSn. ....	80
Figure 7.1 Cross sectional dark field TEM images of (a) sample A and (d) sample B viewed from 110 direction. SIMS plots as a function of depth for (b) sample A and (e) sample B. RSM contour plots of (c) sample A and (f) sample B. ....	85
Figure 7.2 (a) SIMS profile of sample A. (b) The band diagram calculation of sample A with Sn compositional graded GeSn structure. ....	86
Figure 7.3 (a1), (a2) Temperature-dependent PL spectra. (b) The integrated PL intensity and peak position as a function of temperature. (c) Power-dependent PL spectra at 10 K. Inset: Blue shift of wavelength with increasing power density. (d) Band filling effect in triangular potential model. Inset: calculation of spontaneous emission in triangular potential well. ....	88
Figure 7.4 The schematic diagram of GeSn laser devices and optically pumped lasing setup. ...	89
Figure 7.5 The temperature-dependent L-L curves of the edge emitting devices for (a) sample A-5 $\mu\text{m}$ and (b) sample B-5 $\mu\text{m}$ . Inset: characteristic temperature $T_o$ was extracted as 70 K. Lasing spectra at different temperature for devices of (c) sample A-5 $\mu\text{m}$ and (d) sample B-5 $\mu\text{m}$ . kkkk	91
Figure 7.6 Comparison of Lasing and PL spectra for sample A-5 $\mu\text{m}$ at temperature of 77 K. Inset: The pattern of $\text{TE}_0$ mode at the lasing wavelength of 2900 nm. ....	92
Figure 7.7 (a) The temperature-dependent L-L curves of sample B-20 $\mu\text{m}$ devices. The 1064 nm pumping laser was utilized. (b) The lasing spectra at the temperature of 200K. The inset: Zoomed-in lasing spectra. ....	94

Figure 7.8 The L-L curve of sample B-20 $\mu$ m at the temperature of 200 K. Note: The logarithmic scales of both x and y axis .....	95
Figure 7.9 (a) The temperature-dependent L-L curves of sample A-4 $\mu$ m devices. (b) The temperature-dependent L-L curves of sample A-20 $\mu$ m devices.....	96
Figure 7.10 (a) The temperature-dependent lasing spectra of sample A-4 $\mu$ m devices. (b) The temperature-dependent lasing spectra of sample A-20 $\mu$ m devices.....	96
Figure 7.11 (a) The temperature-dependent L-L curves of lasing devices of sample B with 80 $\mu$ m width by using the 1950 nm pumping laser. The power-dependent lasing spectra at the temperature of (b) 265 K and (c) 270 K.....	97
Figure 8.1 Schematic diagram of Ge <sub>0.95</sub> Sn <sub>0.05</sub> /Ge <sub>0.91</sub> Sn <sub>0.09</sub> /Ge <sub>0.95</sub> Sn <sub>0.05</sub> (a) SQW (Sample A) and (b) DQW (Sample B) (not to scale).....	100
Figure 8.2 (a) Cross-sectional TEM image of Sample A and (b) EDX line scanning. (c) TEM image of Sample B. Inset: FTP. The smooth boundaries at the atomic level was highlighted in (d) zoomed-in TEM image. ....	101
Figure 8.4 Temperature-dependent PL for (a) Sample A and (b) Sample B shows direct bandgap transition is dominant for both QWs at room temperature. ....	105
Figure 8.5 The calculated band structure of Sample A indicates type-I band alignment. ....	107
Figure 8.6 The electron occupation ratio between $\Gamma$ and L valley, lifetime of SRH process and statistical number of phonons (insert) verse temperature. ....	109
Figure 8.7 The schematic diagram of QW structure and the change of SnCl <sub>4</sub> flow fraction during the CVD epitaxy process of QW structure. ....	110
Figure 8.8 The SIMS profiles of sample B, C, and D were shown in (a), (b), and (c), respectively. The Ge interlayer was removed gradually from sample B to D. ....	112
Figure 8.9 The comparison of PL spectra of sample B, C, and D at the temperature of 10 K. ..	114
Figure 8.10 (a) The bright field TEM image of sample D. (b) The band diagram of QW structure of sample D, showing the type-I band alignment of QW. ....	115

## List of Tables

Table 1.1 The summary of MBE and CVD growths of GeSn. ....	6
Table 2.1 The summary of the various lifetimes of carriers. ....	21
Table 2.2 EPD results of Ge film on Si at different areas. ....	26
Table 2.3 The growth recipe of Ge on Si by HFA-CVD and the corresponding thickness of Ge films. ....	27
Table 2.4 The summary of PE-CVD growth recipes of GeSn samples. ....	33
Table 2.5 The summary of Sn compositions and PL peak positions of sample 1 and 2. ....	35
Table 2.6 The summary of growth recipe of GeSn on Ge buffered Si substrate. ....	38
Table 2.7 The summary of data fitting results of GeSn films. ....	41
Table 4.1 Summary of GeSn layer thicknesses, the maximum Sn compositions, average of Sn compositions, degree of compressive strains and degree of relaxations. ....	58
Table 7.1 The summary of Sn content, the maximum compressive strain, and the minimum bandgap for sample A and sample B. The experimental bandgap was extracted from PL spectra at 300 K. ....	82
Table 7.2 The summary of GeSn lasing results. ....	98
Table 8.1 Summary of material characterization results for sample A. ....	103
Table 8.2 Summary of material characterization results for sample B. ....	103
Table 8.3 The calculated band structure of Sample A. ....	108
Table 8.4 Design of Sample structures after RP-CVD growth in order to remove the Ge interlayer of GeSn QW. ....	112

## Chapter 1. Introduction

### 1.1. Motivation

Silicon (Si) photonics is a rapidly expanding technology that integrates photonic circuits onto a Si substrate, which has seen progressive growth since 1980s and 1990s[1][2][3]. Si photonics was initially motivated by the needs of broadband fiber optic communications which enable the high data densities and transmission over longer distance[4][5]. The integration of Si electronics and photonics has been a successful technology[6][7] and has been developed a wide range of applications such as night-vision imaging, solar, LiDAR, optical sensing of chemistry and biology and so on[8]. Nowadays, three approaches have been proposed to integrate electronics and photonics: 1) Putting electronics and photonics on separated chips; 2) Bonding the electronics and photonics components on a single chip; 3) monolithically optoelectronic integrated circuits. The third approach is more advantageous because of the seamless and robust process and large scalability of devices.

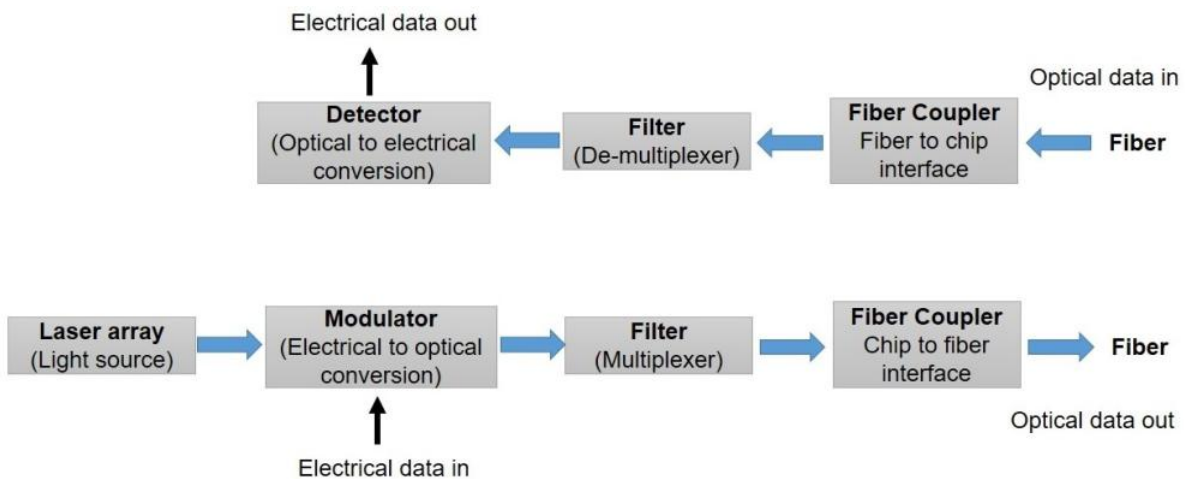


Figure 1.1 The schematic diagram of a complete set of silicon photonics transceiver.

The complete set of components for Si photonics transceivers was schematically drawn in Figure 1.1. The optical data-out module starts from the Laser arrays with multiple wavelengths as the



light sources. The optical signals with different wavelength were then transmitted in parallel by low-loss strip waveguide, followed by the Modulator which converts electrical data into optical data. The modulated optical data in multiple lines were filtered by the Multiplexer. Finally the selected optical data by the Multiplexer was coupled into the Fiber. For the data-in module the optical data was firstly transferred from Fiber to strip waveguide by Fiber Coupler. After the Demultiplexer Filter, the optical data was finally converted into electrical data by the Detector. Among all the Si photonics components an efficient light source integrated on Si substrate is still missing. In order to achieve this goal, laser devices based on III-V semiconductor materials such as InP[9] or GaAs[10] were employed to integrate on Si based platform by using the selective area growth[9] or wafer-bonding[11] approach. The III-V based laser devices integrated on Si are called hybrid silicon lasers. However, III-V semiconductor materials are different from Si substrate in lattice constant, thermal expansion and chemical polarity, which greatly increase the fabrication costs. Group IV materials are highly desirable due to the similar chemical and physical properties with Si, which enables the fabrication of highly sophisticated Si photonics devices at lower costs than those currently required for III-V compound semiconductors. The Si Raman laser[12][13] and rare-earth-ion laser on Si[14] were reported, which rely on the non-bandgap emission and exclude from the direct electrical pumping. Electrically pumped  $n^+$ -doped tensile-Ge laser on Si has been demonstrated at room temperature[15] [16][17]. However, none of these approaches have led to satisfactory results so far.

GeSn alloy has drawn great attentions as a complementary metal–oxide semiconductor (CMOS) compatible optoelectronic material for Si photonics[18][19]. The devices based on GeSn alloy could be monolithically integrated into well-established and high-yield Si-based integrated circuits, which is favorable for chip-scale optoelectronics devices featuring smaller size, lower

cost, and higher reliability. Unlike the traditional group-IV semiconductors i.e. Si and Ge with relatively low light emitting efficiency, the direct-bandgap feature of GeSn with sufficiently high fraction of Sn is favorable for light emitting devices. GeSn with Sn composition over 8% could become the direct bandgap material[20][21], which is advantageous for efficient light source. As shown in Figure 1.2 (a), Ge is an indirect bandgap material in which the fourfold degenerate indirect valley (L-valley) in conduction band lies 140 meV below the direct valley ( $\Gamma$ -valley). For GeSn alloy both direct and indirect bandgap decrease due to Sn incorporation while the direct one shrinks faster than the indirect one, which was shown in Figure 1.2 (b). As a consequence, GeSn passes the indirect-to-direct bandgap transition for Sn contents more than 8% (Figure 1.2 (c))[21]. Additionally, by tuning Sn composition the GeSn-based devices with multiple operating wavelengths are easily achieved, enabling the broad coverage of mid infrared wavelength from 2 up to 12  $\mu\text{m}$ . The low temperature epitaxy of GeSn on Si compatible with existing CMOS processes makes GeSn more attractive for optoelectronics applications.

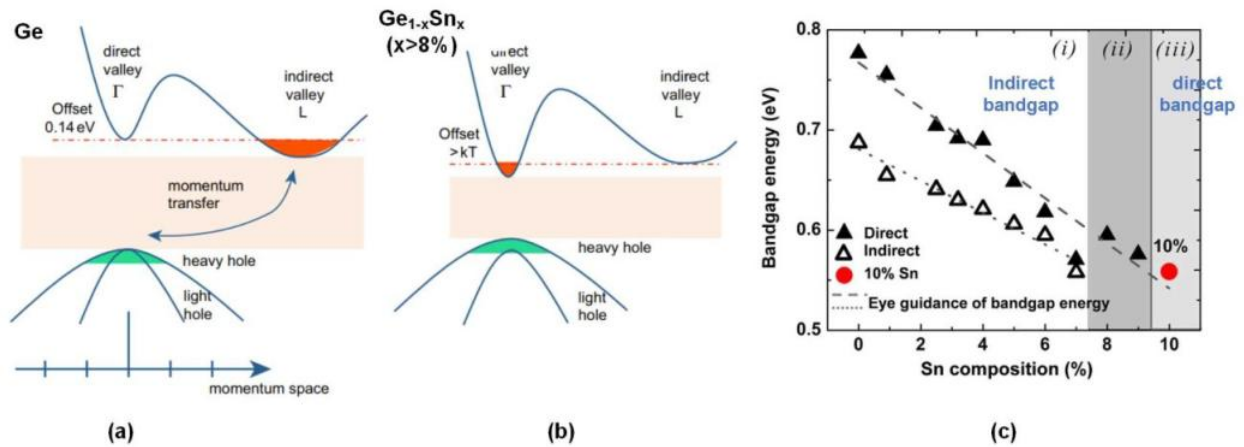


Figure 1.2 (a) Band structure of bulk Ge shows the indirect bandgap characteristics. (b) GeSn with Sn content more than 8% exhibits the direct bandgap characteristics. (c) The transition between indirect and direct energy bandgap of GeSn as a function of Sn composition.

## 1.2. Growth technology for GeSn

From material growth perspective, the epitaxy of single crystalline GeSn with high material quality is challenging due to the following factors: i) Low (<1%) equilibrium solid solubility of  $\alpha$ -Sn in Ge[22]: Since Sn atoms exhibits a comparably low free surface energy, Sn atoms tend to segregate during the epitaxy growth and form  $\beta$ -Sn clusters[23][24]. ii) Small temperature window for GeSn epitaxy growth: Low temperature is required for high Sn incorporation to suppress Sn precipitation. However, low temperature growth easily leads to epitaxial breakdown for thick film due to the severe surface roughening[25]; iii) Large lattice mismatch (~15%) between Ge and  $\alpha$ -Sn, making GeSn epitaxy with smooth and high quality material difficult.

Benefiting from the maturity of epitaxial technology, such as molecular beam epitaxy (MBE), and chemical vapor deposition (CVD), high quality single crystal GeSn could be grown under non-equilibrium conditions. The non-equilibrium growth of GeSn introduces Sn contents higher than the thermal equilibrium solid-solubility into substitutional lattice sites of Ge. Figure 1.3 shows the major achievements of GeSn epitaxy using both MBE and CVD techniques. The first attempt to grow GeSn alloys was based on MBE technology in 1980s and 1990s. Several substrates including InP[26], GaAs[27] and InSb[28], et al. were utilized in MBE in order to grow GeSn on substrates with the lowest lattice mismatch. High quality epitaxial Sn-rich GeSn alloys with Sn content >92%[27] and >87%[28] were achieved on InSb or InSb/GaAs substrates and the corresponding GeSn thickness is up to 150 nm. For Ge-rich GeSn, the ultra-high Sn content of 27% with low temperature MBE growth was achieved on InP substrate[29]. In terms of the conventional Group IV substrate such as Si and Ge, the first single crystal ultra-thin GeSn layer (<2 nm) on Ge was reported in 1992 and high Sn content up to 10% was achieved[30]. The growth of pseudomorphic GeSn layers with Sn content between 3.5% and 11.5% was grown on Ge using ion-assisted MBE

technique[31]. The thickness was obtained between 50 and 200 nm. However, the low temperature (100-200°C) growth as well as limited layer thickness for single crystal hinders the GeSn growth with device-level material quality. Recently the single crystal GeSn with high Sn content of 18.5% was obtained on Si-based Ge buffer using low temperature MBE growth, although the thickness is limited within 100 nm[32].

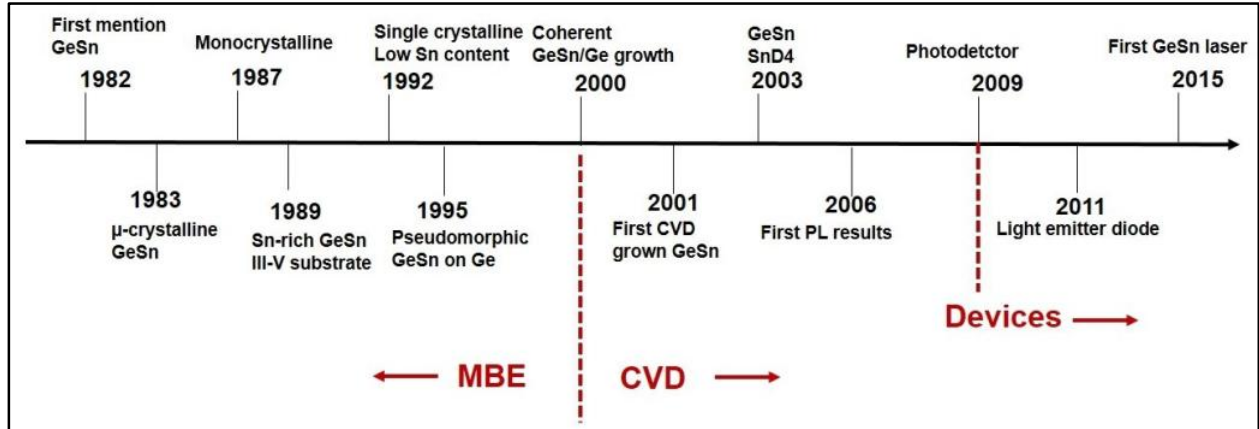


Figure 1.3 The overview of major achievements of GeSn growth since GeSn was first mentioned. Two growth techniques of MBE and CVD were mainly employed in the history of GeSn epitaxy.

CVD technique for GeSn epitaxy has made significant progress as it promises the uniform and homogenous GeSn epitaxy for the mass production of optoelectronic devices. One of the important factor for CVD growth is to choose a suitable Sn precursor. The first CVD grown GeSn on Si was reported by Kouvetakis and Menendez et al[33][34]. They introduced the ultra-high vacuum (UHV) CVD for high quality GeSn using Digermane ( $\text{Ge}_2\text{H}_6$ ) and Tin Deuteride ( $\text{SnD}_4$ ) as precursors. The corresponding Sn contents range from 2 to 15% on Si substrate at the temperature from 250-350°C, respectively. The same group also reported the first photoluminescence (PL) result in 2007[35]. The atmospheric pressure CVD was adopted for the epitaxial  $\text{Ge}_{0.92}\text{Sn}_{0.08}$  on Ge substrate at the temperature of 320°C. The commercial available precursors  $\text{Ge}_2\text{H}_6$  and  $\text{SnCl}_4$  were used. Since then, many studies on GeSn alloy focus on the high quality, high Sn content and thick GeSn. High quality GeSn with 12.6% Sn content has been grown using  $\text{Ge}_2\text{H}_6$  and  $\text{SnCl}_4$  as

Table 1.1 The summary of MBE and CVD growths of GeSn.

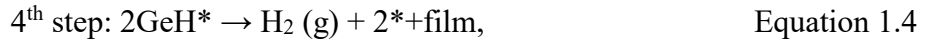
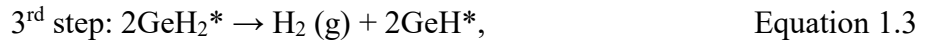
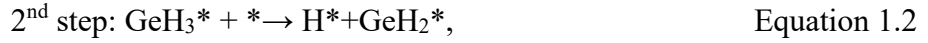
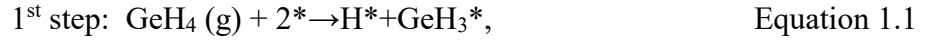
Growth method	Research team	Sn Source/Precursors	Ge Source/Precursors	Major achievements
MBE	Standard University	Solid Sn source	Solid Ge source	Sn%: up to 10%[45]
MBE	University of Delaware	Solid Sn sources	Solid Ge source	Thickness: up to 100 nm Sn%: up to 18.5%[32]
MBE	University of Stuttgart	Solid Sn sources	Solid Ge source	Thickness: up to 200 nm Sn%: up to 18%[46]
MBE	National Taiwan University	Solid Sn source	Solid Ge source	Sn%: up to 7.8%[47]
MBE	National University of Singapore	Solid Sn source	Solid Ge source	Thickness: up to 50 nm Sn%: up to 17%[48]
MBE/ Magnetron Sputter Epitaxy	Institute of Semiconductors, Chinese Academy of Sciences	Solid Sn source	Solid Ge source	Thickness: 140 nm Sn%: up to 12%[49]
Hot-Wall UHV-CVD	Arizona State University	SnD <sub>4</sub>	Ge <sub>2</sub> H <sub>6</sub> , Ge <sub>3</sub> H <sub>8</sub> , Ge <sub>4</sub> H <sub>10</sub>	Sn%: up to 17%[50]
RP-CVD	IMEC	SnCl <sub>4</sub>	Ge <sub>2</sub> H <sub>6</sub>	Sn%: up to 12.6%[51]
RP-CVD	Stanford University/ Applied Materials	SnCl <sub>4</sub>	Ge <sub>2</sub> H <sub>6</sub>	Sn%: up to 8%[52]
RP-CVD	Peter Grünberg Institute	SnCl <sub>4</sub>	Ge <sub>2</sub> H <sub>6</sub>	Thickness: up to 1 μm Sn%: up to 14%[36]
RP-CVD	CEA-LETI	SnCl <sub>4</sub>	Ge <sub>2</sub> H <sub>6</sub>	Thickness: up to 200 nm Step graded Sn composition layer Sn%: up to 16%[39]
RP-CVD	ASM/University of Arkansas/ Arktonics LLC	SnCl <sub>4</sub>	GeH <sub>4</sub>	Thickness: up to 1.2 μm Sn%: up to 22.3%[44]
UHV-CVD	University of Arkansas/ Arktonics LLC	SnD <sub>4</sub> /SnCl <sub>4</sub>	GeH <sub>4</sub>	Sn %: 5%-7%

precursors[36], with the thickness up to 1  $\mu\text{m}$ . The high quality of GeSn results in superior optical properties, which was evidenced by strong light emission of photoluminescence (PL) and electroluminescence (EL)[37][38]. High Sn incorporation up to 16% has been achieved using the step graded method using the same growth chemistry[39]. High order Ge hydrides such as  $\text{Ge}_3\text{H}_8$  or  $\text{Ge}_4\text{H}_{10}$  were also utilized for GeSn growth in order to pursue high Sn incorporation[40]. Those highly reactive Ge hydrides enable the high growth rate at low temperature due to their weak Ge-Ge molecular bond to favor more Sn incorporation. However,  $\text{GeH}_4$  as precursor for GeSn growth remains very attractive for industrial manufacturing due to its low cost and high thermal stability at room temperature[41][42]. We previously reported low-defect and thick GeSn growth with Sn incorporation up to 17.5% using  $\text{GeH}_4$  and  $\text{SnCl}_4$  as precursors[43]. Table 1.1 summarizes the GeSn epitaxy within the worldwide research group by both MBE and CVD techniques. It is noteworthy that so far the world record Sn incorporation has been achieved up to 22.3% by our collaborator of ASM Company[44]. The corresponding thickness of GeSn is up to 1.2  $\mu\text{m}$ , which is sufficient for the device fabrications such as GeSn laser and detector, etc.

### **1.3. Growth mechanism of GeSn**

The mechanism of CVD process for GeSn epitaxy could be understood by chemical reaction of precursors on the surface. Specifically, the chemical reactions include surface adsorption, decomposition, adatom migration and byproduct desorption and so on[53][54]. Figure 1.4 describes the hydride elimination pathway of  $\text{GeH}_4$  on the Ge (001) surface, which consists four subsequent Ge-H bond dissociation processes[55][56]. The hydrogen atoms in  $\text{GeH}_4$  are eliminated gradually by thermal decomposition kinetics on the surface. Each step depends on the empty sites on the surface. If the surface is mainly covered by hydrogen atoms, the growth rate is limited[57]. The hydrogen elimination process could be described by the following chemical

reactions with the available surface sites involved[58][59]. The symbol \* stands for the available surface sites.



In the 1<sup>st</sup> step of chemical reaction, two open surface sites are consumed while in the 2<sup>nd</sup> step of reaction one open site is consumed. In the 4<sup>th</sup> and 5<sup>th</sup> steps, two open sites on the surface are generated, respectively. The free surface sites are temperature dependent, which is critical for the growth rate. At the high temperature, a large number of open sites are generated, leading to the high growth rate. In contrast, at the low temperature the growth rate is limited because of the high coverage of surface sites. A “feedback action” of the open sites will control the growth rate during the continuous GeSn growth[60]. The reaction rate of the 3<sup>rd</sup> and 4<sup>th</sup> steps affects the rate of reaction in the 1<sup>st</sup> and 2<sup>nd</sup> steps via controlling the coverage of open sites on the surface.

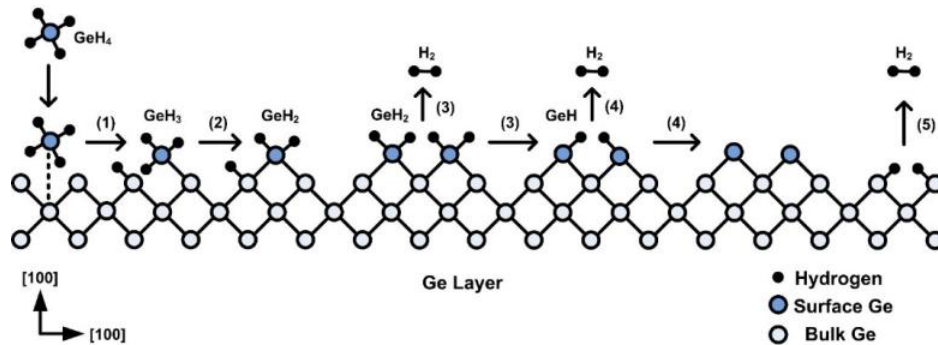


Figure 1.4 Schematic mechanism of hydride elimination pathway describing GeH<sub>4</sub> chemisorption on the Ge (001) surface.

The liquid SnCl<sub>4</sub> was used as the Sn precursors for the CVD growth of GeSn in the dissertation. In order to deliver the liquid SnCl<sub>4</sub> into the CVD reactor chamber, two methods are utilized. The first method is to use the vapor pressure because of the volatility of SnCl<sub>4</sub>. The vapor pressure of SnCl<sub>4</sub> at room temperature is 20 mmHg (1333.3 Pa). More vapor pressure could be obtained by heating up the SnCl<sub>4</sub> cylinder, providing a flexible availability of the partial growth pressure of SnCl<sub>4</sub> during the CVD growth. This method was usually adopted in UHV-CVD system. However, in the RP-CVD system, the partial pressure of precursors must be higher than total pressure in the reaction chamber in order to deliver the precursors into the chamber. Therefore, the first method by using the vapor pressure to deliver SnCl<sub>4</sub> is not applicable. The second method is to use bubbler system. In this system the carrier gas such as argon or hydrogen could bubble inside the liquid SnCl<sub>4</sub> and deliver the SnCl<sub>4</sub> from SnCl<sub>4</sub> cylinder into the reaction chamber. The carrier gas is metered by mass flow controller (MFC) to control the flow rate of SnCl<sub>4</sub>. This method could be used not only in UHV-CVD system but only in RP-CVD system.

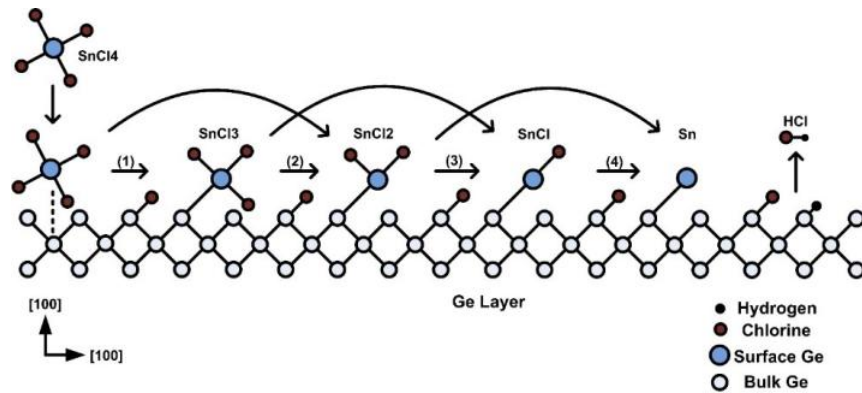
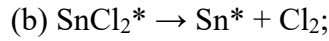
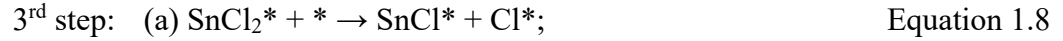
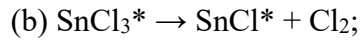
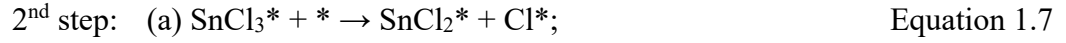
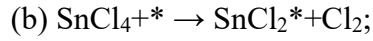
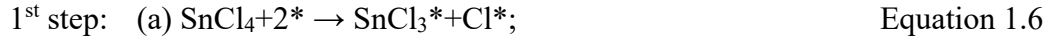


Figure 1.5 The possible reaction pathways of the SnCl<sub>4</sub> thermal decomposition.

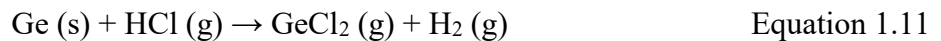
The kinetics of thermal deposition of SnCl<sub>4</sub> precursor on the surface of film was also studied, as shown in Figure 1.5. The SnCl<sub>4</sub> decomposes into one Sn atoms and four chlorine atoms via the chlorine elimination pathway, similar with GeH<sub>4</sub> dissociation process shown in Figure 1.4. However, due to the low thermal dissociation energy of SnCl<sub>4</sub>, more reaction steps are involved



during the decomposition process. The specific reaction mechanism was described as the following steps[61]:



The Sn-Cl dissociation steps (a) for each step are energetically favorable reactions in the decomposition pathways. Finally the  $\text{SnCl}_4$  decomposes into one Sn atoms and four chlorine atoms at the 3<sup>rd</sup> step (b) and the 4<sup>th</sup> step. The first step is a rapid process because the reaction energy barrier of (a) and (b) at the 1<sup>st</sup> step is low and could be negligible. In contrast, the 3<sup>rd</sup> and 4<sup>th</sup> steps are initiated to produce both Cl and Sn atoms slowly because of the high reaction barriers. One thing should be noted is that the gaseous HCl is formed at the 5<sup>th</sup> step during the dissociation of  $\text{SnCl}_4$ , which introduces the chemical etching of Ge during the GeSn epitaxy[62]. The etching reaction could be expressed as



The etching rate is both temperature- and pressure- dependent, which is similar with the growth rate. It indicates that the growth mechanism of GeSn is different from the traditional Ge epitaxy. The GeSn was grown with the competition between etching and epitaxy process. Under some specific conditions the etching rate is larger than the growth rate, resulting in the difficulty of GeSn epitaxy. Therefore, the growth window of GeSn is much narrower than Ge.

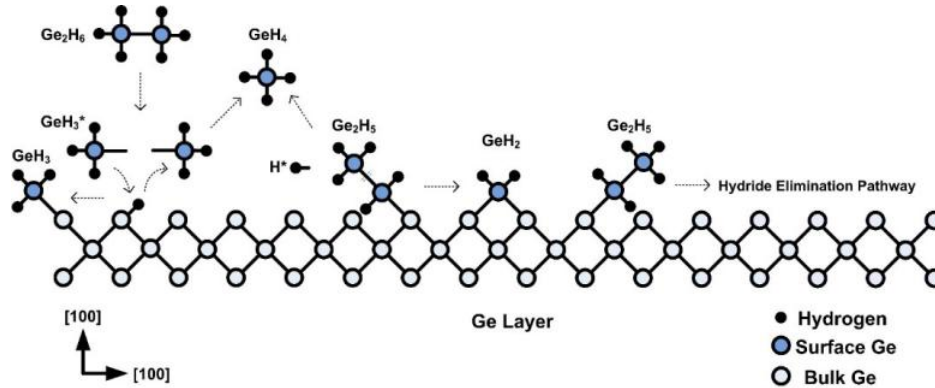
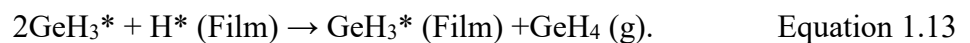
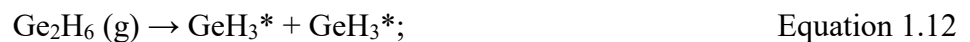


Figure 1.6 The possible reaction pathways of the  $\text{Ge}_2\text{H}_6$  thermal decomposition.

The thermal decomposition of the second order Ge hybrids Digermane ( $\text{Ge}_2\text{H}_6$ ) was studied as well, as shown in Figure 1.6. Compared with  $\text{GeH}_4$ ,  $\text{Ge}_2\text{H}_6$  experiences the lower dissociation energy because of its weaker atom bonds. High growth rate of GeSn could be ensured by using  $\text{Ge}_2\text{H}_6$  as the precursor, especially at the low growth temperature. The thermal decomposition of  $\text{Ge}_2\text{H}_6$  follows the normal hybrid elimination pathways, similar with that of  $\text{GeH}_4$ . The growth rate through hybrid elimination mainly depends on the availability of open surface sites. However, a new “concerted” growth mechanism was proposed to explain the high growth rate by using  $\text{Ge}_2\text{H}_6$  as the precursor[63]. The Ge-Ge bond is much weaker than Ge-H bond in  $\text{Ge}_2\text{H}_6$  molecules, which means that  $\text{Ge}_2\text{H}_6$  could be easily dissociated into two  $\text{GeH}_3^*$  fragment bonds. The  $\text{GeH}_3^*$  firstly replaces the surface sites which was previously occupied by the hydrogen atoms. Then the remaining  $\text{GeH}_3^*$  will react with  $\text{H}^*$  and form a  $\text{GeH}_4$  molecule as byproducts. The reaction could be written as[63] [64]:



This process is independent of the availability of open surface sites. Therefore,  $\text{Ge}_2\text{H}_6$  will ensure the high growth rate through the new “concerted” growth mechanism.

#### 1.4. Progress of GeSn laser

High quality direct bandgap GeSn alloy was investigated in recent years as gain medium for laser application. Figure 1.7 presents the timeline of development of GeSn lasing. The optically pumped microdisk resonator of pseudomorphic Ge/Ge<sub>0.92</sub>Sn<sub>0.08</sub>/Ge quantum well was firstly demonstrated in 2013[52]. The whispering-gallery-mode (WGM) resonances were observed. However, the Pseudomorphic Ge<sub>0.92</sub>Sn<sub>0.08</sub> in microdisk is still indirect bandgap material due to the large compressive strain and no indication of lasing was shown. Later on, High quality relaxed GeSn grown on Ge buffer by chemical vapor deposition features true direct bandgap characteristics and enables the edge emitting lasing with operating temperature up to 90 K[65] and 110 K[66]. The temperature-dependent PL indicates transition from indirect to direct bandgap for partial relaxed GeSn with more than 10% Sn. The modal gain with the value up to 110 cm<sup>-1</sup> was measured using variable stripe length method[65]. Optically pumped GeSn microdisk with significant improvement of lasing temperature of 130 K and lasing threshold of 220 kW/cm<sup>2</sup> at 50 K was presented by the same research team[67]. The compressive strain is gradient relaxed from the center to the edge of microdisk due to the undercut etching. The devices based on GeSn with high Sn content is highly desirable to extend the wavelength coverage well into mid infrared range for sensing applications. Optically pumped lasing of GeSn microdisk with 16% Sn was also demonstrated at 3.1 μm with operating temperature up to 180 K[68]. The corresponding lasing threshold is 377 kW/cm<sup>2</sup> at 25 K. Step graded GeSn was utilized to increase Sn incorporation and improve the material quality. Recently, the optically pumped edge emitting GeSn laser on Si was realized by Dr. Fisher Yu's research group with broad wavelength coverage from 2 to 3 μm[43]. The highest lasing temperature was measured as 180 K which is attributed to the high material quality and robust fabrication process.

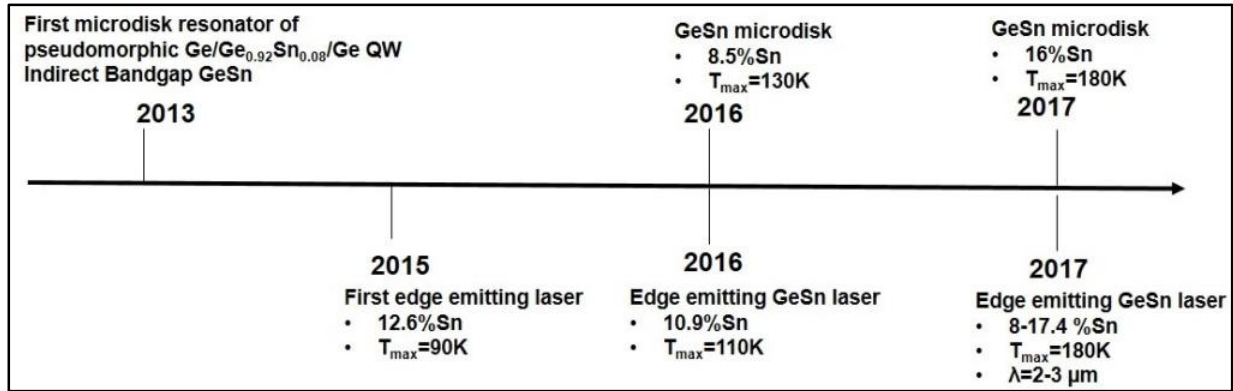


Figure 1.7 The timeline of the development of laser of GeSn since 2013.

### 1.5. Organization of this dissertation

The main goal of this dissertation was divided as the following: 1) To pursue the high quality and high-Sn-content GeSn by CVD technology; 2) To achieve the room temperature GeSn laser devices; 3) To obtain the true type-I GeSn/GeSn/GeSn quantum well structure. Following the above-mentioned objectives, this dissertation could be organized with nine chapters. Chapter 1 firstly introduced the background of GeSn as a group IV material for the potential light sources of Si photonics. The development of growth technologies such as MBE and CVD was then discussed since 1982 when the GeSn material was firstly grown by MBE. The growth mechanism of CVD technique was discussed. The dissociation processes of precursors such as GeH<sub>4</sub>, Ge<sub>2</sub>H<sub>6</sub>, and SnCl<sub>4</sub> were introduced. After the growth of device-level GeSn alloy, the progress of GeSn lasing including the edge emitting laser and microdisk was summarized.

Chapter 2 talked about the growth progress by using the custom designed UHV-CVD system. High quality Ge on Si substrate was grown by low/high temperature two-step epitaxy. The Ge film was then characterized by various measurement tools including PL, Raman and Ellipsometry, etc. The function of hot-filament module was explored and Ge on Si was grown and characterized. Plasma enhanced CVD growth of GeSn was studied for the first time worldwide. Buffer free GeSn on Si substrate was successfully grown. The high quality GeSn growth on Ge buffered Si substrate by

the standard UHV-CVD system was also investigated. The exploration of Ge(Sn) growth by UHV-CVD system provides the vital guidance for the future epitaxy of group IV materials.

Chapter 3 discussed the band structure calculation by K.P method. The strain effects were then included in order to provide more accurate description of GeSn band structure. Chapter 4 showed the strategies of pursuing the high Sn-content GeSn by RP-CVD system. The underlying mechanism of spontaneous Sn gradient GeSn films was discussed. It was attributed to the compressively strain effects on Sn incorporation. Various methods such as SIMS, EDX, and XRD were employed to confirm the spontaneous Sn-content GeSn on Ge buffer. Chapter 5 systematically studied the strain relaxation mechanism at both GeSn/Ge interface and the region beyond the critical thickness. This chapter reveals microscopically the strain relaxation process by high resolution TEM technique. Chapter 6 utilized Gibbs free energy calculation to well explain the strain effects on the Sn incorporation, providing the theoretical support of strain engineering to pursue the high Sn-content GeSn. The interplay between compressive strain and Sn composition was also discussed and the methods to grow even higher Sn-content GeSn was proposed.

Chapter 7 discussed the GeSn lasing devices by using the world-record 22.3% Sn-content GeSn alloy. The PL measurements were firstly conducted to explore the optical properties of GeSn alloy. The initial lasing study of GeSn devices demonstrates the feasibility of 22.3% Sn-content GeSn for device applications. By optimizing the configuration of lasing setup and adopting large size of GeSn devices, the near room temperature was finally achieved, which is the world-record performance. Chapter 8 talked about the advanced structure of GeSn/GeSn/GeSn QW. The initial study of GeSn QW reveals the existence of unintentional GeSn interlayer between barrier and well region. The Ge interlayer was removed by adopting the GeSn buffer instead of Ge buffer. The true type I GeSn/GeSn/GeSn QW was achieved, which was confirmed by the temperature dependent

PL measurements and theoretical study of band alignment of QW structure. Chapter 9 summarized the research work in this dissertation and proposed the future work.

## **Chapter 2. High quality Ge and GeSn by UHV-CVD**

### **2.1. Ultra-high vacuum chemical vapor deposition (UHV-CVD)**

The customer-designed UHV-CVD has been built up by our research group for the group IV epitaxy of Ge, SiGe, and (Si)GeSn systems. Figure 2.1 (a) shows the overview of cold-wall UHV-CVD system. The system composes of two chambers: the load lock chamber and the process chamber. The load lock chamber was designed to prevent the process chamber from exposing the atmospheric contaminants. Si wafers were RCA-standard cleaned prior to epitaxy in the cleanroom. The lowest pressure of process chamber is  $10^{-10}$  Torr and the growth temperature could be achieved as high as  $1000^{\circ}\text{C}$ . The inert gas of argon (Ar) and commercialized available  $\text{GeH}_4$  were used for Ge, SiGe, and (Si)GeSn epitaxy. Sn precursor of  $\text{SnCl}_4$  was used for (Si)GeSn growth. In addition, UHV-CVD system was equipped with the unique plasma module and hot filament module. Both modules could help break atomic bonds of precursors and improve material quality of GeSn. Both modules also increase growth rate at low temperature and thus lead to high Sn incorporation since more Sn atoms are buried in Ge lattice matrix at high growth rate. The CVD system was also upgraded by adding new gas maxing system to precious control flow fraction of precursors. The whole gas mixing system was installed inside the gas cabinets which was air exhausted by the mechanical fan. The schematic diagram of gas mixing system was shown in Figure 2.1 (b). The base pressure was kept as  $10^{-8}$  Torr to prevent the leakage of precursors during the mixing process. Prior to the CVD epitaxy, the precursors such as  $\text{GeH}_4$ ,  $\text{SnCl}_4$  was delivered into the mixing bottle for the uniform gas mixing. The molar fraction of each precursor was monitored by the Residual Gas Analyzer (RGA). The agitator was used within the mixing bottle

to maintain the uniformity of mixing. Gas mixing system helps improve mixture of precursors and thus homogeneity of GeSn epitaxy. Through gas mixing system a large range of gas flow ratio could be easily tuned in order to explore the optimized epitaxy window of UHV-CVD system.

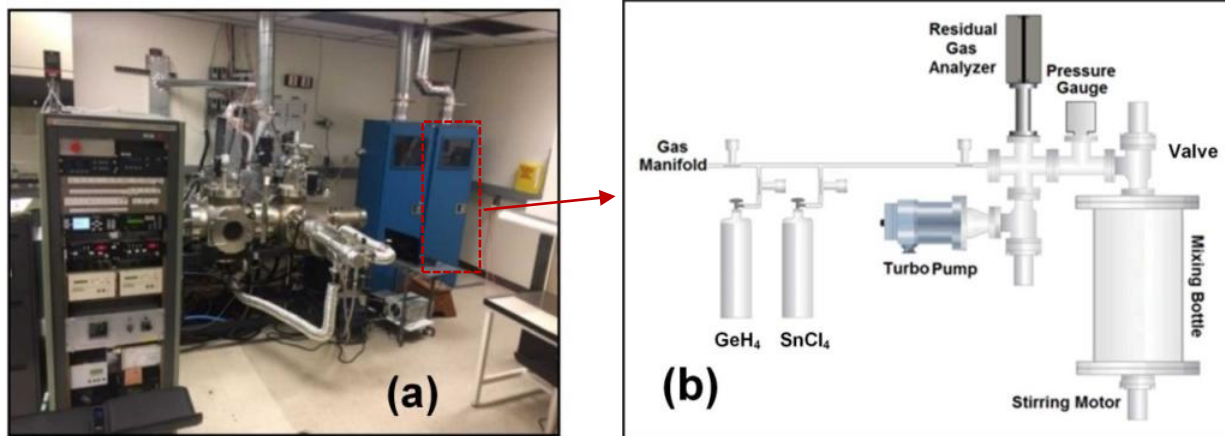


Figure 2.1 (a) The overview of customer-designed cold wall UHV-CVD system. (b) The schematic diagram of gas mixing system.

## 2.2. Two-step Ge buffer on Si

### 2.2.1. Ge growth on Si

Low/high temperature two step Ge buffer was firstly investigated in order to explore the growth ability of CVD machine. The Ge buffer growth benchmark the CVD growth for the guidance of GeSn growth. The Ge buffer could also act as the buffer layer between Si substrate and GeSn layer to accommodate the large lattice mismatch between Si and GeSn. For the first step Ge growth, the temperature from 350 to 400 °C is used while for the second step the growth temperature ranges from 500 to 600 °C. The growth pressure is kept at 1 Torr for both step growths. The growth time is 5 and 20 minutes for the 1<sup>st</sup> and 2<sup>nd</sup> steps, respectively. All the surface of Ge buffer is mirror like, suggesting that the low surface roughness. After the growth, the thickness information was obtained by data fitting of Ellipsometry measurements. Figure 2.2 (a) shows the growth rate of Ge as function of growth temperature of the first and second steps. As the temperature increases from

500 to 600°C at the second step, the growth rate increases dramatically. The activation energy was extracted as  $E_a=1.07$  eV using the following equation:  $GR = GR_0 * \exp(-\frac{E_a}{kT})$ , where GR is the growth rate and  $E_a$  represents the activation energy and  $kT$  is the product of the Boltzmann constant  $k$  and the temperature  $T$ . The activation energy of our growth is comparable with the published results[69][70]. The growth rate V.S. dilution ratio of GeH<sub>4</sub> and Ar was also investigated, as shown in Figure 2.2 (b). When the dilution ratio increases from 1:200 to 1:50 at different temperature condition, the growth rate increases, as expected.

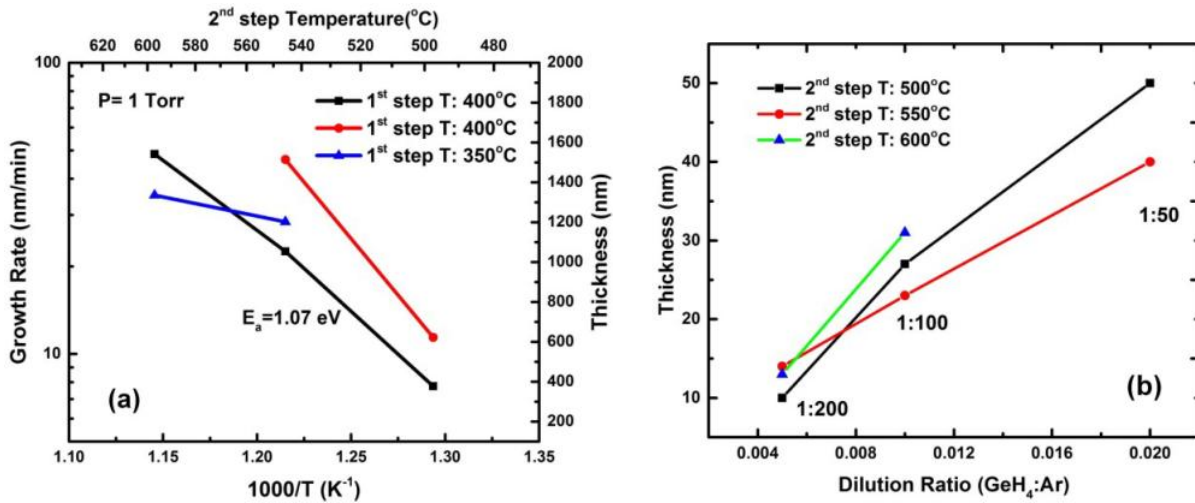


Figure 2.2 (a) The second step temperature V.S. the average growth rate. (b) The growth rate as a function of dilution ratio of GeH<sub>4</sub> and Ar. During the growth GeH<sub>4</sub> acts as a precursor of Ge buffer while Ar was used as the carrier gas.

### 2.2.2. Raman characteristics

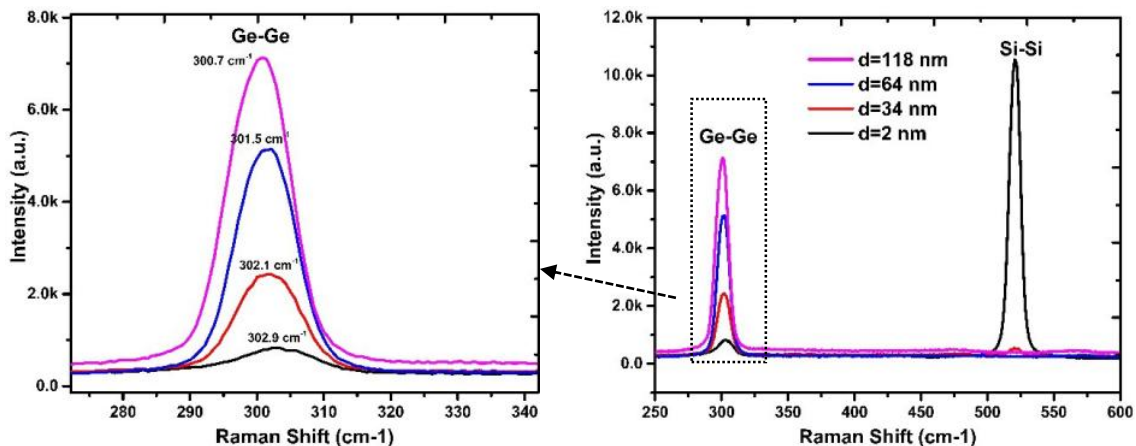




Figure 2.3 Ge-Ge LO Raman shift and Si-Si TO Raman shift with different thickness of Ge film on Si.

Raman spectroscopy was employed in order to probe the crystallization of two step Ge samples. The continuous wave (CW) laser with the wavelength of 632 nm was used as the excitation source of Raman measurements and the laser power was 10 mW. The reflected Raman scattering light was collected by spectrometer and nitrogen-cooled CCD (Charge Coupled Device) arrays. Figure 2.3 shows the Raman spectra for two step Ge films with the thickness ranging from 2 to 118 nm. The peak intensity of Ge-Ge longitudinal optical (LO) mode increases significantly when the thickness of GeSn increases. Meanwhile, the Si-Si peak of transverse optical (TO) mode was clearly observed at 2 nm thickness and decreases rapidly when the thickness increases. Si-Si TO mode stems from the Si substrate. The excitation laser with 632 nm was used in Raman measurements and has penetration depth of less than 100 nm in Ge. When Ge film is thin, the pumping laser could penetrate through Ge film and causes phonon scattering in Si substrate. Thus Si-Si Raman peak could be observed. Ge film on Si is under compressive strain, resulting in the blue shift of the peak of Ge-Ge LO. For example, the LO peak of fully relaxed Ge is  $300\text{ cm}^{-1}$  while Ge film with 2nm thickness has LO peak at  $302.9\text{ cm}^{-1}$ . However, with increasing thickness, Ge film relaxes gradually and the peak of Ge-Ge LO has a red shift towards LO peak of bulk Ge.

## 2.2.3. Photoluminescence (PL) characteristics

### 2.2.3.1 PL mechanism

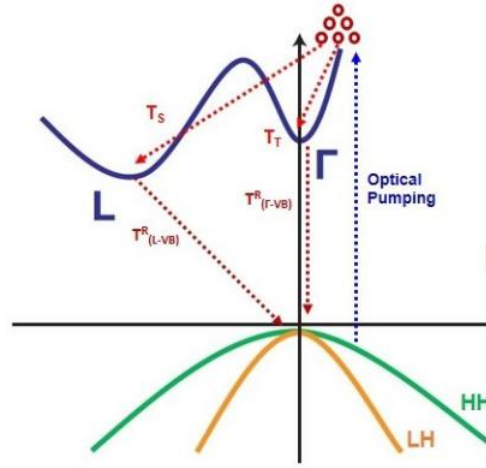


Figure 2.4 The schematic diagram of PL mechanism of bulk Ge. The pathways of carriers were drawn on the Ge band structure.

Figure 2.4 illustrates the PL mechanism of bulk Ge, in which two valence bands of heavy hole (HH) and light hole (LH) and one conduction band with  $\Gamma$  and L valleys were drawn. The direct bandgap energy ( $\Gamma$ -HH) is 0.798 eV and the indirect bandgap energy (L-HH) is 0.664 eV[71]. The electrons are excited from valance to conduction band via external laser source. The carrier excitation path is vertical in k space in order to keep the conservation of momentum governed by the Fermi's golden rules. The "hot" photoexcited electrons firstly reside at the high energy states and then quickly redistribute and cool down to the  $\Gamma$  and L valleys of conduction band through thermal relaxation process. Note that the L valley is 140 meV lower than  $\Gamma$  valley of bulk Ge. Therefore, most of the electrons transfer to the L valley. Meanwhile, the "hot" holes are condensed to the top of valance bands. The symbol of  $T_T$  in the Figure 2.4 represents the carrier lifetime of thermal relaxation from excited energy states to  $\Gamma$  valley, which was measured as  $110 \pm 30$  fs by ultrafast transient absorption spectroscopy[72][73].  $T_s$  is the lifetime of the inter-valley scattering from the  $\Gamma$  valley to L valley which occurs at the 200-300 fs time scale[74][75]. The radiative

recombination of carriers at the  $\Gamma$  and L valleys was also shown on the Figure 2.4.  $T^R_{(\Gamma-VB)}$  stands for the carrier lifetime of direct bandgap from  $\Gamma$  valley to valence band (VB) and  $T^R_{(L-VB)}$  represents the carrier lifetime of indirect bandgap from L valley to VB. The lifetime  $T^R_{(\Gamma-VB)}$  varies from ns to  $\mu$ s order of magnitude, depending on the carrier injection level and the operating temperature[76][77].  $T^R_{(L-VB)}$  is normally four or five orders of magnitude higher than  $T^R_{(\Gamma-VB)}$ [78]. The optical transition between  $\Gamma$  valley to VB is much more efficient than the transition between L valley to VB[79]. However, because the majority of carriers populate that the L valley, the indirect bandgap light emission dominates at the PL spectrum of bulk Ge at room temperature.

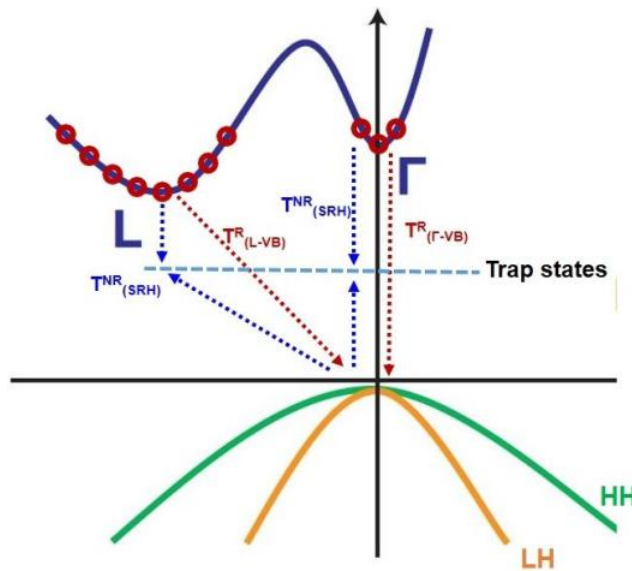


Figure 2.5 The mechanism of carrier recombination in the presence of Shockley-Read-Hall (SRH) recombination centers.

The PL mechanism in the presence of trap states was also discussed, as shown in Figure 2.5. For Ge growth on Si, the misfit dislocations are generated in order to accommodate the lattice mismatch between Ge and Si. The dislocations introduce the trap energy states within the bandgap of Ge. Since the majority of dislocations are localized in Ge layer, the trap levels are extended in k space of band structure. The introduced trap states act as the deep level recombination center and greatly influence the PL mechanism. The non-radiative recombination of Shockley-Read-Hall

(SRH) process via trap states provides additional non-radiative recombination pathway of carriers. The determination of SRH lifetime of  $T_{\text{SRH}}^{\text{NR}}$  is complicated because the relevant parameters are difficult to obtain, such as the density of trap energy levels and the positions trap energy states within the bandgap energy. Usually  $T_{\text{SRH}}^{\text{NR}}$  is the picosecond order of magnitude, which is a fast recombination process compared with the lifetime of radiative recombination:  $T_{(\Gamma\text{-VB})}^{\text{R}}$  and  $T_{(\text{L-VB})}^{\text{R}}$  (See appendix C). The summary of the various lifetimes of carriers was listed in Table 2.1.

Table 2.1 The summary of the various lifetimes of carriers.

Lifetime	$T_{\text{T}}$	$T_{\text{s}}$	$T_{(\Gamma\text{-VB})}^{\text{R}}$	$T_{(\text{L-VB})}^{\text{R}}$	$T_{\text{SRH}}^{\text{NR}}$
Value	110±30 fs[72][73]	200-300 fs[74][75][80]	1 ns – 1 µs[76][77]	1 us-1 ms[78]	1 ps-1 ns

### 2.2.3.2 PL measurements

PL measurements was utilized to evaluate optical properties of two step grown Ge samples. In the PL setup, a 1064 nm pulsed laser was utilized as a pumping source with 45 kHz repetition and 6 ns pulse width. The laser spot size was measured as 20 µm in diameter and the pumping power was 300 mW. PL emissions were collected by spectrometer and sent to thermoelectric-cooled lead sulfide (PbS) detector with the wavelength detection cut-off at 3 µm. A lock-in system along with a chopper were applied to amplify the PL signal. Figure 2.6 (a) shows the room-temperature power dependent photoluminescence (PL) of bulk Ge and Figure 2.6 (b) shows the two step grown Ge films on Si substrate. The Ge film were grown 1 µm thick. For PL spectra of bulk Ge, both direct and indirect bandgap were observed. The peaks at 1550 nm (0.8 eV) and 1780 nm (0.7 eV) correspond to direct and indirect bandgap, respectively. The peak of indirect bandgap dominates due to the indirect-bandgap nature of Ge. With the increase of optical pumping power both direct and indirect emission increase while the PL peak of indirect bandgap dominates over all the

spectra. For our grown Ge film, the direct bandgap emission dominates over indirect bandgap emission for all the power-dependent PL spectra. The indirect bandgap emission could only be observed at the high excitation power. It is because indirect transition is an inefficient process as most injected electron-hole pairs recombine non-radiatively before the occurrence of radiative recombination. Therefore the indirect PL can be clearly observed in ultra-high quality germanium or low-temperature measurement at which non-radiative recombination centers are greatly suppressed. On the contrary, the direct transition is a fast process with radiative recombination rate four or five orders of magnitude higher than that of the indirect transition. For our grown Ge samples, the threading dislocations generated during the large lattice mismatch between Ge and Si degrade material quality and dramatically decrease indirect bandgap emission. In order to decrease the threading dislocation the high temperature cycle annealing is necessary. In addition, the peaks of both direct and indirect bandgap have a red shift compared to bulk Ge. It is attributed to the residual tensile strain which is generated during high temperature growth due to the discrepancy of thermal expansion coefficients between Si and Ge. Figure 2.6 (c) represents the peak intensity as a function of pumping power for two Ge on Si samples and bulk Ge. Our grown samples show the similar trends with bulk Ge. The peak intensities of two step Ge samples are 8 times smaller than that of the bulk Ge.

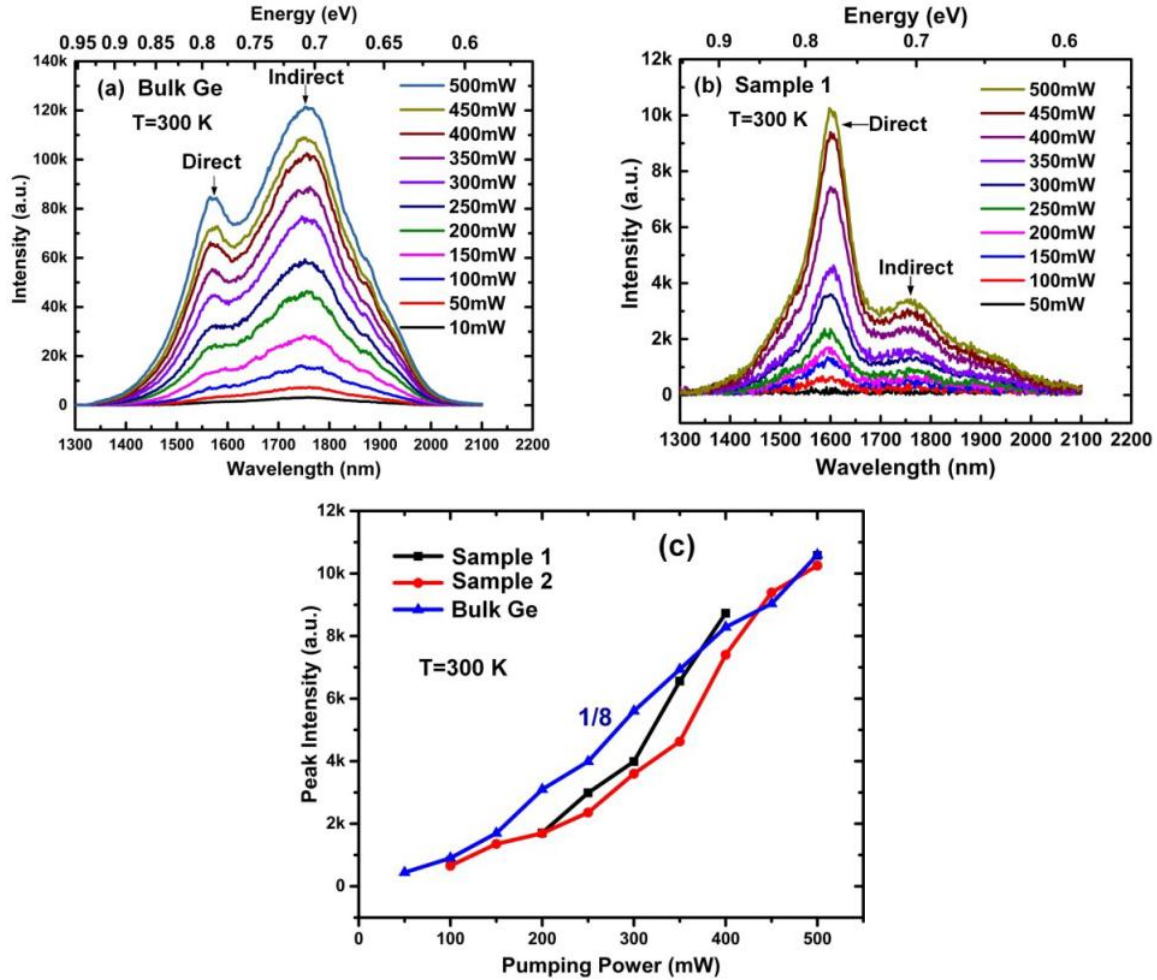
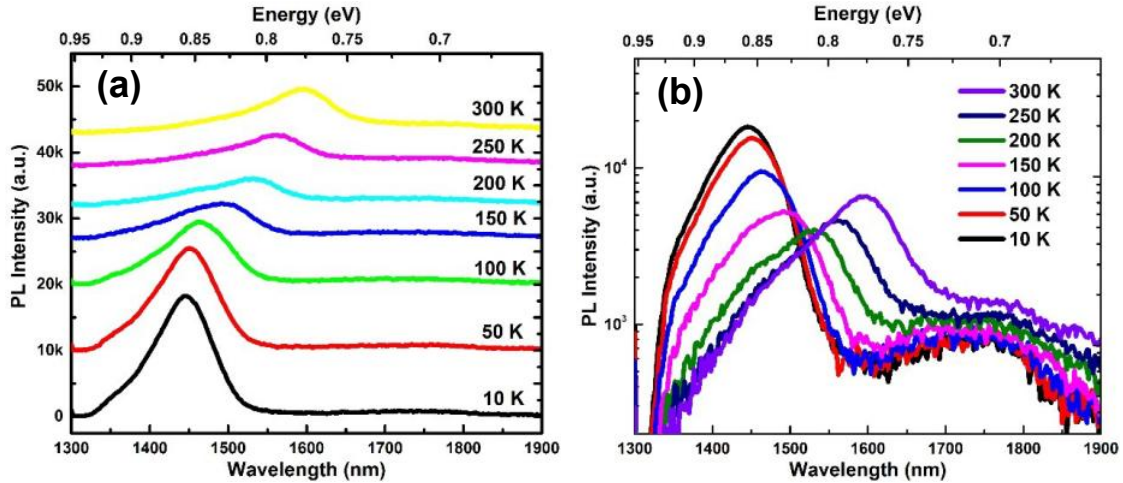


Figure 2.6 Power-dependent PL spectra of (a) bulk Ge and (b) two step Ge films with thicknesses of 1  $\mu\text{m}$ . (c) The peak intensity of sample 1,2 and bulk Ge as the function of pumping power.

The temperature-dependent PL of two step Ge sample was measured at the pumping of 150 mW as shown in Figure 2.7 (a), in which the direct bandgap emission dominates for all the spectra at the temperature from 10 to 300 K. The PL spectra at logarithmic scale at different temperature were also drawn in Figure 2.7 (b) for clarity. With the decrease of temperature down to 10 K, the emission peak of direct bandgap has a clear blue shift from 1590 nm (0.78 eV) to 1450 nm (0.86 eV), following the empirical Varshni model. The PL peak intensity of direct bandgap decreases as the temperature drops from 300 to 200 K while the intensity increases from 200 to 10 K. At the room temperature, the PL peak of indirect bandgap is negligible because the majority of carriers

recombine via the non-radiative SRH process. At the low temperature below 200 K the indirect PL peaks are observable. However, the indirect peak intensity at low temperature is one order of magnitude lower than direct peak intensity. The integrated PL intensity and peak positions were drawn in Figure 2.7 (c). When the temperature is decreased from 300 to 200 K, the integrated intensity of emission is reduced about 30%. It is because more electrons are condensed from direct to indirect bandgap with the decrease of temperature. As the continuous cooling down of Ge sample from 200 to 10 K, the integrated intensity dramatically increases about 2.6 times. It is attributed to the dramatically reduced SRH (Shockley-Read-Hall) non-radiative recombination with the decrease of temperature. At the low temperature, the majority of non-radiative trap states within bandgap which are introduced by the defects were frozen, resulting in the increase of radiative emission.



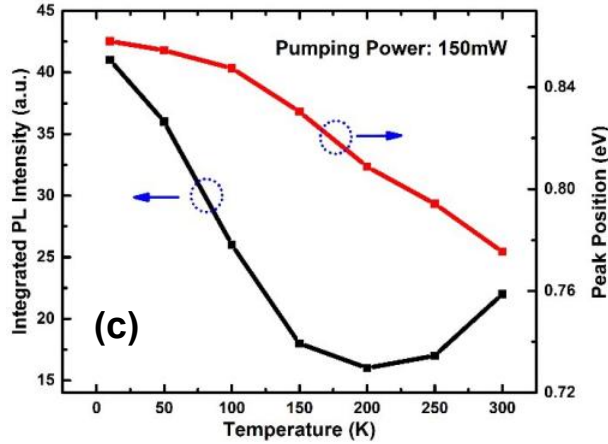


Figure 2.7 (a) Temperature- dependent PL measurements of the two step Ge sample on Si. (b) The PL spectra at logarithmic scale at different temperatures. (c) The corresponding integrated PL intensity and the peak positions of direct bandgap as a function of temperature.

#### 2.2.4. Etch pit method

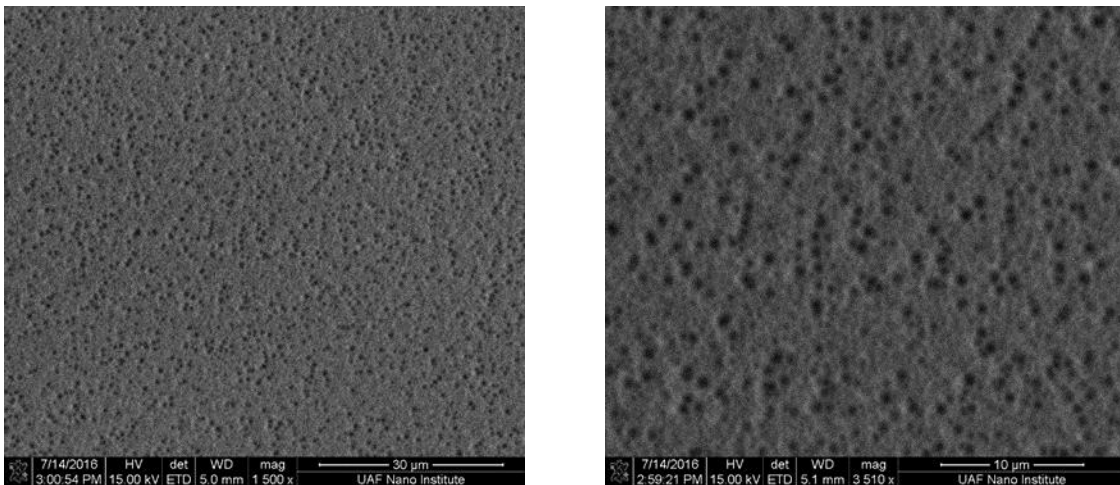


Figure 2.8 The SEM Images of etch-pit method for Ge film on Si at different areas.

The etch-pit method was employed to evaluate the threading dislocation density for our Ge buffer. Etch pit method is a preferential etching solution on the surface of samples. The etching rate is high at the dislocation regions on the surface. Then the pits or grooves form and represent the dislocations as a result of preferential etching. The pits or grooves are visible under the optical microscopy or scanning electron microscopy. By counting the numbers of pits or grooves the dislocation density could be evaluated. The wet chemical etching for etch pit method was well



established using iodine solution [CH<sub>3</sub>COOH (65 mL)|HNO<sub>3</sub> (20 mL)|HF (10 mL)|I<sub>2</sub> (30 mg)][81]. The etching process was done at temperature of 0°C in order to reduce the aggressive wet etching. Since I<sub>2</sub> is difficult to solve into the solutions, the magnetic stirring bar was applied to accelerate the solving time. The etch-pit results were obtained by image of scanning electron microscopy, as shown in Figure 2.8. The black dots on the SEM imaging represent the threading dislocations. In order to accurately extract threading dislocation density, three different areas on Ge surface were considered. By counting the values of etch pits of different areas, the average threading dislocation density was eventually calculated as 1.94\*10<sup>7</sup> cm<sup>-2</sup>, which is comparable with other reported two step Ge on Si growth followed by cycle annealing between high temperature and low temperature using hot wall UHV-CVD[81].

Table 2.2 EPD results of Ge film on Si at different areas.

Area	The 1 <sup>st</sup> area	The 2 <sup>nd</sup> area	The 3 <sup>rd</sup> area	The average
EPD value	1.85*10 <sup>7</sup> cm <sup>-2</sup>	2.14*10 <sup>7</sup> cm <sup>-2</sup>	1.84*10 <sup>7</sup> cm <sup>-2</sup>	1.94*10 <sup>7</sup> cm <sup>-2</sup>

### 2.3. Hot-filament-assisted CVD growth of Ge on Si

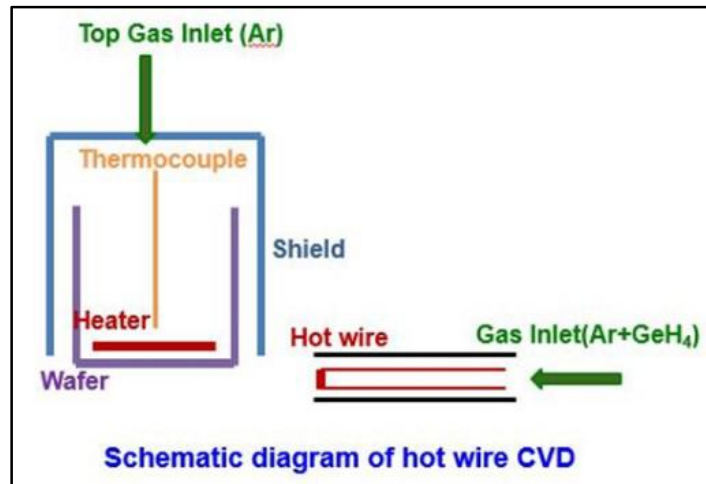


Figure 2.9 The schematic diagram of hot-filament assisted CVD.

The setup of hot-filament assisted CVD (HFA-CVD) was also equipped in the reactor, which is a useful method for the deposition of many different semiconductor materials such as SiC[82], diamond[83],etc. The schematic diagram of hot-filament configuration in the reactor was shown in Figure 2.9. The tungsten filament was placed at the entrance of gas inlet and was shielded by the stainless steel tube. The filament temperature roughly ranges from 1400 to 2100 °C. With the help of hot filament various precursors such as SiH<sub>4</sub> or GeH<sub>4</sub> could be easily dissociated in to atomic radicals or ions. Then the reactive radicals or ions horizontally transport towards the surface of Si wafer and are deposited on the surface of substrate. The Si substrate was rotated during the epitaxy process to assure the uniform growth across the wafer. The HFA-CVD is important to increase the growth rate and improve the material quality especially at the low temperature growth conditions. By using the HFA-CVD the growth recipe and the corresponding sample thickness of Ge epitaxy on Si was listed in Table 2.3. The Ge thickness at the center of the wafer for each recipe was measured by Ellipsometry.

Table 2.3 The growth recipe of Ge on Si by HFA-CVD and the corresponding thickness of Ge films.

Precursors Parameters		Pressure	0.3 Torr		0.03 Torr		
Dilution Ratio	Flow Rate (sccm)	Hot filament	80 W	120 W	0 W	80 W	120 W
		Power Temperature					
1:40	5:200	350°C	25 nm	20 nm			27 nm
1:20	5:100	350°C	27 nm				
1:00	5	350°C	46 nm	44 nm	4 nm	44 nm	52 nm
1:00	5	400°C	162 nm		119 nm		142 nm

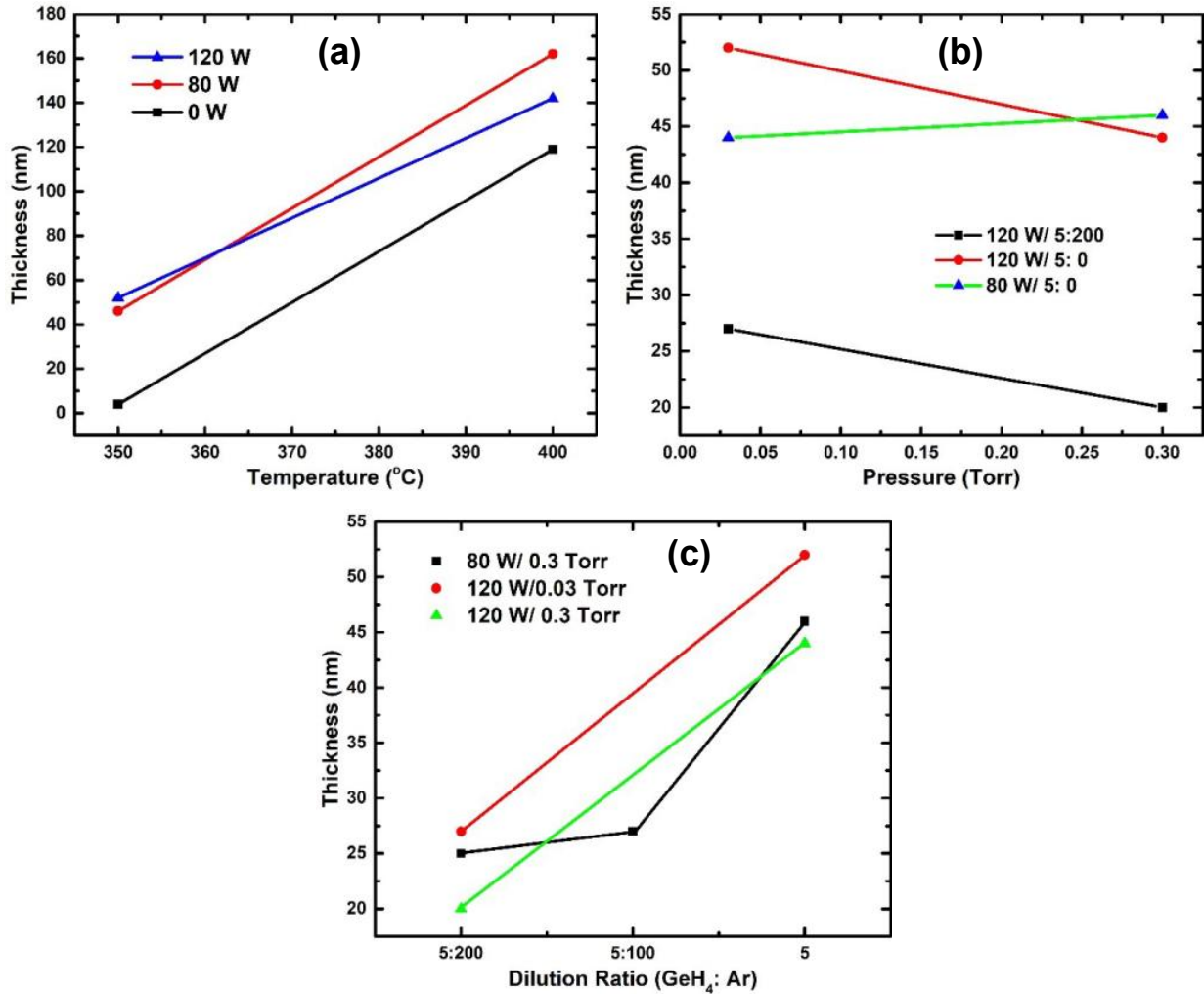


Figure 2.10 (a) The Ge thickness V.S growth temperature using HFA-CVD growth under different power supplies of hot filament. (b) The pressure-dependent growth thickness of Ge under different power supplies of hot filament and dilution ratio of precursors. (c) The Ge thickness V.S dilution ratio between GeH<sub>4</sub> and Ar under different power supplies and growth pressures.

Figure 2.10 (a) shows the thickness of one step Ge growth on Si substrate with different growth temperatures and power supplies of hot filament. The substrate temperature was changed from 350 to 400°C and the growth pressure is 0.3 Torr. With the increase of growth temperature, the thickness of Ge film increases dramatically. Compared to non-filament assisted growth (Power supply: 0 W), the hot filament helps increasing growth rate as expected. For example, when the power supply of hot filament is 80 W, the growth thickness is 46 nm, which is 11 times higher than non-filament assisted growth. However, further increasing the power supply of hot filament

from 80 to 120 W does not increase the growth thickness, which suggests that other parameters rather than power supply of hot filament have the dominating effects on growth rate. The growth pressure is suspected to have major effects on growth rate, especially for the HFA-CVD growth. High pressure in the reactor chamber corresponds to the short mean free path of precursors. For example, the mean free path of Argon is 0.6 mm at pressure of 0.3 Torr and temperature of 300 K. Since the distance between the end of filament and edge of wafer is 6 cm, the collision frequency of radicals generated by hot filament during the transportation of radicals from filament to the wafer is  $100\text{s}^{-1}$ . It is more likely that, contrary to the non-filament assisted growth, the lower pressure growth leads to the increase of growth rate because the less collision frequency of the radicals occurs during their travel from hot filament to substrate. The pressure-dependent HFA-CVD was shown in Figure 2.10 (b). When the pressure decreases from 0.3 to 0.03 Torr at 120 W power supply, the growth rate increases from 20 to 27 nm, suggesting that the pressure plays important role in HFA-CVD growth. The growth thickness of Ge as the function of dilution ratio of precursors was investigated, as shown in Figure 2.10 (C). As expected, the thickness of Ge increases dramatically with the increase of dilution ratio between  $\text{GeH}_4$  and Ar. For example, at the growth pressure of 0.3 Torr and hot-filament power supply of 120 W, the thickness of Ge increases from 20 to 44 nm when the dilution ratio increases from 5:200 to 5:0.

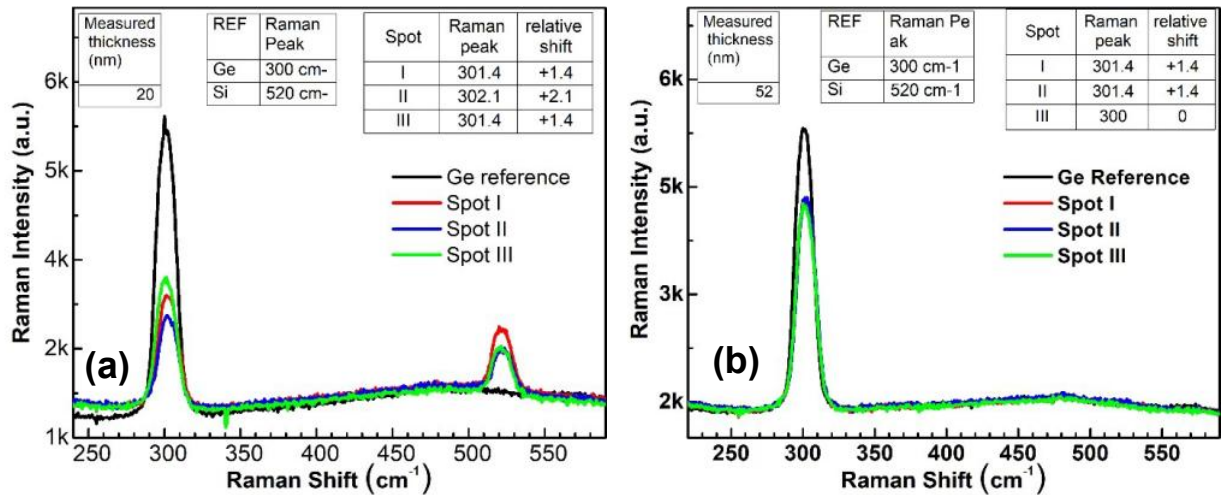


Figure 2.11 (a) The Raman spectra of 20 nm-thickness Ge on Si at three spots of substrate. (b) The Raman spectra of 52 nm-thickness Ge on Si.

The Raman spectra was studied for Ge on Si samples by using HFA-CVD growth. For the 20 nm-thickness Ge samples, three spots from the center of the wafer to the edge: I, II and III were measured in order to investigate the growth uniformity. As shown in Figure 2.11 (a) The Si-Si TO Raman peaks at all the spots were observed because of the thin Ge layer on Si. The Si-Si TO peaks originate from the Si substrate. The Ge-Ge LO peaks are shown as well on the Raman spectra while the peak intensities are much lower than the Ge-Ge peak of Ge reference. Comparing with the Raman spectra among different spots, the Si-Si peak intensity at the spot I is higher than that at the spots II and III while the Ge-Ge peak at the spot III is higher than that at the spots I and II. It indicates that the growth rate at the center of wafer is smaller than that at the edge of wafer. The radicals or ions generated by hot filament firstly arrive at the edge of wafer and deposit on the surface during the transportation. Less radicals or ions move towards the center and result in the smaller growth rate at the center compared to the growth rate at the edge of wafer. The Ge-Ge LO peaks at all the spots have a red shift compared with the Ge-Ge peak of Ge reference, indicating that the Ge layer on Si is under compressive strain. As expected, the thin Ge growth on Si at the low growth temperature results in the high compressive strain within the Ge layer. The Raman

spectra of 52 nm-thickness Ge on Si was also measured, as shown in Figure 2.11 (b). The Si-Si peaks disappear because of the thick Ge layer on Si substrate. The intensities of Ge-Ge peaks at all the spots are similar.

#### **2.4. Plasma-enhanced CVD growth of GeSn on Si**

Plasma enhanced CVD (PE-CVD) technique has been employed for Ge on Si epitaxy for high quality Ge film at low growth temperature[84][85]. Through the gas discharge, the epitaxy occurs at lower growth temperature than the traditional CVD while maintaining the material quality[86]. The low thermal budget makes PE-CVD more attractive especially for the low temperature growth condition. The precursors were ionized in the body of plasma, which makes the epitaxy less sensitive of the growth temperature. The PE-CVD growth provides another ability of freedom to control the surface reactions and material properties. Despite of its promising prospects, the PE-CVD technique faces difficulties as follows: 1) The plasma involvement in the CVD growth introduces the physical sputtering accompanying the epitaxy process on the surface. The sputtering could etch the surface and make the growth rate difficult to control. 2) Since each precursor have different dissociation energy, the ionization rates between precursors under the same power supply of plasma are different. For the alloy epitaxy of PE-CVD it is difficult to control the compositions for each constitute. 3) The uniformity of epitaxy is another critical issue for the PE-CVD growth because of the complicated controllability of uniform plasma density above the wafer, high reaction rates of ions and high collision frequency between ions on the substrate. Therefore, the parameters such as power supply of plasma, growth pressure, plasma dimension, etc. need to be optimized to address the abovementioned issues.

PE-CVD technique could be also used for GeSn epitaxy on Si or Ge. GeSn has to be grown under the low epitaxy temperature in order to avoid the segregation of Sn atoms. However, maintaining

the high material quality is a huge challenge for low temperature epitaxy. The low temperature growth also means the small growth rate, thus limiting the Sn incorporation. Benefiting from plasma enhancement, the precursors of  $\text{GeH}_4$  and  $\text{SnCl}_4$  could be easily decomposed at the low growth temperature, ensuring the sufficient growth rate for high Sn incorporation. In addition, the ions of precursors in the plasma will accelerate by the built-in electrical field in the sheath between body of plasma and substrate. As a result, the ions gain sufficient energy when arriving at the surface of film and increases the collision probability between reactive ions at the surface. Therefore, the surface mobility of adatoms enhances at low temperature and thus increases the material quality.

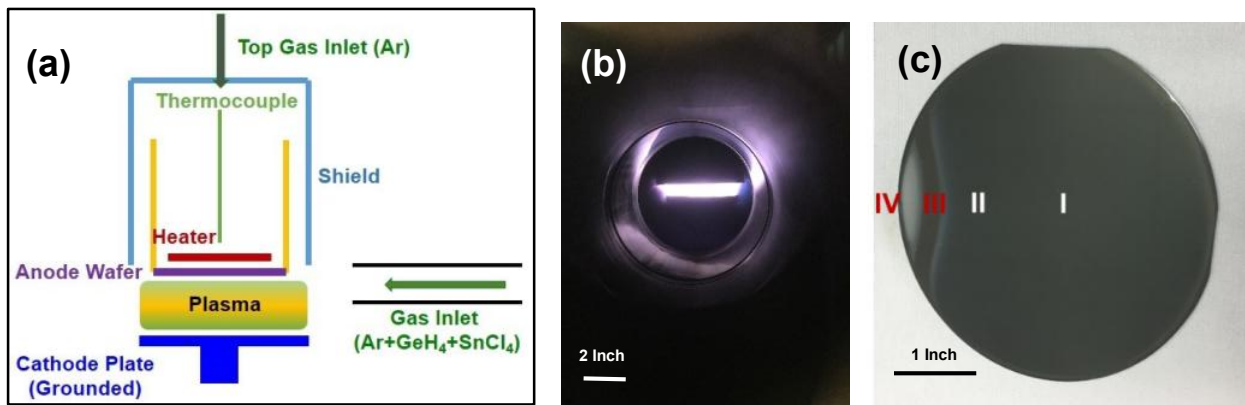


Figure 2.12 (a) The schematic diagram of PE-CVD system. (b) The generation of plasma between cathode plate and wafer in the CVD process chamber. (c) The grown GeSn on Si wafer after PE-CVD growth. Different probing spots were marked on the wafer.

The configuration of PE-CVD was schematically drawn in Figure 2.12. The Capacitively Coupled Plasma (CCP) was utilized to generate the low temperature plasma. The 13.56 MHz Radio frequency (RF) power and L-matching network were employed. The substrate wafer was powered as the anode of CCP while conductor plate in parallel with the wafer was grounded as the cathode. The plasma was generated between the wafer and cathode plate when the proper power supply applies. The body plasma was shown as the glowing region in Figure 2.12 (b), which could be divided as two areas: 1) the main area A between the wafer substrate and cathode plate and 2) the

peripheral area B close to the gas inlet. The area A was shown as yellow glowing region, mainly corresponding to the discharge of Argon and GeH<sub>4</sub> while the area B was shown as the navy blue glowing region, corresponding the discharge of GeH<sub>4</sub> and SnCl<sub>4</sub>. It could be explained that SnCl<sub>4</sub> is easily decomposed and the majority of SnCl<sub>4</sub> was immediately discharged at the edge of bulk plasma close to the gas inlet. One could tell that the generation of plasma is non-uniform, which will result in the non-uniformity of GeSn growth on Si wafer.

Two samples of 1 and 2 were grown by PE-CVD and the growth recipes were shown in Table 2.4. After the PE-CVD process, both samples were grown non-uniformly. The sample 1 was shown in Figure 2.12 (c), which is due to the non-uniform discharge of precursors in the plasma. Four probing point along the radius of wafer were marked as spot I (Center of wafer), II, III and IV (Edge of wafer), respectively.

Table 2.4 The summary of PE-CVD growth recipes of GeSn samples.

Sample	Plasma Power (W)	Temperature (°C)	Pressure (Torr)	Flow Rate (sccm) (SnCl <sub>4</sub> : GeH <sub>4</sub> : Ar)	Growth time (min)	Thickness of spot III (nm)
1	50	<b>350</b>	0.3	1:5:100	20	1154
2	50	<b>400</b>	0.3	1:5:200	20	1027

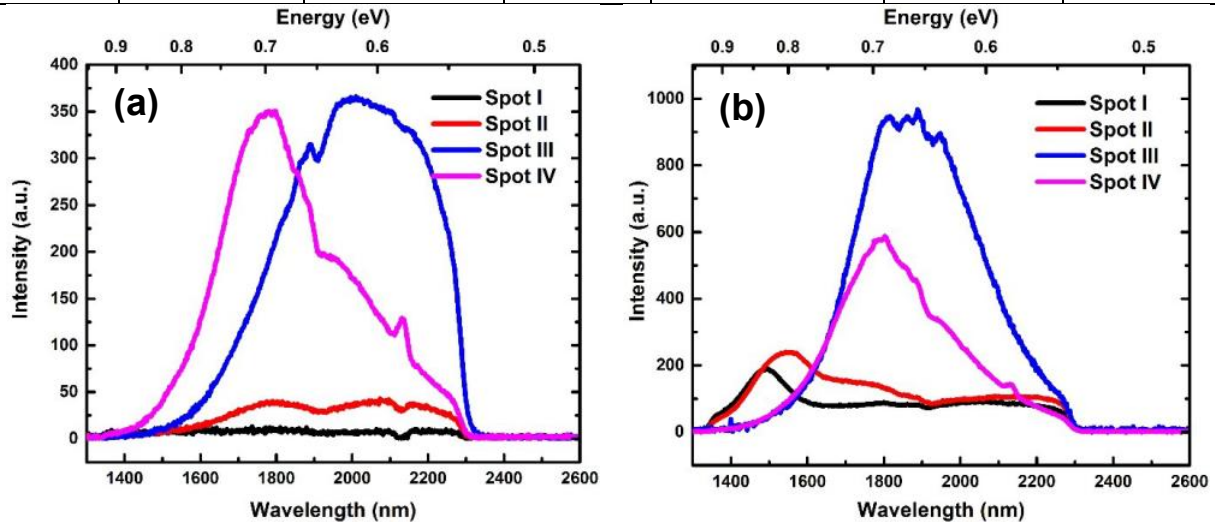




Figure 2.13 Room temperature PLs of (a) sample 1 and (b) sample 2 at different probing spots on the wafer.

The room temperature PL of two samples were conducted, as shown in Figure 2.13. The 1064 nm pulsed laser was used as pumping source with 45 kHz frequency and 6 ns pulse width. The pumping power was chosen as 500 mW. The liquid nitrogen-cooled InGaAs detector was utilized with the cut-off detecting wavelength of 2300 nm. The PL spectra of four different probing points confirmed the non-uniformity of GeSn epitaxy using PE-CVD technique. For sample 1, the PL intensities of spot III and IV are clearly observed comparing to that of spots I and II. The PL peaks of spot III and IV have a clear red shift compared with direct (1550 nm) and indirect (1776 nm) bandgap emission of Ge bulk sample, suggesting that Sn atoms are efficiently incorporated into Ge lattice sites. The fact that PL spectrum of spot III has a more red shift of wavelength (2010 nm) than that of spot IV (1776 nm) means that spot III has a higher Sn incorporation. For sample 2, the non-uniform film deposition was confirmed by PL spectra across the wafer as well. Starting from the spot I, the peak of PL emission is 1486 nm, corresponding to the emission of direct bandgap for pure Ge film under compressive strain. For spot II, the main peak shifts to 1556 nm and peak intensity increases in comparison with spot I, suggesting that Sn is incorporated into Ge lattice matrix. The spot III has the PL emission of  $\sim 1878$  nm wavelength while the spot IV has a shorter wavelength of 1800 nm. The PL peak intensity at the spot III reached the maximum. The PL spectra of both samples suggest that spot III has the highest Sn incorporation under the current PE-CVD growth. The PL peak information for both samples was summarized in Table 2.5.

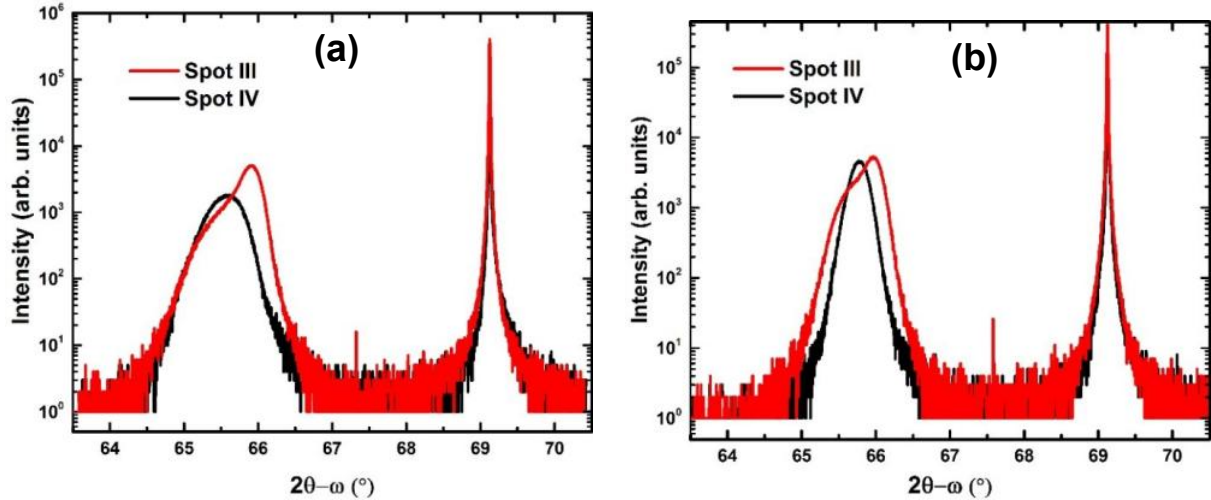


Figure 2.14 The rock curves of XRD measurements at spots III and IV of (a) sample 1 and (b) sample 2.

The XRD measurements was performed in order to investigate the GeSn crystallization on Si and Sn incorporation. XRD was performed using a Philips X'pert MRD system, which was equipped with a standard four-bounce Ge (220) monochromator and a three bounce (022) channel cut Ge analyzer crystal along with the 1.6 kW Cu  $K_{\alpha 1}$  X-ray tube with vertical line focus. For both samples 1 and 2 the spots III and IV exhibit the similar trends. Taking sample 1 as an example, a single peak at  $65.59^\circ$  was observed at Spot III while a main peak at  $65.91^\circ$  with a shoulder at  $65.39^\circ$  was shown at Spot IV. By the data fitting of XRD peaks, the Sn incorporation at spots III and IV of both samples could be estimated and the fitting results were shown in Table 2.5. The bowing parameter of lattice constant was chosen as  $-0.066 \text{ \AA}$  for the data fitting of Sn incorporation. Considering that the thicknesses of GeSn films measured by Ellipsometry are beyond  $1 \mu\text{m}$ , GeSn could be treated as the fully relaxed film.

Table 2.5 The summary of Sn compositions and PL peak positions of samples 1 and 2.

Sample	Spot	Sn composition (%)	PL peak position (nm)
1	III	1/6.2	1966 – 2100
	IV	3.5	1776
2	III	0.3/3.8	1796 – 1952
	IV	2	1800

The Raman spectroscopy of sample 2 was performed in order to double check the crystallization at different spots, which was shown in Figure 2.15. The Raman peaks of spot I, II and III exhibit a clear Raman shift compared with that of Ge reference. The Raman peak of spot III has the Raman shift of  $-4.5 \text{ cm}^{-1}$ , corresponding to the Sn incorporation of 5.1% for fully relaxed GeSn films[87]. The absorption coefficient for GeSn was measured by Ellipsometry, as shown in Figure 2.16 (a). The spot I exhibits pure Ge absorption coefficient while spot III shows an obvious red shift of absorption edge, suggesting the incorporation of Sn. The Ellipsometry results are consistent with PL, XRD, and Raman results. At the spot III in Figure 2.16 (a), both direct and indirect bandgap absorption were observed. When photon energy  $h\nu$  exceeds the direct bandgap energy  $E_g^\Gamma$ , the direct bandgap transition is dominated over the indirect bandgap transition. Near the direct band edge, the absorption could be expressed as[88],

$$(\alpha h\nu)^2 = A(h\nu - E_g^\Gamma) \quad \text{Equation 2.1}$$

where  $\alpha$  is the absorption coefficient of direct bandgap transition,  $h\nu$  is the photon energy,  $A$  is the constant and  $E_g^\Gamma$  is the direct bandgap energy. By fitting the absorption coefficient of band edge at spot III, the direct bandgap energy  $E_g^\Gamma$  could be extracted. Figure 2.16 (b) shows the data fitting process of  $E_g^\Gamma$ , by drawing the relationship between  $(\alpha h\nu)^2$  and  $h\nu$ . After linear data fitting of Figure 2.16 (b), the  $E_g^\Gamma$  was extracted as 0.735 eV.

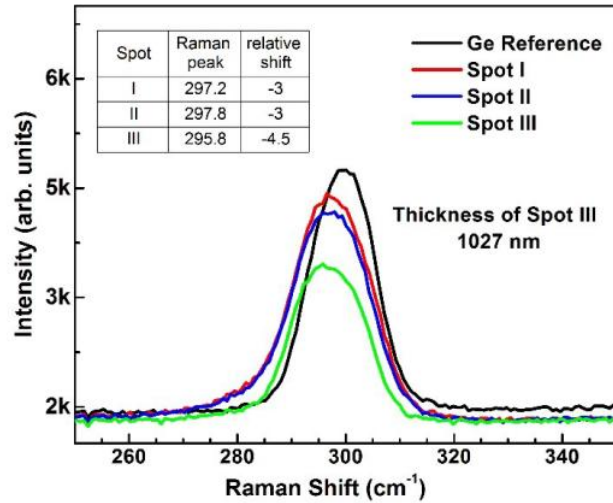


Figure 2.15 Raman spectroscopy at the spots of I, II and III of sample 2.

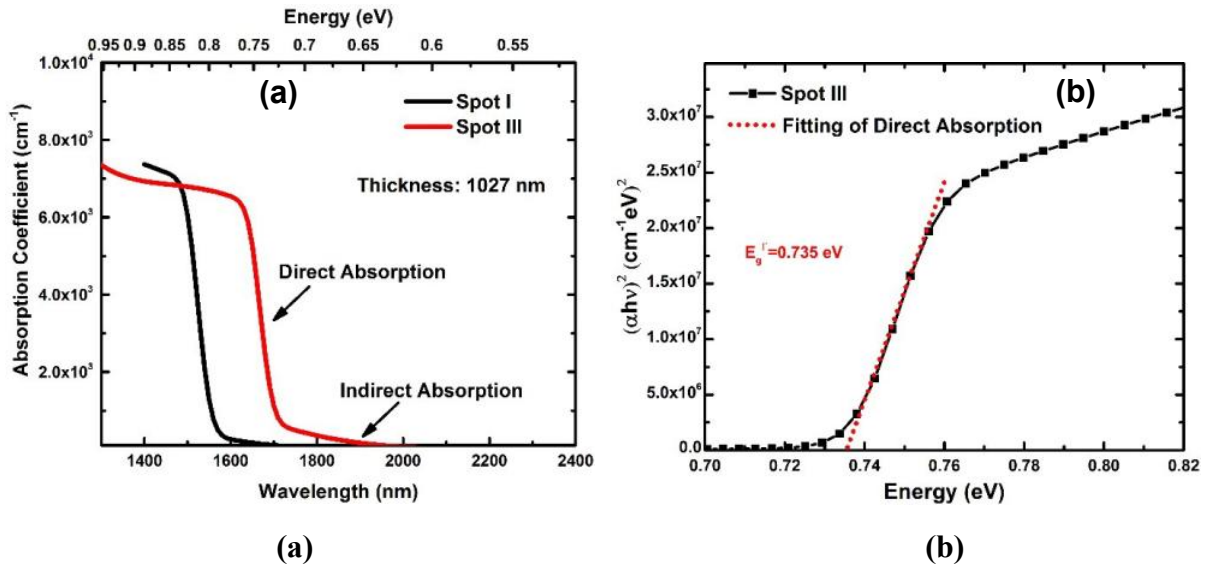


Figure 2.16 (a) The Ellipsometry measurements at spots I and III of sample 2. (b) The data fitting of direct absorption coefficient for direct bandgap energy at the spot III of sample 2.

## 2.5. GeSn growth on Ge buffer

The GeSn growth on Ge buffer of Si substrate was investigated using standard UHV-CVD system in order to pursue the high quality and high Sn incorporation. Prior to the GeSn epitaxy, the high quality Ge buffer was grown on Si substrate by low/high temperature two-step method. The GeSn film was then grown on Ge buffer at low temperature condition. The growth recipe was listed in Table 2.6.

Table 2.6 The summary of growth recipe of GeSn on Ge buffered Si substrate.

Sample	Layer	Temperature (°C)	Pressure (Torr)	Flow Rate (sccm) (SnCl <sub>4</sub> : GeH <sub>4</sub> : Ar)	Growth Time (min)
Ge	1 <sup>st</sup>	375	1	0:5:200	10
	2 <sup>nd</sup>	600	1	0:2.5:200	20
GeSn		250-300	1 or 2	(0.03-0.07):(10-20):200	60 or 120

The flow fraction of SnCl<sub>4</sub> is a critical parameter for the GeSn growth and has multiple effects on the GeSn epitaxy, which were listed as follows:

1. Surface etching by the byproducts HCl. The reaction between SnCl<sub>4</sub> and GeH<sub>4</sub> generates the gaseous HCl as a byproduct, which has an aggressive chemical etching of Ge atoms on the surface[62].
2. Sn segregation on the surface. For example, if the flow fraction of SnCl<sub>4</sub> is too high, the excess Sn atoms will float and segregate on the surface. The Sn segregation will roughen the surface and deteriorate the material quality[24].
3. The surfactant effects of Sn. A certain amount of Sn has been reported as a surfactant that smoothed the GeSn surface by enhancing Ge diffusivity[89].

We have explored a wide range of flow fractions of SnCl<sub>4</sub> ( $\frac{F_{SnCl_4}}{F_{SnCl_4} + F_{GeH_4} + F_{Ar}}$ ) from 10<sup>-2</sup> to 10<sup>-4</sup> order of magnitude, where the  $F_{SnCl_4}$ ,  $F_{GeH_4}$  and  $F_{Ar}$  indicate the flow rate of SnCl<sub>4</sub>, GeH<sub>4</sub> and Ar, respectively. Finally, it turns out that the low flow fraction of SnCl<sub>4</sub> (i.e. 10<sup>-4</sup>) results in smooth surface and high quality of GeSn. However, the Sn incorporation maintains the constant with variable SnCl<sub>4</sub> flow fraction at the current range, which means that other parameters such as substrate temperature dominate the effects on Sn incorporation. Hereby, we obtained a high quality GeSn sample on Ge buffer by using SnCl<sub>4</sub> flow fraction of 1.4\*10<sup>-4</sup>, which is the minimum limitation of mass flow controllers. The substrate temperature and growth pressure are 250°C and

2 Torr, respectively. The growth time is 60 minutes. After the growth the thickness of GeSn was obtained as 234 nm by Ellipsometry.

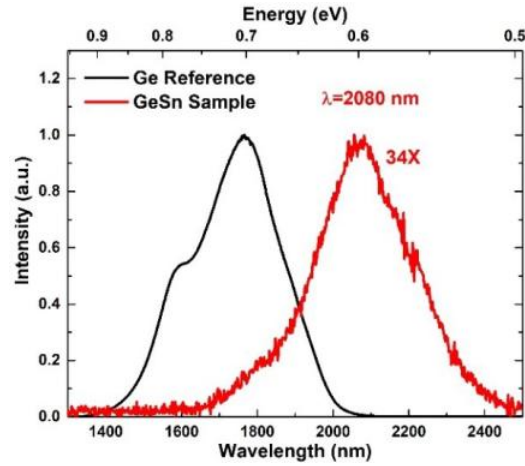


Figure 2.17 The room-temperature PL spectra of GeSn and bulk Ge reference.

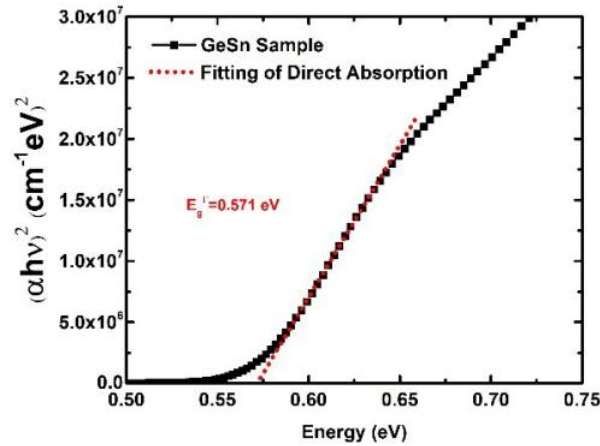


Figure 2.18 The data fitting of direct absorption coefficient for direct bandgap energy.

The room temperature PL was measured in order to investigate the optical properties of GeSn. The 1064 nm pulsed laser with 45 kHz frequency and 6 ns pulse width was used as the pumping source. The pumping power was chosen as 50 mW. As shown in Figure 2.17, a pronounced red shift of the PL peak of GeSn was observed compared to the PL of bulk Ge, suggesting an effective Sn incorporation into Ge lattice sites. The main PL peak was 2080 nm (0.6 eV), corresponding to the light emission of direct bandgap. Through Gaussian data fitting the direct bandgap energy was

extracted as 0.587 eV. The indirect bandgap on the PL spectra was not resolved. Figure 2.18 shows the direct absorption of coefficient for GeSn measured by Ellipsometry. By data fitting of the absorption coefficient, the direct bandgap energy was obtained as 0.571 eV, which is in agreement with the PL results.

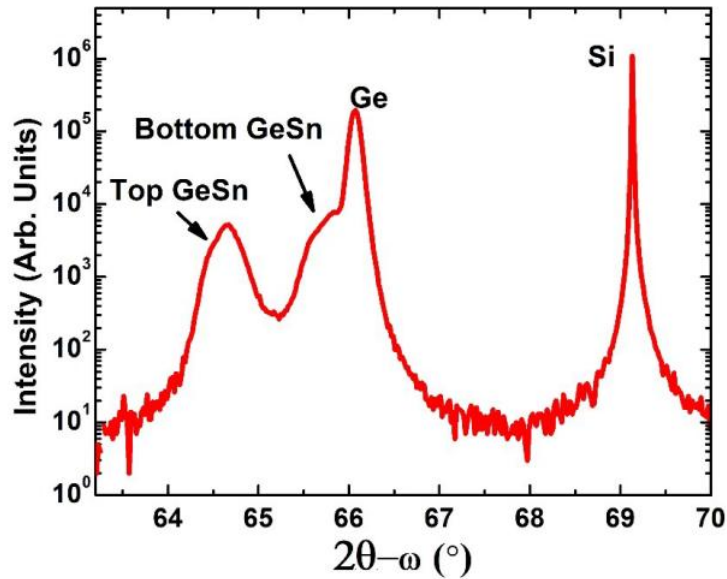


Figure 2.19 The rocking curve of XRD along (004) plane for GeSn sample.

The crystallization of GeSn was investigated by the XRD measurements. The symmetric rocking curve of GeSn sample along (004) plane was shown in Figure 2.19. Both peaks of Si substrate and Ge buffer were shown on the rocking curve, which are located at the diffraction angle of 69.12° and 65.99°, respectively. Below the diffraction angle of Ge buffer, two peaks of GeSn were observed, suggesting that two layers of GeSn were grown on top of Ge buffer. The angles of 65.83° and 64.67° correspond to the bottom and top GeSn, respectively. The Sn incorporation was estimated from rocking curve of XRD. The initial Sn incorporation range of 5-8% was obtained from the results of PL and Ellipsometry. Within this range of Sn incorporation the critical thickness was calculated from 109 nm (8%) to 334 nm (5%) according to the People- Bean model. Considering that the thickness of grown GeSn was 234 nm, the GeSn film on Ge buffer could be

considered as the pseudomorphic growth. Then after the data fitting of rock curve the Sn incorporations of the bottom and top GeSn were obtained as 1.4% and 8.1%, respectively. The summary of data fitting of GeSn film was listed in Table 2.7.

Table 2.7 The summary of data fitting results of GeSn films.

GeSn	XRD Angle (°)	Lattice constant (Å)		Sn Composition (%)	Strain (%)
		Out of Plane	In Plane		
Bottom layer	65.83	5.6703	5.6656	1.4	-0.05
Top layer	64.67	5.7607	5.6656	8.1	-0.95

### Chapter 3. Band structure of GeSn

#### 3.1. K.P method for GeSn band structure

Band structure, especially near the band edge is of great importance for the analysis of optical properties of optoelectronic semiconductors such as the radiative recombination, optical gain and quantum efficiency, etc. Several methods were proposed involving tight binding[90], orthogonalized plane wave[91], pseudopotential approach[92] and K.P method[93]. For example, tight binding method has been widely utilized to calculate the band structure of entire Brillouin Zone on the basis of localized atomic orbitals. However, the center of Brillouin zone,  $\Gamma$  point ( $k=0$ ) is very important for the optoelectronic devices, most of which is made of direct bandgap materials. For the direct bandgap materials such as GaAs, InP, etc, the optical transition primarily occurs between the minima of conduction band and the maxima of valence band. The radiative recombination is efficient for these direct bandgap materials. In this case the K.P method is much desirable to analysis the direct bandgap materials because the K.P method focused on the description of the near-edge band structure. The simplicity and reliability of calculation makes K.P method more attractive.



The K.P method was firstly proposed by Bardeen and Seitz and then well developed by Dresselhaus[94], Kane[95]. K.P method is also known as the effective mass approximation or envelop function approximation which bases on the perturbation theory of quantum mechanics. It requires the minimal sets of empirical parameters to describe the near-edge band structure. Until now the K.P method has already been the widespread approach among the III–V compound semiconductors and their alloys[96]. The simplest model of band structure is parabolic model, which treats all the energy dispersion as parabola, as depicted in Figure 3.1 (a). The Kane method takes into account the four core bands: one conduction band (CB) and three valence bands: heavy hole (HH), light hole (LH) and splitting orbit (SO) band. The Kane model ignores the rest of bands, as shown as Figure 3.1 (b). In Kane model one more term of splitting orbit interaction is added into Hamilton, thus modifying the parabolic model near the center zone ( $k=0$ ). In Luttinger-Kohn model the remote bands were further introduced as the perturbation of four core bands, as shown in Figure 3.1 (c). The four core bands of CB, HH, LH, SO were classified as the class A and the rest of the bands were treated as the Class B. The Luttinger-Kohn model is a more practical model to calculate band structure at the  $k \neq 0$  region.

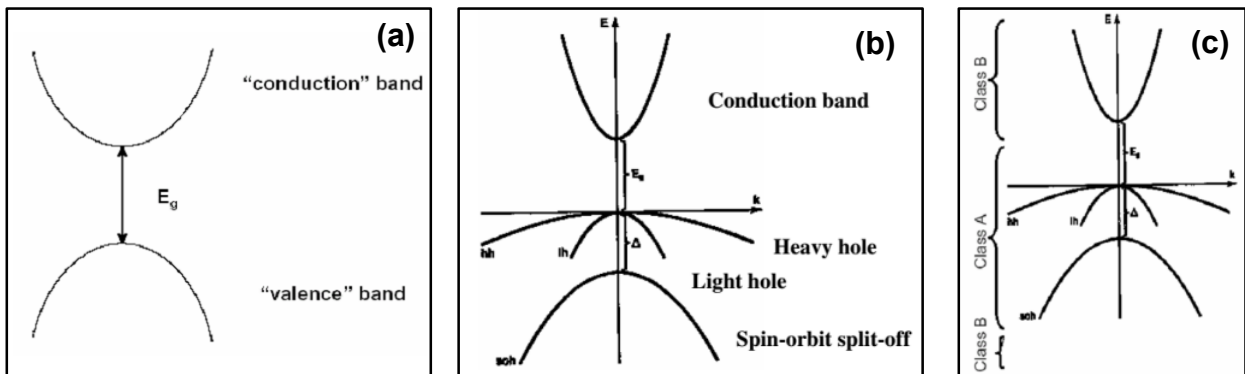


Figure 3.1 (a) parabolic model of two bands. (b) Kane model of four core bands. (c) Luttinger-Kohn model of the bands classified into A and B.

In this chapter, the general calculation procedure based on the K.P method could be described as follows[93]:

- 1) The wave function based on Bloch theorem was introduced that consists of a free electron wave and a periodic part.
- 2) The conventional Schrodinger equation was modified by adding the splitting-orbit interaction. The Bloch wave function was put into the modified Schrodinger equation. A K.P perturbation terms appears in the Hamilton. The energy dispersion at point  $k=0$  was calculated using Kane's model.
- 3) The perturbation theory and Luttinger-Kohn model were applied simultaneously to generate Luttinger-Kohn Hamiltonian matrix, the core part of Luttinger-Kohn model.
- 4) The eigenvalues and eigenfunctions of Luttinger-Kohn Hamiltonian matrix were solved to obtain the energy dispersion.

### 3.1.1. Kane Model

According to Bloch Theorem, the wave function in the semiconductors can be written as:

$$\Psi(\mathbf{r}) = e^{i\mathbf{k}\cdot\mathbf{r}}u(\mathbf{r}) \quad \text{Equation 3.1}$$

where  $u(\mathbf{r}) = u(\mathbf{r} + \mathbf{R})$  is the periodic function due to the potential symmetry of semiconductor materials.  $u(\mathbf{r})$  has the same periodicity as the crystal lattice constant.  $\mathbf{R}$  is the period of potential value. When putting Bloch wave function and adding splitting orbit interaction into the typical Schrodinger equation, Schrodinger equation can be modified as,

$$\left( H_0 + \frac{\hbar}{m_0} \mathbf{K} \cdot \mathbf{P} + \frac{\hbar}{4m_0^2c^2} \nabla V \times \mathbf{P} \cdot \boldsymbol{\sigma} \right) u(\mathbf{r}) = \left( E(\mathbf{k}) - \frac{\hbar^2 k^2}{2m_0} \right) u(\mathbf{r}) \quad \text{Equation 3.2}$$

The second term  $\frac{\hbar}{m_0} \mathbf{K} \cdot \mathbf{P}$  on the left side of equation is K.P perturbation and the third term

$\frac{\hbar}{4m_0^2c^2} \nabla V \times \mathbf{P} \cdot \boldsymbol{\sigma}$  is spin orbit interaction.  $u(\mathbf{r})$  is the periodic function, which could be regarded

as the superposition of an array of complete base functions. Hereby the band edge functions at  $k=0$  was employed as the base functions. The base functions should be completed and orthogonal with each other. In Kane model only four core band-edge functions (CB, HH, LH, SO) were included,

and these band-edge wave functions are chosen as the base functions. To simplify the four base functions, quasi-hydrogen atom model was applied because the electron wave functions at  $k=0$  of conduction bands are S state-like whilst the hole wave functions at  $k=0$  of valance bands are P state-like. Therefore the base function could be written using the following spherical harmonic function in hydrogen atom model. The self-spin effects are taken into account, which were notated as  $\uparrow$  and  $\downarrow$ .

$$\begin{aligned} u_1 = Y_{00}^{00} = |S \uparrow\rangle \quad u_2 = |S \downarrow\rangle \quad u_3 = Y_{00}^{11} = \left| \frac{X-iY}{\sqrt{2}} \uparrow \right\rangle \quad u_4 = \left| -\frac{X+iY}{\sqrt{2}} \downarrow \right\rangle \\ u_5 = Y_{00}^{10} = |Z \uparrow\rangle \quad u_6 = |Z \downarrow\rangle \quad u_7 = Y_{00}^{11} = \left| -\frac{X+iY}{\sqrt{2}} \uparrow \right\rangle \quad u_8 = \left| \frac{X-iY}{\sqrt{2}} \downarrow \right\rangle \end{aligned} \quad \text{Equation 3.3}$$

Based on these functions the Hamiltonian matrix becomes

$$H = \begin{pmatrix} \bar{H} & 0 \\ 0 & \bar{H} \end{pmatrix} \text{ and } \bar{H} = \begin{pmatrix} E_g & 0 & kP & 0 \\ 0 & E_p - \frac{\Delta}{3} & \sqrt{2} \frac{\Delta}{3} & 0 \\ kP & \sqrt{2} \frac{\Delta}{3} & E_p & 0 \\ 0 & 0 & 0 & E_p + \frac{\Delta}{3} \end{pmatrix} \quad \text{Equation 3.4}$$

where  $E_g$ ,  $P$ , and  $\Delta$  represent the band gap, Kane's parameter and spin orbit splitting energy, respectively.  $E_p = -\Delta/3$  is the reference energy. Solving Schrodinger equation yields energy dispersion near band edge ( $k=0$ ), which reads as

$$\begin{aligned} E_c(k) = E_g + \frac{\hbar^2 k^2}{2m_0} + \frac{k^2 P^2 \left( E_g + 2\frac{\Delta}{3} \right)}{E_g (E_g + \Delta)} \quad (CB) \quad E_{hh}(k) = \frac{\hbar^2 k^2}{2m_0} \quad (HH) \\ E_c(k) = \frac{\hbar^2 k^2}{2m_0} - \frac{2k^2 P^2}{3E_g} \quad (LH) \quad E_{so}(k) = -\Delta + \frac{\hbar^2 k^2}{2m_0} - \frac{k^2 P^2}{3(E_g + \Delta)} \quad (SO) \end{aligned} \quad \text{Equation 3.5}$$

### 3.1.2. Luttinger-Kohn Model

Since Kane model has been solved to obtain the energy dispersion near  $k=0$  area, the remote bands (noted as class B) compared to four core ones (noted as class A) were further taken into consideration in Luttinger-Kohn model as the perturbation terms. After considering all the

interaction among bands the more accurate band structure at  $k \neq 0$  area could be acquired. Similar to Kane's model, the base functions in class A (CB, HH, LH, SO) including spin effects are:

$$\begin{aligned} u_1^A &= |S \uparrow\rangle & u_2^A &= |S \downarrow\rangle & u_3^A &= \left| \frac{3}{2}, \frac{3}{2} \right\rangle & u_4^A &= \left| \frac{3}{2}, \frac{1}{2} \right\rangle \\ u_5^A &= \left| \frac{3}{2}, -\frac{1}{2} \right\rangle & u_6^A &= \left| \frac{3}{2}, -\frac{3}{2} \right\rangle & u_7^A &= \left| \frac{1}{2}, \frac{1}{2} \right\rangle & u_8^A &= \left| \frac{1}{2}, -\frac{1}{2} \right\rangle \end{aligned} \quad \text{Equation 3.6}$$

Employing Lowdin's perturbation theory yields the hermite Luttinger-Kohn Hamiltonian as

$$H_{L-K} = \begin{pmatrix} T & 0 & -\frac{1}{2}k_x P & \sqrt{\frac{2}{3}}k_z P & \frac{1}{\sqrt{6}}k_x P & 0 & -\frac{1}{\sqrt{3}}k_z P & -\frac{1}{\sqrt{3}}k_x P \\ 0 & T & 0 & -\frac{1}{\sqrt{6}}k_x P & \sqrt{\frac{2}{3}}k_z P & -\frac{1}{2}k_x P & -\frac{1}{\sqrt{3}}k_x P & -\frac{1}{\sqrt{3}}k_z P \\ -\frac{1}{2}k_x P & 0 & U+Q & -S & R & 0 & -\frac{S}{\sqrt{2}} & \sqrt{2}R \\ \sqrt{\frac{2}{3}}k_z P & -\frac{1}{\sqrt{6}}k_x P & -S^* & U-Q & 0 & R & -\sqrt{2}Q & \sqrt{\frac{3}{2}}S \\ \frac{1}{\sqrt{6}}k_x P & \sqrt{\frac{2}{3}}k_z P & R^* & 0 & U-Q & S & \sqrt{\frac{3}{2}}S^* & \sqrt{2}Q \\ 0 & -\frac{1}{2}k_x P & 0 & R^* & S^* & U+Q & -\sqrt{2}R^* & -\sqrt{\frac{1}{2}}S^* \\ -\frac{1}{\sqrt{3}}k_z P & -\frac{1}{\sqrt{3}}k_x P & -\frac{S^*}{\sqrt{2}} & -\sqrt{2}Q^* & \sqrt{\frac{3}{2}}S & -\sqrt{2}R & U+\Delta & 0 \\ -\frac{1}{\sqrt{3}}k_x P & -\frac{1}{\sqrt{3}}k_z P & \sqrt{2}R^* & \sqrt{\frac{3}{2}}S^* & \sqrt{2}Q^* & -\sqrt{\frac{1}{2}}S & 0 & U+\Delta \end{pmatrix} \quad \text{Equation 3.7}$$

Where

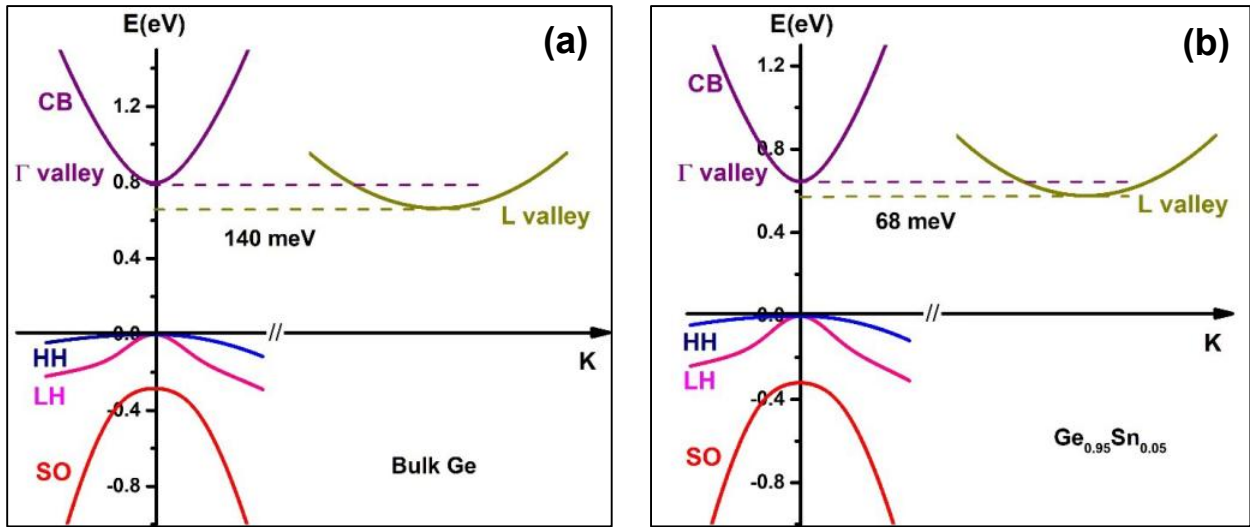
$$k_{\pm} = k_x \pm ik_y, T = E_c + \frac{\hbar^2 k^2}{2m_0}, U = \frac{\hbar^2 \gamma_1}{2m_0} (k_x^2 + k_y^2 + k_z^2), Q = \frac{\hbar^2 \gamma_2}{2m_0} (k_x^2 + k_y^2 - 2k_z^2)$$

$$R = \frac{\hbar^2}{2m_0} [-\sqrt{3}\gamma_2(k_x^2 - k_y^2) + i2\sqrt{3}\gamma_3 k_x k_y], S = \frac{\hbar^2 \gamma_3}{2m_0} \sqrt{3}(k_x - ik_y)k_z$$

In the above Hamiltonian matrix,  $\gamma_1, \gamma_2, \gamma_3$  note as Luttinger parameters, which could be determined experimentally. In this chapter the Luttinger-Kohn Hamiltonian has been applied to calculate the GeSn bulk material with various Sn composition. All the necessary parameters occurred in the Hamiltonian could be found in Appendix A.

The band structures of GeSn with Sn compositions of 0%, 5% and 15% using the 8-band Luttinger-Kohn model were shown in Figure 3.2. The four bands of CB, HH, LH, SO were included. Starting

from the bulk Ge in Figure 3.2 (a), The  $E_g^{\Gamma\text{-HH}}$  (direct) is 0.8 eV while the  $E_g^{\text{L-HH}}$  (indirect) locates at 140 meV lower than the  $E_g^{\Gamma\text{-HH}}$ . The splitting orbit energy  $E^{\text{HH-SO}}$  for bulk Ge is 0.28 eV. For  $\text{Ge}_{0.95}\text{Sn}_{0.05}$  alloy of Figure 3.2 (b), both direct and indirect bandgap decrease simultaneously due to the Sn incorporation. The  $E_g^{\Gamma\text{-HH}}$  decreases to 0.65 eV and The  $E_g^{\text{L-HH}}$  reduces to 0.58 eV. The fact that the  $E_g^{\text{L-HH}}$  is 68 meV lower than  $E_g^{\Gamma\text{-HH}}$  indicates that the direct bandgap shrinks faster than indirect bandgap due to the Sn incorporation. Meanwhile, the  $E^{\text{HH-SO}}$  increases to 0.32 eV. For  $\text{Ge}_{0.85}\text{Sn}_{0.15}$  alloy, the  $E_g^{\Gamma\text{-HH}}$  and  $E_g^{\text{L-HH}}$  further reduce to 0.37 and 0.42 eV, respectively, as shown in Figure 3.2 (c). The GeSn alloy has already become the direct bandgap. Meanwhile, the  $E^{\text{HH-SO}}$  increases to 0.39 eV, which is larger than the direct bandgap  $E_g^{\Gamma\text{-HH}}$ . The large value of splitting orbit energy helps suppress the nonradiative Auger process in which the energy and momentum of an electron-hole pair in the process of radiative recombination are transferred to a third carrier in either conduction or valance band.



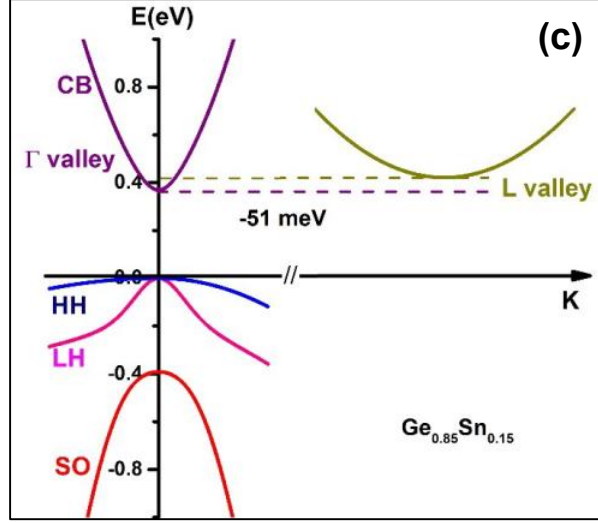


Figure 3.2 The band structure of the unstrained (a) bulk GeSn, (b)  $\text{Ge}_{0.95}\text{Sn}_{0.05}$  and (c)  $\text{Ge}_{0.85}\text{Sn}_{0.15}$  at room temperature.

### 3.2. Temperature-dependent bandgap of GeSn

The direct ( $E_g^\Gamma$ ) and indirect ( $E_g^L$ ) bandgaps were calculated as the function of Sn incorporation.

The temperature of 300 and 10 K was applied in the calculation. The direct  $E_g^\Gamma(\text{GeSn})$  and indirect

$E_g^L(\text{GeSn})$  bandgaps could be expressed as

$$E_g^\Gamma(\text{GeSn}) = (1 - x) * E_g^\Gamma(\text{Ge}) + x * E_g^\Gamma(\text{Sn}) + b^\Gamma * x * (1 - x) \quad \text{Equation 3.8}$$

$$E_g^L(\text{GeSn}) = (1 - x) * E_g^L(\text{Ge}) + x * E_g^L(\text{Sn}) + b^L * x * (1 - x) \quad \text{Equation 3.9}$$

where  $x$  is the Sn composition,  $b^\Gamma$  and  $b^L$  are the bowing parameters of direct and indirect bandgaps, respectively. Both  $E_g^{\Gamma,L}(\text{Ge})$  and  $E_g^{\Gamma,L}(\text{Sn})$  are temperature dependent and the value could be found in Table A1 of Appendix A. The  $b^\Gamma$  and  $b^L$  are very critical in this calculation and are also temperature dependent. The value of  $b^\Gamma$  and  $b^L$  have been predicated by various research groups although none of the results has been reached the agreement[97][98][99]. In this section, the  $b^\Gamma = 1.94 \text{ eV}$  [98] and  $b^L = 1.23 \text{ eV}$  [98] were adopted at the room temperature (300 K) while the  $b^\Gamma = 2.61 \text{ eV}$  [100] and  $b^L = 0.8 (\pm 0.06) \text{ eV}$  [100] were chosen at temperature of 10 K. The calculation results were drawn in Figure 3.3. At both temperatures of 300 and 10 K, the direct

$E_g^\Gamma$  and indirect  $E_g^L$  bandgaps decrease with the increase of Sn incorporation while the  $E_g^\Gamma$  shrinks faster than  $E_g^L$ . The crossing between  $E_g^\Gamma$  and  $E_g^L$  occurs at the critical Sn concentration. Beyond the critical Sn content the GeSn becomes direct bandgap. The critical Sn content was calculated as 10.5 % at the temperature of 300 K. The corresponding bandgap energy ( $E_g^{\Gamma,L}$ ) was calculated as 0.489 eV. However, at the temperature of 10 K the critical Sn content reduces to 6.3% and the bandgap energy was 0.656 eV. The two critical Sn contents at temperature of 300 and 10 K divide the Sn composition into three areas: 1) Sn content < 6.3%, in which GeSn is indirect bandgap at all the temperature range; 2) 6.3% < Sn content < 10.5%, in which the GeSn is indirect bandgap material at 300 K and becomes direct bandgap material at 10 K; 3) Sn content > 10.5%, in which the GeSn is direct bandgap material at all temperature range. One thing should be noticed that different adoption of bowing parameters yields different critical Sn incorporation. However, the calculation reveals that the directness of GeSn material is not only Sn-composition dependent but also temperature dependent.

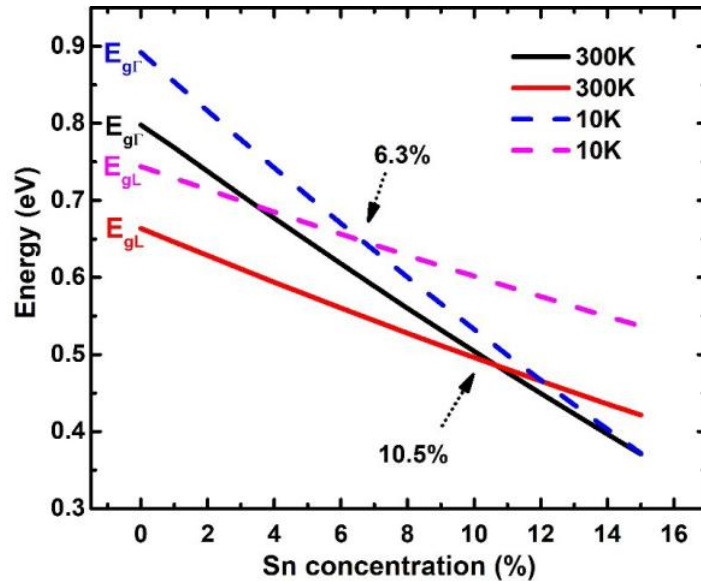


Figure 3.3 The bandgap energy as the function of Sn concentration at the temperature of 300 and 10 K.

Since the critical Sn content at 300 K is 10.5 %, the band structure of  $\text{Ge}_{0.9}\text{Sn}_{0.1}$  at the temperature of 300 and 10 K were calculated as the typical example. By using the 8 band Luttinger-Kohn model of K.P method the calculation results including CB, HH, LH and SO were shown in Figure 3.4. At the temperature of 300 K, the indirect bandgap  $\text{Ge}_{0.9}\text{Sn}_{0.1}$  was observed with the energy separation between  $\Gamma$  and L valleys only 7 meV, which is smaller than the thermal energy  $1kT$  (26 meV) of the room temperature. Therefore, the  $\text{Ge}_{0.9}\text{Sn}_{0.1}$  could be considered as the quasi-direct bandgap material at the room temperature. The direct bandgap ( $\Gamma$ ) of 0.5 eV was obtained for  $\text{Ge}_{0.9}\text{Sn}_{0.1}$  alloy at 300 K. Using the simple parabolic model of conduction bands, the curvature of  $\Gamma$  valley is smaller than the curvature of L valley, which is due to the difference of effective masses of electrons. The L valley has larger effective mass than the  $\Gamma$  valley. Therefore, the density of states of L valley of conduction band is larger than that of the  $\Gamma$  valley, which means the L valley could accommodate more electrons than  $\Gamma$  valley. In contrast, at the temperature of 10 K, the  $\text{Ge}_{0.9}\text{Sn}_{0.1}$  becomes truly direct bandgap material with the  $\Gamma$  valley 69 meV lower than the L valley. The direct bandgap was calculated as 0.533 eV. The calculation results indicate that the L valley has more sensitivity of temperature. When the temperature cools down from 300 to 10 K, both L and  $\Gamma$  valley increase while the L valley increases faster than the  $\Gamma$  valley. Therefore, the quasi-direct bandgap material of  $\text{Ge}_{0.9}\text{Sn}_{0.1}$  at room temperature becomes direct bandgap material at the temperature of 10 K.



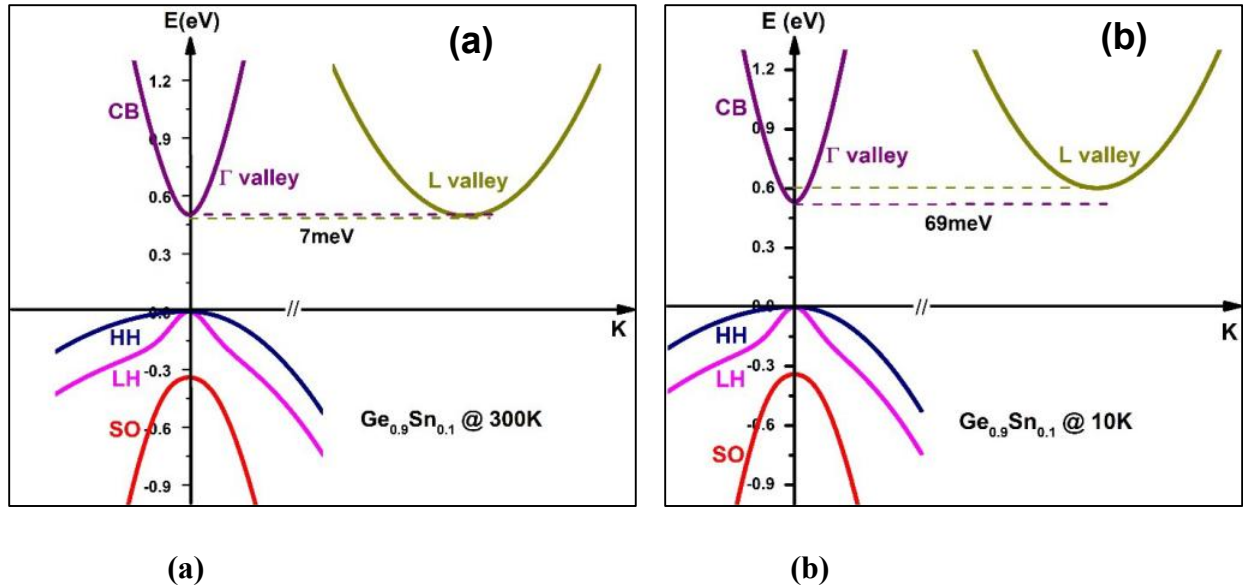


Figure 3.4 The band structure of unstrained  $\text{Ge}_{0.9}\text{Sn}_{0.1}$  at (a) room temperature (300 K) and (b) 10 K.

### 3.3. Strain effects on the GeSn band structure

The strain plays an important role in the band structure engineering[101][102]. Normally the strain lowers the symmetry of the crystal structure and affects the periodic potential of electrons or holes. Therefore, the band structure could be changed by the strains. For example, the symmetry of crystal structure could be reflected by the band degeneracy. In unstrained semiconductor the HH and LH merge at maximum of the valence band because of the high symmetry of crystal. If taking the spin counterpart into consideration, the maximum spot of HH and LH is fourfold degenerate. When the strain is applied into the semiconductor, the symmetry of crystal is broken, leading to the splitting of HH and LH on the top of valence band. The strain in the semiconductor also alters the effective masses of electrons and holes, which are another important parameters characterizing semiconductor properties[101]. For simplicity, a special case of bilateral strain is mainly focused, which was schematically drawn in Figure 3.5. The growth direction of epitaxial layer was marked as z axis and the direction perpendicular to the growth direction was marked as x or y axis. The planes parallel to the z axis were named as out of plane and the planes parallel to x(y) direction

were named as in plane. In term of the in-plane strain three cases were considered: 1) The compressive strain of epitaxial layer. The in-plane lattice constant is larger than that of substrate (Figure 3.5 (a)); 2) The no strain of epitaxial layer. The in-plane lattice constant is matched with the substrate (Figure 3.5 (b)); 3) The tensile strain of epitaxial layer. The in-plane lattice constant is smaller than that of substrate (Figure 3.5 (c)).

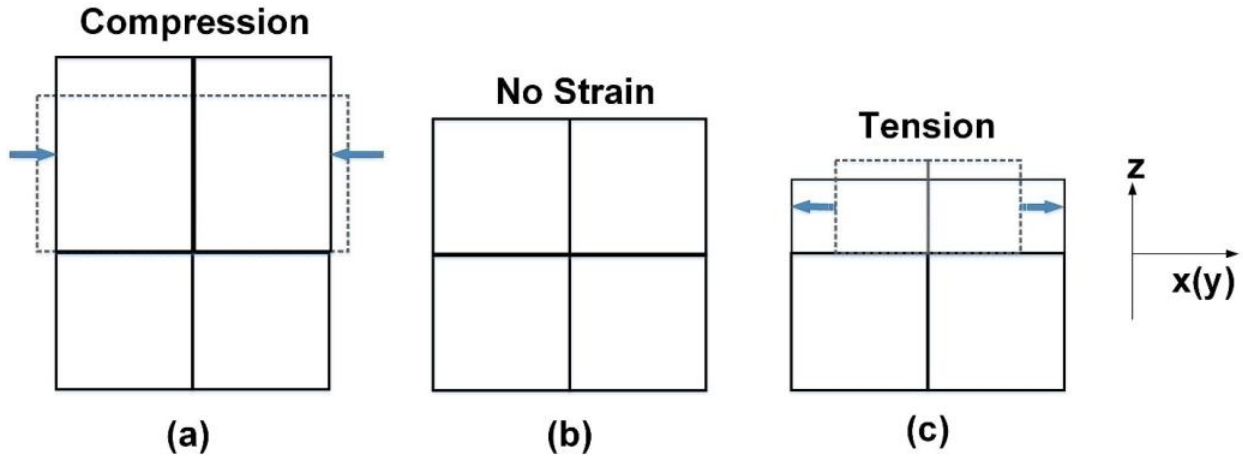


Figure 3.5 The schematic diagram of (a) compressive strain (b) no strain and (c) tensile strain for the epitaxial growth.

The degree of biaxial strain was defined as

$$\varepsilon_{xx} = \varepsilon_{yy} = \frac{a_0 - a}{a} \quad \varepsilon_{zz} = -\frac{C_{12}}{C_{11}}(\varepsilon_{xx} + \varepsilon_{yy}) \quad \varepsilon_{xy} = \varepsilon_{yz} = \varepsilon_{xz} = 0 \quad \text{Equation 3.10}$$

where  $a_0$  and  $a$  are the in-plane lattice constants of the substrate and epitaxial layer, respectively.

$C_{12}$  and  $C_{11}$  are elastic constants. For GeSn system, the relevant parameters were listed in Table A1 of Appendix A.

In strained semiconductors, the Luttinger-Kohn Hamiltonian ( $H_{L-K}$ ) for calculation of band structure evolves into the Pikus-Bir Hamiltonian ( $H_{P-B}$ )[93].

$$H_{P-B} = H_{L-K} - H_S \quad \text{Equation 3.11}$$

and

$$H_S = \begin{pmatrix} T_\varepsilon & 0 & 0 & 0 & 0 & 0 & 0 & 0 \\ 0 & T_\varepsilon & 0 & 0 & 0 & 0 & 0 & 0 \\ 0 & 0 & U_\varepsilon + Q_\varepsilon & 0 & 0 & 0 & 0 & 0 \\ 0 & 0 & 0 & U_\varepsilon - Q_\varepsilon & 0 & 0 & -\sqrt{2}Q_\varepsilon & 0 \\ 0 & 0 & 0 & 0 & U_\varepsilon - Q_\varepsilon & 0 & 0 & \sqrt{2}Q_\varepsilon \\ 0 & 0 & 0 & 0 & 0 & U_\varepsilon + Q_\varepsilon & 0 & 0 \\ 0 & 0 & 0 & -\sqrt{2}Q_\varepsilon & 0 & 0 & U_\varepsilon & 0 \\ 0 & 0 & 0 & 0 & \sqrt{2}Q_\varepsilon & 0 & 0 & U_\varepsilon \end{pmatrix} \quad \text{Equation 3.12}$$

where  $T_\varepsilon = a_c(\varepsilon_{xx} + \varepsilon_{yy} + \varepsilon_{zz})$ ,  $U_\varepsilon = -a_v(\varepsilon_{xx} + \varepsilon_{yy} + \varepsilon_{zz})$ ,  $Q_\varepsilon = -\frac{b}{2}(\varepsilon_{xx} + \varepsilon_{yy} - 2\varepsilon_{zz})$

At the position of  $k=0$ , the band edge energies could be obtained as

$$\begin{aligned} E_c(k=0) &= E_g + a_c(\varepsilon_{xx} + \varepsilon_{yy} + \varepsilon_{zz}) \\ E_{HH}(k=0) &= -P_\varepsilon - Q_\varepsilon = a_v(\varepsilon_{xx} + \varepsilon_{yy} + \varepsilon_{zz}) + \frac{b}{2}(\varepsilon_{xx} + \varepsilon_{yy} - 2\varepsilon_{zz}) \\ E_{LH}(k=0) &= -P_\varepsilon + Q_\varepsilon = a_v(\varepsilon_{xx} + \varepsilon_{yy} + \varepsilon_{zz}) - \frac{b}{2}(\varepsilon_{xx} + \varepsilon_{yy} - 2\varepsilon_{zz}) \end{aligned} \quad \text{Equation 3.13}$$

The splitting energy between the band edges of HH and LH at  $k=0$  is

$$E_{HH}(k=0) - E_{LH}(k=0) = b(\varepsilon_{xx} + \varepsilon_{yy} - 2\varepsilon_{zz}) \quad \text{Equation 3.14}$$

Therefore, the band gaps between CB and HH (LH) could be written as

$$\begin{aligned} E_{C-HH} &= E_g - \delta E_{hy} + \frac{1}{2}\delta E_{sh} \\ E_{C-LH} &= E_g - \delta E_{hy} - \frac{1}{2}\delta E_{sh} \end{aligned} \quad \text{Equation 3.15}$$

Where  $\delta E_{hy} = a(\varepsilon_{xx} + \varepsilon_{yy} + \varepsilon_{zz})$  and  $\frac{1}{2}\delta E_{sh} = Q_\varepsilon = -\frac{b}{2}(\varepsilon_{xx} + \varepsilon_{yy} - 2\varepsilon_{zz})$  are defined as hydrostatic

deformation and shear deformation energy, respectively.

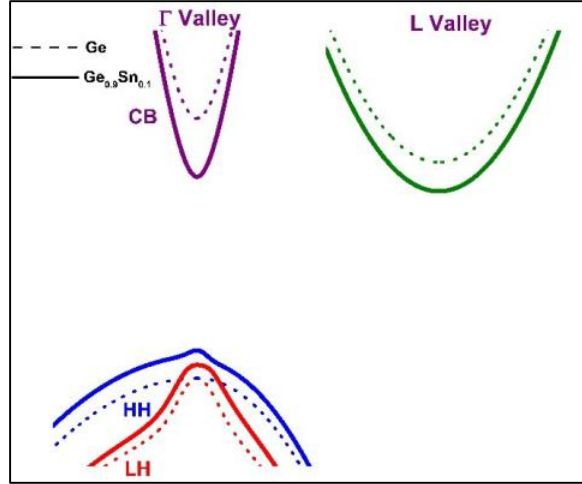


Figure 3.6 The band structure comparison of Ge bulk and compressive strained  $\text{Ge}_{0.9}\text{Sn}_{0.1}$  at room temperature.

Taking  $\text{Ge}_{0.9}\text{Sn}_{0.1}$  as an example, the change of band structure under compressive strain is compared with relaxed bulk Ge in Figure 3.6. The change of band edges of  $\text{Ge}_{0.9}\text{Sn}_{0.1}$  as a function of compressive strain was shown in Figure 3.7. The band structure of unstrained and strained  $\text{Ge}_{0.9}\text{Sn}_{0.1}$  at room temperature (300 K) was calculated for comparison, as shown in Figure 3.8. For unstrained  $\text{Ge}_{0.9}\text{Sn}_{0.1}$ , The HH and LH merge on top of valance band edge. The energy difference between direct ( $E_{\Gamma}$ ) and indirect bandgap ( $E_L$ ) is 7 meV, indicating that the  $\text{Ge}_{0.9}\text{Sn}_{0.1}$  is quasi-direct material. With the increase of compressive strain, both  $E_{\Gamma}$  and  $E_L$  increase rapidly while the  $E_{\Gamma}$  increases faster than  $E_L$ . As a result, the compressive strain increases the indirectness of  $\text{Ge}_{0.9}\text{Sn}_{0.1}$ . Meanwhile, the heavy hole ( $E_{hh}$ ) and light hole ( $E_{lh}$ ) split with each other. The  $E_{hh}$  moves up while  $E_{lh}$  moves down. The compressive strain also increases band edge energy of SO, which reduces the non-radiative Auger recombination and increase the quantum efficiency in the process of light emission. At the compressive strain of -0.5 %, the energy difference between  $E_{\Gamma}$  and  $E_L$  is 45 meV and the splitting energy between  $E_{hh}$  and  $E_{lh}$  is 45 meV. The energy of SO band increases from 0.341 to 0.352 eV under -0.5% compressive strain. The increase of SO band energy

dramatically reduces the Auger process, which is the predominant non-radiative mechanism especially for mid-infrared light emission.

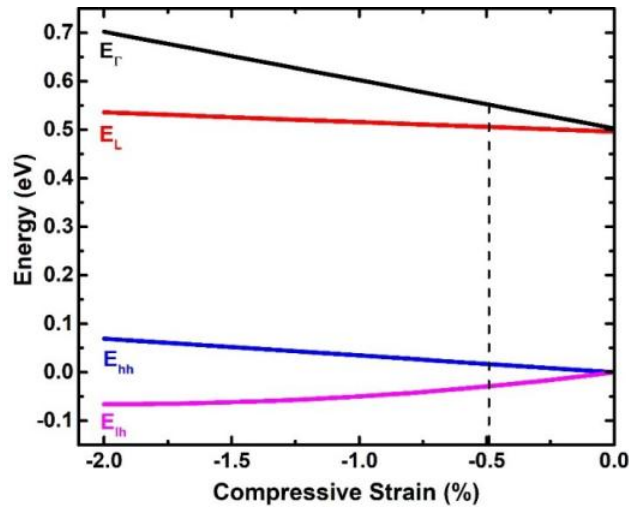


Figure 3.7 The energy change of  $\text{Ge}_{0.9}\text{Sn}_{0.1}$  band edge as a function of compressive strain.

The strain also has a strong effect on the effective masses of CB, HH, and LH. As a result, the density of states could be engineered by strain and thus the population of carriers is changed. The tuning of effective masses by strain also changes the mobility of carriers and transportation properties. For optoelectronic devices the compressive strain has been proven to reduce the lasing threshold density and high power output as a result of the reduced heavy-hole effective mass[101]. The strain could also alter the polarization of light emission for optoelectronic devices. For example, the optical transition between  $\Gamma$  valley and HH is mainly Transverse Electric (TE) polarized. In contrast, the optical transition between  $\Gamma$  valley and LH is predominately Transverse Magnetic (TM) polarized. The compressive strain lifts up heavy hole above light hole as the top of valance band. Under the compressive strain the light emission is mainly TE polarized.

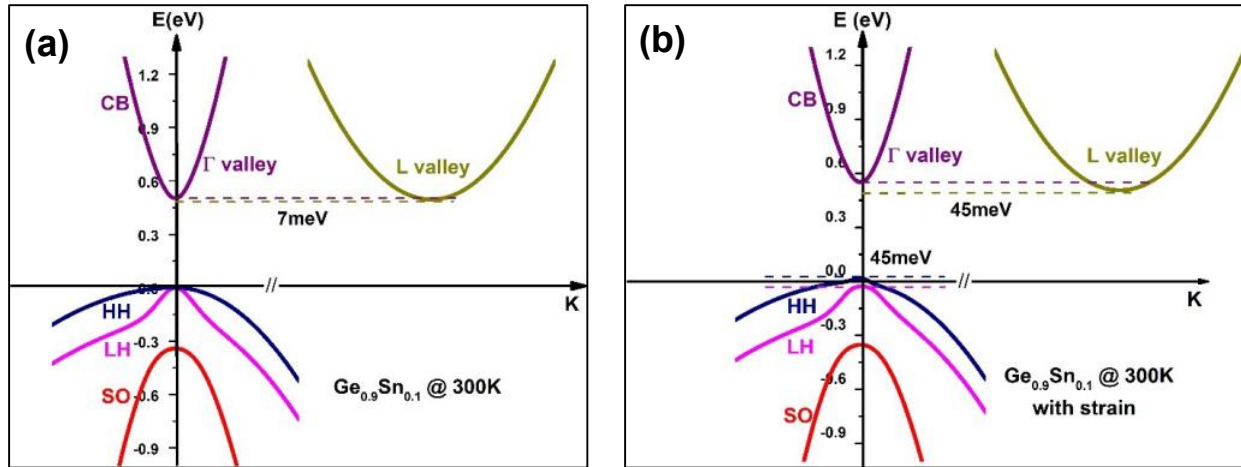


Figure 3.8 The comparison of band structure between (a) unstrained and (b) compressively strained  $\text{Ge}_{0.9}\text{Sn}_{0.1}$  at room temperature.

## Chapter 4. High Sn-content GeSn by RP-CVD

### 4.1. Reduced-pressure chemical vapor deposition (RP-CVD)

Our group has established an external cooperation with ASM America Inc. in Phoenix, AZ. GeSn was grown using an ASM Epsilon® 2000 Plus reactor which is a reduced-pressure chemical vapor deposition (RPCVD) single wafer epitaxial deposition system, as shown in Figure 4.1. The Epsilon is a horizontal flow, load-locked reactor, featuring a lamp heated silicon carbide coated graphite susceptor in a cold wall quartz chamber[42]. Prior to the GeSn growth, strain relaxed Ge buffer was grown on Si (100) substrate. Low/high temperature two step growth was adopted. In this process, the first step Ge buffer was grown at low temperature (320-370°C) condition to avoid 3-dimensional island growth while the second step Ge was grown at high temperature (600-650°C) to decrease the dislocations and increase the growth rate. After two step epitaxy, high temperature (800°C) in-situ cycle annealing was followed in order to further improve the quality of Ge buffer. The final thickness of Ge is 600-700 nm with threading dislocation densities of  $\sim 1 \times 10^7 \text{ cm}^{-2}$  which was measured by etch pit method. GeSn was grown in-situ on Ge buffer at the temperature below

450°C which is COMS-compatible. The commercially available precursors of GeH<sub>4</sub>, SnCl<sub>4</sub>, and carrier gases of H<sub>2</sub> or N<sub>2</sub> were utilized. The final thickness of GeSn layer is 800- 1200 nm.



Figure 4.1 The Epsilon® 2000 Plus RPCVD system from ASM company.

#### **4.2. Growth methodology of high Sn-content GeSn**

Historically it is generally acknowledged that the Sn incorporation via CVD epitaxy growth of GeSn is limited by chemical reaction dynamics. Therefore, substantial growth efforts were devoted to the process optimization of surface chemistry kinetics and thermodynamics[40][103][64]. However, recently we discovered a spontaneous-relaxation-enhanced (SRE) Sn incorporation mechanism for growth using GeH<sub>4</sub> and SnCl<sub>4</sub> as precursors[43][44]. It was found that Sn incorporation is primarily limited by compressive strain under Sn oversaturation condition while surface chemical reaction being secondary[104]. Since Sn exhibits lower free energy[4], the excess provided Sn atoms will float and segregate on the surface, or be desorbed from the surface. For example, when the nominal growth recipe was used with targeting Sn content of 12%, the Sn incorporation starts from 12% and then increases continuously to 15% due to the material gradual relaxation. More Sn incorporation also results in the reduction of surface Sn segregation. Since all the growth parameters maintained invariable, the gradient GeSn was grown spontaneously rather than intentionally. Guided by SRE discovery, new growth strategies were carefully designed which

lead to high quality and high Sn incorporation[43]. Other research groups also observed SRE mechanism in the study of GeSn epitaxy[39]. While this approach showed its effectiveness based on the previous work, the microscopic mechanism of GeSn strain relaxation induced high Sn incorporation as well as high quality material formation is still unclear. A thorough understanding of the mechanism would provide great insights to guide the future high quality and high Sn composition GeSn material growth for the development of high performance Si based optoelectronics.

In order to explore the high Sn incorporation by SRE mechanism, five GeSn samples were grown on relaxed Ge buffered Si substrate with GeH<sub>4</sub> and SnCl<sub>4</sub> precursors. Ge buffer layer with approximately 600 nm thickness was grown by low/high temperature two-step growth followed by post thermal annealing. The 1<sup>st</sup> 150 nm-thick layer was grown at temperature of 375°C while the 2<sup>nd</sup> 450 nm-thick layer was grown at temperature of 600 °C using 10% GeH<sub>4</sub> in purified H<sub>2</sub> carrier gas. Afterwards the in-situ annealing was done at >800 °C. GeSn growth was initiated on Ge buffer with the temperature between 200 and 400°C. SnCl<sub>4</sub> is a liquid at room temperature and must be delivered using a bubbler in which H<sub>2</sub> gas is metered to control the SnCl<sub>4</sub> mass flow rate. All the sample was grown with a SnCl<sub>4</sub>/(GeH<sub>4</sub>+SnCl<sub>4</sub>+H<sub>2</sub>) molar flow fraction of 10<sup>-5</sup> order of magnitude.

Two strategies have been used in GeSn epitaxy to obtain high Sn incorporation: i) the SRE approach for sample A, B and C with nominal growth recipe of 9%, 10% and 11% Sn and the corresponding finally achieved Sn compositions 12.5%, 12.9% and 15.9%, respectively; ii) The GeSn virtual substrate (VS) approach for sample D and E in which GeSn VS was prepared through SRE approach with a nominal growth recipe of 12% and achieved intermediate Sn composition of 16.5% for both samples. Sample D was then grown with single-step Sn enhanced recipe on GeSn



VS with the final achieved Sn composition 17.5%. Sample E was grown with a three-step gradient GeSn recipe with target thickness 100 nm for each step layer. For each step the grading rate of Sn incorporation was designed to be moderate in order to suppress the breakdown of continuous growth. The SnCl<sub>4</sub> flow fraction for each step epitaxy increases by ~8% compared with the previous step. The graded structure eases compressive strain gradually, leading to the continuous increase of Sn concentration. The final Sn content was obtained as 22.3%, an unprecedented achievement so far for CVD technology.

### 4.3. Sample characterization

Table 4.1 Summary of GeSn layer thicknesses, the maximum Sn compositions, average of Sn compositions, degree of compressive strains and degree of relaxations.

Sample	Structure	Thickness (nm)	The maximum Sn Composition (%) Region I / II	Average Sn Composition by XRD (%)	Strain/relaxation (%)
A	1 <sup>st</sup> layer	180	8.8 / 10.2	9.4	-0.04 / 96.5
	2 <sup>nd</sup> layer	660	12.5	11.4	-0.14 / 63.9
B	1 <sup>st</sup> layer	320	9.2 / 10.5	9.7	-0.24 / 80.2
	2 <sup>nd</sup> layer	500	12.9	12.1	-0.39 / 30.7
C	1 <sup>st</sup> layer	250	11.7 / 13.2	10.5	-0.01 / 92.4
	2 <sup>nd</sup> layer	670	15.9	14.4	-0.29 / 52.1
D	1 <sup>st</sup> layer	310	11.2 / 13.7	11.9	-0.04 / 94.7
	2 <sup>nd</sup> layer	550	16.5	15.5	-0.28 / 60.0
	3 <sup>rd</sup> layer	260	17.5	17.4	-0.38 / 3.8
E	1 <sup>st</sup> layer	380	11.9 / 15.5	12.3	-0.01 / 93.7
	2 <sup>nd</sup> layer	830	22.3	19.0	-0.61 / 2.8

The material characterizations were performed after the growth. SIMS results were used to determine the Sn compositions, which were cross checked by Energy-dispersive X-ray Spectroscopy (EDX) with good agreement. Strains and degree of relaxations were studied by data

fitting of reciprocal space mapping (RSM) of X-ray diffraction (XRD). Table 4.1 summarizes layer thicknesses, Sn compositions, compressive strains and degrees of relaxations for five samples.

#### 4.3.1. Transmission electron microscopy (TEM) and Secondary ion mass spectrometry (SIMS)

Typical dark field TEM images and Secondary Ion Mass Spectrometry (SIMS) of sample A, D, E are presented in Figure 4.2 (a), (c), and (e) and Figure 4.2 (b), (d), and (f), respectively. Samples B and C show similar results as sample A.

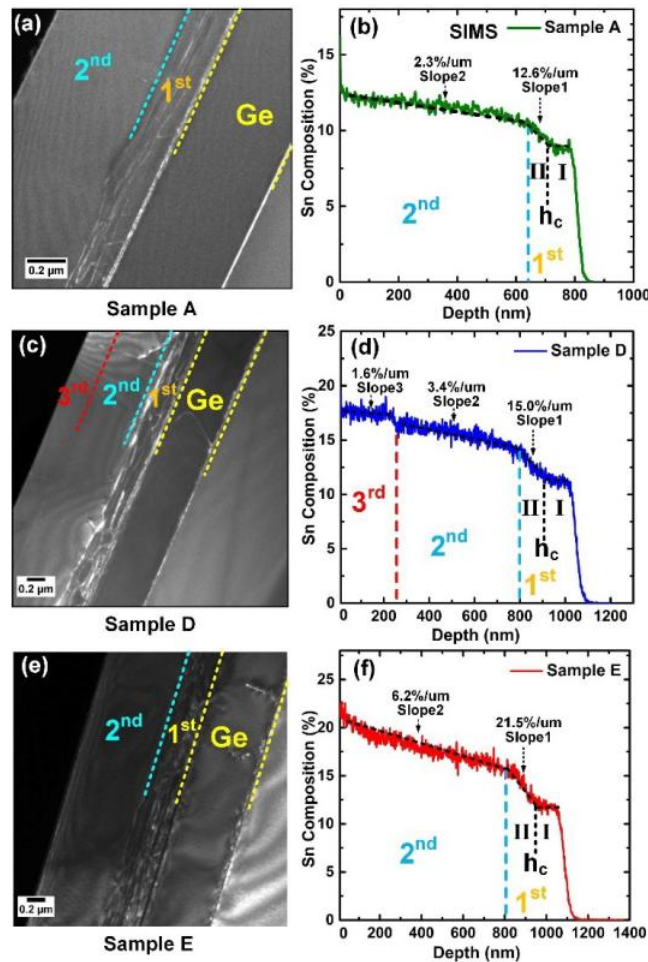


Figure 4.2 (a) Dark field TEM image of sample A. (b) SIMS of sample A. (c) TEM Image of sample D. (d) SIMS of sample D. (e) TEM image of sample E. (f) SIMS of sample E.

For sample A, two GeSn layers could be clearly resolved as shown in TEM images of Figure 4.2 (a): i) highly defective layer (1<sup>st</sup> layer) of 180 nm thickness on Ge buffer and ii) low defect layer (2<sup>nd</sup> layer) of 660 nm thickness above the 1<sup>st</sup> layer. Correspondingly, the two-layer structure observed from TEM image was also marked on the SIMS plot. From SIMS, both layers show Sn composition spontaneously enhanced gradient. The 1<sup>st</sup> layer could be further subdivided into two regions defined by the boundary of the critical thickness  $h_c$ , in which region-I and II represent constant low Sn content and Sn-enhanced gradient, respectively. Hereby the critical thickness  $h_c$  was calculated based on People – Bean (P-B) model[105]. The region I maintains with 8.8% Sn contents while the region II obtains the maximum 10.2% Sn contents with sharp Sn composition gradient. Through linear data fitting the gradient rate at region II of the 1<sup>st</sup> layer was obtained as 12.6%/μm, which is 5.5 times of 2.3%/μm in the 2<sup>nd</sup> layer. Note that since the 2<sup>nd</sup> layer was Sn gradient with a small gradient rate, part of the strain could be relaxed by the biaxial distortion of lattice constant without breaking the cubic crystal structure.

For Sample D, the GeSn VS exhibits a similar two-layer structure with the thickness of 310 nm and 550 nm for the 1<sup>st</sup> and 2<sup>nd</sup> layer, respectively. The additional 3<sup>rd</sup> layer was measured with a thickness of 260 nm, which is below the theoretical critical thickness of 1171 nm calculated by P-B model. Therefore, the 3<sup>rd</sup> layer of sample D could be considered as pseudomorphic growth which was further confirmed by RSM of XRD analysis. One bright line was observed to travel across the 2<sup>nd</sup> and 3<sup>rd</sup> layers, indicating the penetration of threading dislocation which is partly responsible for strain relaxation. From SIMS, the two-layer structure was marked and the 1<sup>st</sup> layer was divided into region-I and II, similar to sample A. Region I shows the constant Sn composition as 11.2% while region II reaches the final Sn composition of 13.7%. The gradient rate at region II of the 1<sup>st</sup> layer and the 2<sup>nd</sup> layer are 15%/μm and 3.4%/μm, respectively, which is higher than that of sample

A. At the 3<sup>rd</sup> layer the Sn composition was slightly enhanced with gradient rate of 1.6%/μm. Eventually 17.5% Sn incorporation was achieved on top of the 3<sup>rd</sup> layer.

For sample E, the GeSn VS shows a similar two-layer structure with sample D. The 1<sup>st</sup> defective layer was observed with thickness of 380 nm and the 2<sup>nd</sup> layer of 830 nm thickness is low defect without distinct boundaries between the steps, suggesting the smooth growth transition. From SIMS, the two-layer structure and region-I and II in the 1<sup>st</sup> layer were marked. The Sn content at region I is 11.9% and the final Sn content at region II is 15.5%. The gradient rate at region II and the 2<sup>nd</sup> layer is 21.5%/μm and 6.2%/μm, both of which are higher than sample A and sample D. Sample E achieved the final world-record Sn composition of 22.3% after three-step gradient growth. It is noteworthy that based on the sharp gradient rate at the end of 2<sup>nd</sup> layer, higher Sn incorporation than the value of 22.3% is expected if sample E could be grown thicker with the same recipe. High Sn content of sample E increases light emission efficiency due to more directness of bandgap and extends operating wavelength up to 3220 nm, evidenced by PL spectra.

#### 4.3.2. Photoluminescence (PL) characterization

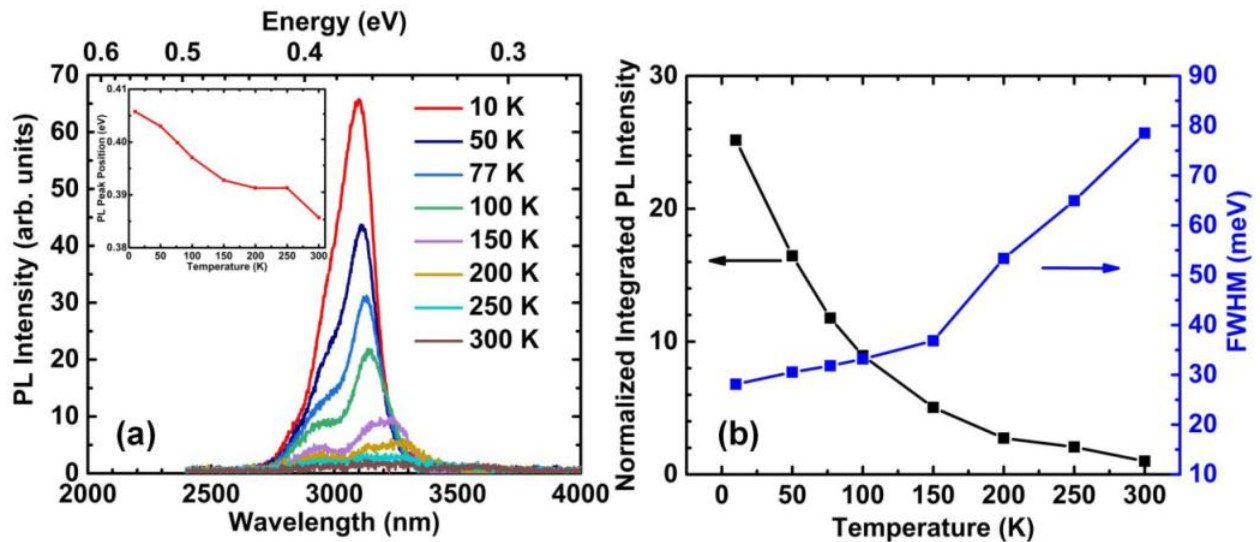


Figure 4.3 (a) Temperature-dependent photoluminescence (PL) of sample E from 10 to 300 K. The insert: temperature-dependent peak shift. (b) The integrated PL intensity and The full width of half maximum (FWHM).

The temperature-dependent photoluminescence (PL) of sample E was plotted in Figure 4.3 (a), with temperature ranging from 10 to 300 K. A continuous wave (CW) laser emitting at 532 nm wavelength was used as optical-pumping source. The pumping power was measured as 50 mW and the beam size was 100  $\mu\text{m}$  in diameter. PL emission was spectrally analyzed by the combination of iHR320 spectroscopy and liquid nitrogen cooled Indium Antimonide (InSb) detector with the wavelength detection cut-off at 5  $\mu\text{m}$ . A SR830 DSP lock-in system along with a chopper was applied to amplify the PL signal. Samples were mounted in a helium-cooled cryostat with temperature ranging from 10 to 300 K. For sample E, PL spectra exhibit a clear blue shift with decreasing temperature, shown in the insert of Figure 4.3 (a). The shift follows classical Varshni empirical model which describes the temperature dependence of bandgap energy of semiconductors. The wavelength is extended up to 3220 nm at 300 K. As shown in Figure 4.3 (b), the integrated PL intensity increases 25 times as temperature decreases from 300 to 10 K, featuring the true direct bandgap material characteristics. Meanwhile, the FWHM decreases at lower temperature. The slight absorption from the ambient environment was observed at  $\sim 3000$  nm wavelength on the spectra.

#### 4.3.3. Energy Dispersive X-ray Spectroscopy (EDX)

The EDX technique is a powerful tool to determine the local elemental information of semiconductor materials. In TEM facility, a focused beam of high energy electrons is used to bombard the sample and excited the electrons from the inner orbitals to the higher energy level, leaving the vacancies at the inner orbitals. When the electrons transit from high energy level to the inner orbitals, the excessive energy is released as the emission of X-ray. Through the analysis of “characteristic” X-ray, the constituent of elements in the TEM samples could be qualitatively

identified. For most of the elements the analytical accuracy is  $\pm 2\%$ . Since the TEM sample is normally less than 100 nm, the spatial resolution could be achieved as high as 10 nm.

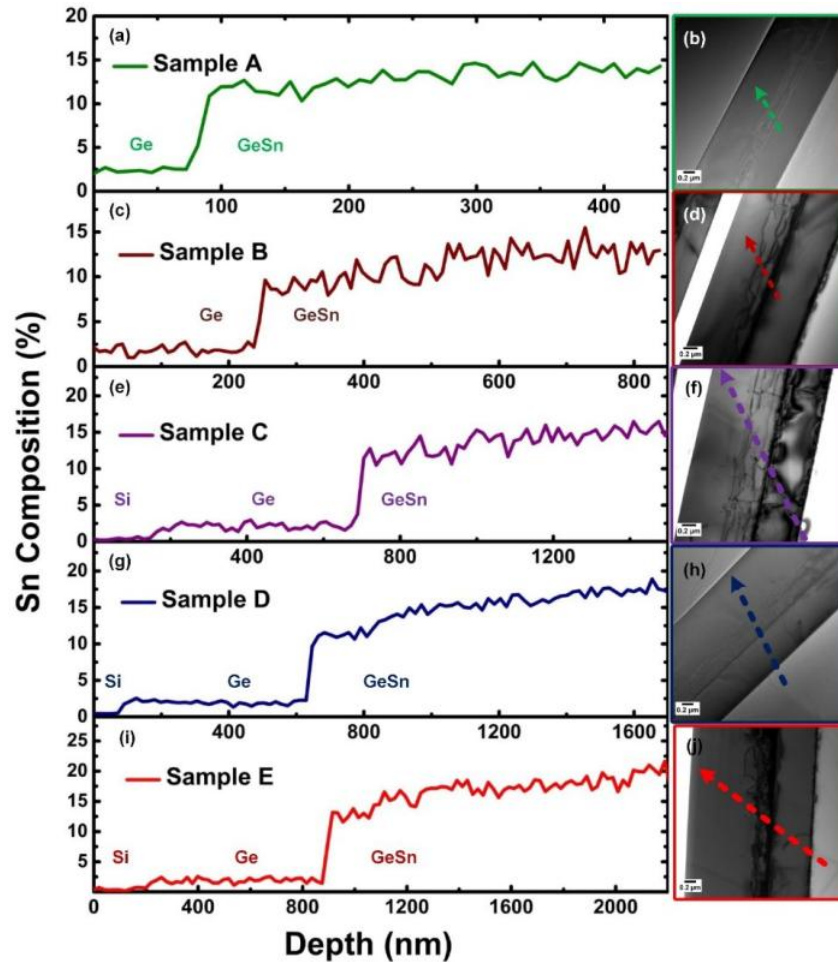


Figure 4.4 EDX-STEM results show Sn composition curves (a), (c), (e), (g), and (i) as function of scanning depth for samples A, B, C, D, and E, respectively. Bright fields of cross sectional TEM images of sample A, B, C, D, and E are shown in (b), (d), (f), (h), and (j), respectively.

The EDX-STEM results for all the five GeSn samples of A, B, C, D, and E were shown in Figure 4.4 (a), (c), (e), (g), and (i), respectively. The two-layer structures of GeSn were shown on EDX line scans of all the samples, which is highly consistent with the SIMS results. The gradient GeSn was also confirmed by EDX results. The sharp interfaces between Ge and GeSn were observed from EDX line scans. The bright field TEM images viewed from  $[\bar{1}10]$  direction for all the five samples of A, B, C, D, and E were shown in Figure 4.4 (b), (d), (f), (h), and (j), respectively. For

each GeSn layer the highly defective layer at the bottom and low defect layer on the top were clearly shown. It should be noticed that the scanning paths of EDX are not parallel to growth direction in order to obtain accurate Sn composition as much as possible.

The symmetric XRD  $2\theta$ - $\omega$  scans along (004) plane of sample A, D, and E were plotted in Figure 4.5 (a), (c), and (e), respectively. The corresponding RSM color contours at the asymmetric (224) scan were drawn in Figure 4.5 (b), (d), and (f) for sample A, D, and E, respectively. Two-layer structure was observed for sample A while three-layer characteristic was shown in sample D. For sample E, the three-step Sn compositional graded structure was not resolved. The layer structure information from XRD shows high consistency with TEM and SIMS results. The least square fitting was performed to determine the average Sn compositions and strains for each layer. Vegard's law was employed to calculate the relaxed lattice constant of GeSn:  $a_{GeSn} = (1 - x)a_{Ge} + xa_{Sn} + bx(1 - x)$ , where  $a_{GeSn}$ ,  $a_{Ge}$ , and  $a_{Sn}$  are lattice constants of GeSn, Ge and Sn, respectively,  $x$  is Sn composition and  $b$  is bowing parameter, which has been reported by various literatures[106][51][107][108]. In this work, the bowing parameter  $b = -0.066 \text{ \AA}$  was adopted[108], which has been proven to best fit our experimental result. It should be noted that the Ge buffer layer undergoes tensile strain up to 0.25%, which is due to the discrepancy of thermal expansion coefficients between Si and Ge. After cooling down from thermal annealing ( $T=800^\circ\text{C}$ ), residual tensile strain remains in Ge buffer layer.

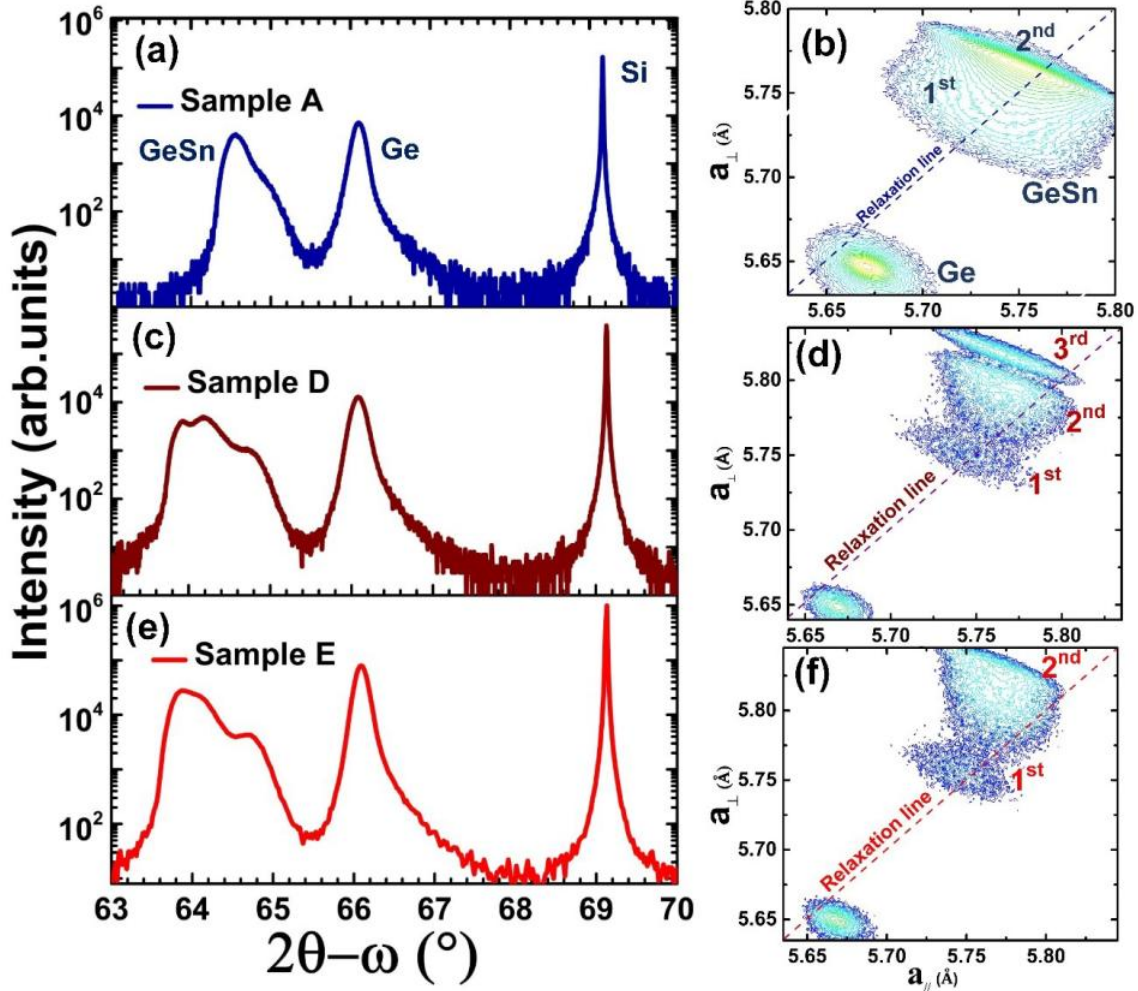


Figure 4.5 The symmetric  $2\theta-\omega$  scans (a), (c), and (e) along (004) plane for sample A, D, and E, respectively. RSMs of XRD (b), (d), and (f) at the asymmetric (224) for sample A, D, and E, respectively.

## Chapter 5. Strain relaxation analysis

While spontaneous-relaxation-enhanced (SRE) mechanism showed its effectiveness based on the previous work, the microscopic mechanism of GeSn strain relaxation induced high Sn incorporation as well as high quality material formation is still unclear. A thorough understanding of the mechanism would provide great insights to guide the future high quality and high Sn composition GeSn material growth for the development of high performance Si based optoelectronics. In this chapter, we systemically studied the strain relaxation of two different



regions: 1) GeSn/Ge interface and 2) beyond the critical thickness. It is revealed that the generation of dislocations at GeSn/Ge interface accommodates the large lattice mismatch and favors the crystalline nucleation for initial GeSn growth. A self-organized dislocation network is formed within the first 200-300 nm GeSn layer near the GeSn/Ge interface, which blocks the propagation of dislocation, leaving the subsequent GeSn layer low defect.

### 5.1. Critical thickness analysis

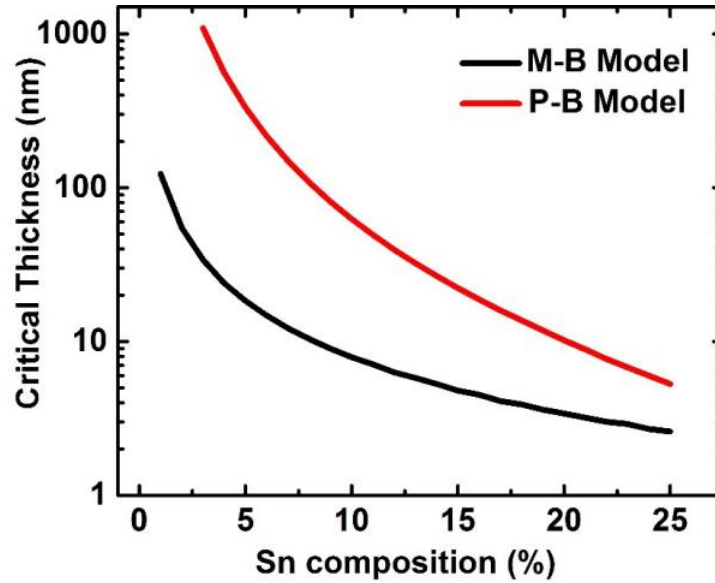


Figure 5.1 Critical thicknesses calculation for GeSn on Ge buffer based on Matthews and Blakeslee (M-B) model and People and Bean (P-B) model.

The critical thickness  $h_c$  of GeSn alloy on Ge was calculated using both Matthews and Blakeslee (M- B) model and People and Bean (P- B) model, as shown in Figure 5.1.

The critical thickness based on M- B model is written as[109],

$$h_c^{M-B} = \frac{1}{8\pi f} \frac{b}{\cos\lambda} \left[ \frac{1 - \nu \cos^2\beta}{(1 + \nu) \cos\lambda} \right] \left[ \ln \frac{h_c^{M-B}}{b} + 1 \right] \quad \text{Equation 5.1}$$

where  $b$  is the burger vector,  $f$  is the strain value,  $\nu$  is poisson's ratio,  $\beta$  is the angle between slip plane and the direction perpendicular to intersection line of interface and slip plane and  $\lambda$  is the angle between burger vector  $b$  and dislocation line. For GeSn/Ge system,  $b$  is the burger vector of

60° mixed dislocation since it dominates in GeSn epitaxy. So  $\cos\beta = \cos\lambda = 0.5$ . The value of strain  $f$  could be estimated as  $\frac{a_{GeSn} - a_{Ge}}{a_{GeSn}}$ , where  $a_{GeSn}, a_{Ge}$  are lattice constants of GeSn and Ge, respectively. Poission ratio  $\nu$  could be obtained by linear interpolation between Ge and  $\alpha$ -Sn. The necessary parameters could be found in Appendix A. Matthews and Blakeslee (M- B) model is also called mechanical equilibrium model. It describes that misfit stress drives the preexisting threading dislocations to elongate and form MDs segments[109]. However, this model is not sufficient to describe the epitaxy that has low interfacial MDs.

People and Bean (P- B) model is based on the energy balance of non-equilibrium theory where the areal strain energy density is balanced against self-energy of an isolated dislocation[105]. The film was grown initially free of MDs until the accumulated elastic strain energy exceeds activation energy of MDs. Thereafter, the dislocations nucleate at the critical thickness  $h_c$  from the interface.

Based on P- B model, the critical thickness could be revised as[105]

$$h_c^{P-B} = \frac{1}{16\sqrt{2}\pi} \frac{b^2}{af^2} \frac{1-\nu}{1+\nu} \ln \frac{h_c^{P-B}}{b} \quad \text{Equation 5.2}$$

The experimental critical thickness of GeSn grown on Ge follow the similar trend, but higher than the predication using P- B model, which assumes that the initial grown film is free of MDs. However, based on our analysis of dislocation configuration at GeSn/Ge interface, strain energy is partially relaxed at the initial growth since MDs already generate at the interface. Therefore, the actual critical thickness remains larger than theoretical predication of P- B model.

## 5.2. Calculations of elastic energy, effective stress, strain, and relaxation

The strain in the film could be expressed as[110]

$$f_1 = \frac{a_{GeSn} - a_{Ge}}{a_{GeSn}} \quad (h \leq h_c) \quad \text{Equation 5.3}$$

$$f_2 = \frac{1}{8\pi} \frac{(1 - \nu \cos^2 \lambda) b^2}{(1 + \nu) b_{\parallel}} \frac{1}{h} \ln\left(\frac{4R}{b}\right) = \frac{A}{h} \quad (h > h_c) \quad \text{Equation 5.4}$$

where  $R$  is the external cut off radius of dislocation loop,  $b_{\parallel}$  is the edge component of burger vector parallel to the interface. Using boundary condition at critical thickness  $h_c$ , the constant of  $A$  could be determined as:  $A = f_1 * h_c$ . The parameters used in the calculation were given in Appendix A using linear interpolation method. Figure 5.2 (a) shows the effective stress and elastic energy of sample A as a function of thickness. Below critical thickness, effective stress linearly increases with thickness. Meanwhile, elastic strain energy accumulates. Beyond the critical thickness both effective stress and elastic energy drop rapidly, inversely proportional to the thickness because of the formation of large amounts of MDs. Both strain energy and effective stress reach the maximum at the point of critical thickness  $h_c$ .

The expression of degree of relaxation is  $R = \frac{a_{\parallel} - a_{Ge}}{a_{GeSn} - a_{Ge}}$ .  $R$  could also be expressed by strain  $f$ ,

which is written as

$$R = \frac{a_{GeSn}(1 - |f|) - a_{Ge}}{a_{GeSn} - a_{Ge}} \quad \text{Equation 5.5}$$

The effective shear stress is given as[55]

$$\tau_{eff} = u \cos \beta \frac{1 - \nu}{1 + \nu} f - \frac{u \cos \beta}{8\pi} b \cos \lambda \frac{1 - \nu \cos^2 \beta}{1 - \nu} \ln \frac{4h}{b} \quad \text{Equation 5.6}$$

The elastic strain energy is calculated as[111]

$$E_{elastic} = 2\mu \frac{1 + \nu}{1 - \nu} f^2 t \quad \text{Equation 5.7}$$

where  $t$  is the film thickness and  $\mu$  is the shear modulus. As shown in Figure 5.2 (b), below critical thickness the strain remains constant and beyond that strain is reversely proportional to the thickness because of the generation of dislocation network. The value of strain becomes steady gradually with continuous growth.

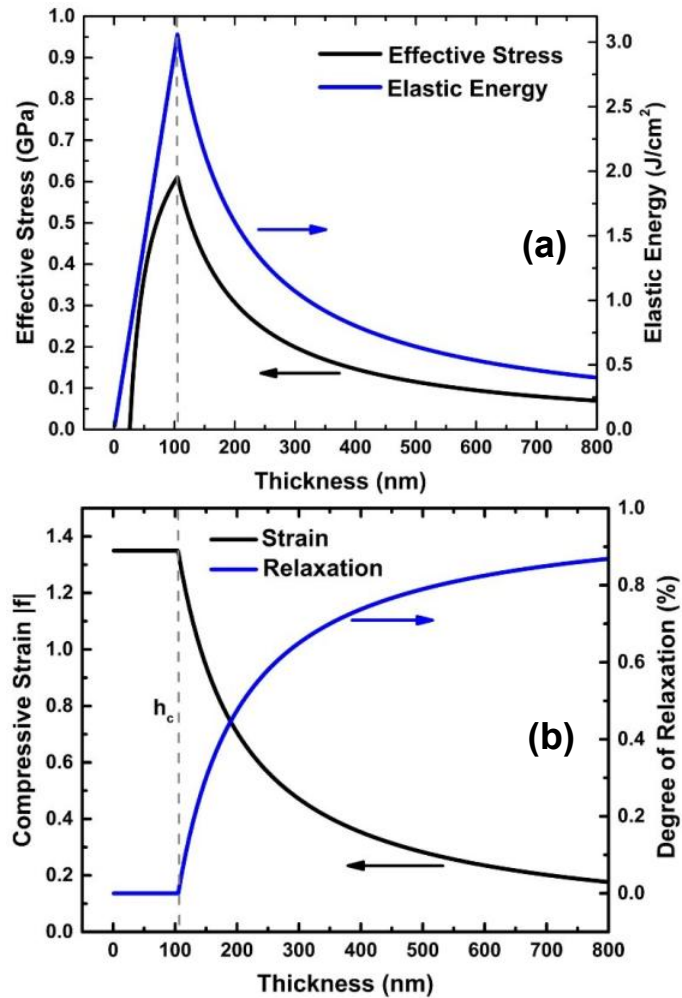


Figure 5.2 (a) Elastic energy and effective stress of Sample A were plotted as a function of thickness. (b) Strain and relaxation as a function of thickness were drawn.

### 5.3. Dislocation configuration at GeSn/Ge interface

The current study of dislocation configuration at GeSn/Ge interface is preliminary while the relaxation process at the interface for other group IV epitaxy such as Ge or SiGe on Si has been extensively studied. In this section, the GeSn/Ge interface was investigated by using the high resolution TEM (HRTEM) technique to probe the dislocation configuration, which could microscopically reveal the accommodation mechanism of large lattice mismatch at the interface for the initial GeSn nucleation. Through the analysis of atomic level TEM at the interface, it was

found that perfect  $90^\circ$  pure edge (Lomer) and  $60^\circ$  mixed dislocations are formed and the  $60^\circ$  mixed dislocations are dominant over Lomer dislocations at the interface. Intrinsic stacking faults were also observed, which are associated with two different reactions of dislocations:  $60^\circ$  dislocation dissociation and Lomer dislocation formation. By introducing dislocations, the compressive strain near the interface is partially relaxed, favoring the initial crystalline nucleation of GeSn on Ge buffer.

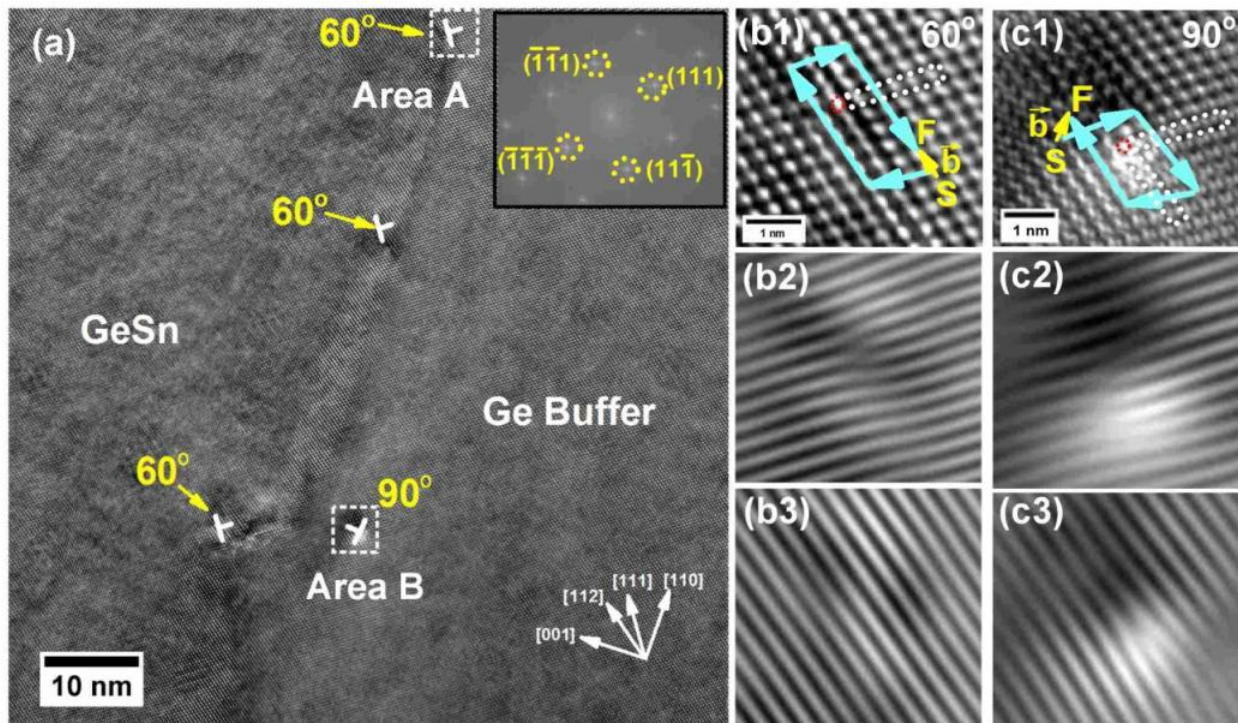


Figure 5.3 (a) The HRTEM image at the GeSn/Ge interface of sample B. (b1) Zoomed-in image of area A. (b2), (b3) The inverse FFT images. (c1) Zoomed-in image of area B. (c2), (c3) The Inverse FFT images.

The dislocation generation at the GeSn/Ge interface was studied for each sample with sample B as a typical example presented in this paper. Both Lomer and  $60^\circ$  mixed dislocations are formed near the interface, as shown in bright field HRTEM image viewed from  $[\bar{1}10]$  direction in Figure 5.3 (a). The observation of existence of Lomer dislocation was highly consistent with other studies, even though different CVD reactor and precursors were utilized. From the image, it is clear that

the 60° dislocations outnumbered the Lomer dislocations, which indicates that the 60° dislocations are dominant for the low-temperature (<400°C) GeSn epitaxy on Ge. This is because the activation energy of 60° dislocations is lower than that of Lomer dislocations since the gliding will proceed through the switching inter-atomic bonds instead of the diffusion motion of individual atoms[112]. The inset shows fast Fourier transform (FFT) pattern with different planes marked. In order to verify 60° dislocation, magnified high resolution TEM images of area A is shown in Figure 5.3 (b1), exhibiting the typical core structure of 60° dislocation. Its burger vector is identified as  $\frac{a}{4}[112]$  by drawing the burger circuit encircling the dislocation core. It is equal to the projected component of burger vector  $\frac{a}{2}[10\bar{1}]$  of 60° dislocation in the projection of  $(\bar{1}10)$  plane. The corresponding inverse FFT images are obtained by masking  $\{(111)(\bar{1}\bar{1}\bar{1})\}$  and  $\{(11\bar{1})(\bar{1}\bar{1}1)\}$  planes in FFT patterns, as shown in Figure 5.3 (b2) and (b3), respectively. The extra half plane of 60° dislocation was observed to be located at (111) plane. The magnified high resolution TEM image of area B presents core structure of Lomer edge dislocation, as shown in Figure 5.3 (c1). The corresponding burger vector of  $\frac{a}{2}[110]$ , which is obtained by drawing burger circuit, lies in (001) plane. Since {001} planes are not the gliding planes, Lomer dislocation is hardly mobile. Inverse FFT images of Lomer dislocation are shown in Figure 5.3 (c2) and (c3), by masking  $\{(111)(\bar{1}\bar{1}\bar{1})\}$  and  $\{(11\bar{1})(\bar{1}\bar{1}1)\}$  planes in FFT pattern, respectively. Two extra half planes were observed at different {111} planes. The Lomer dislocation could be treated as the reaction of two 60° dislocations from different {111} planes:  $\frac{a}{2}[10\bar{1}] + \frac{a}{2}[011] = \frac{a}{2}[110]$  .[113] It is an energetically favorable process according to Frank's  $b^2$  criteria:  $\frac{a^2}{2} + \frac{a^2}{2} > \frac{a^2}{2}$ . Lomer edge dislocation is twice effective for strain relaxation in comparison with that of the 60° mixed type because the efficiency of relaxation scales with the length of edge component of burger vector



projected into the interface[112]. However, due to high nucleation energy, the onset of Lomer dislocation is kinetically limited for GeSn epitaxy at low temperature growth.

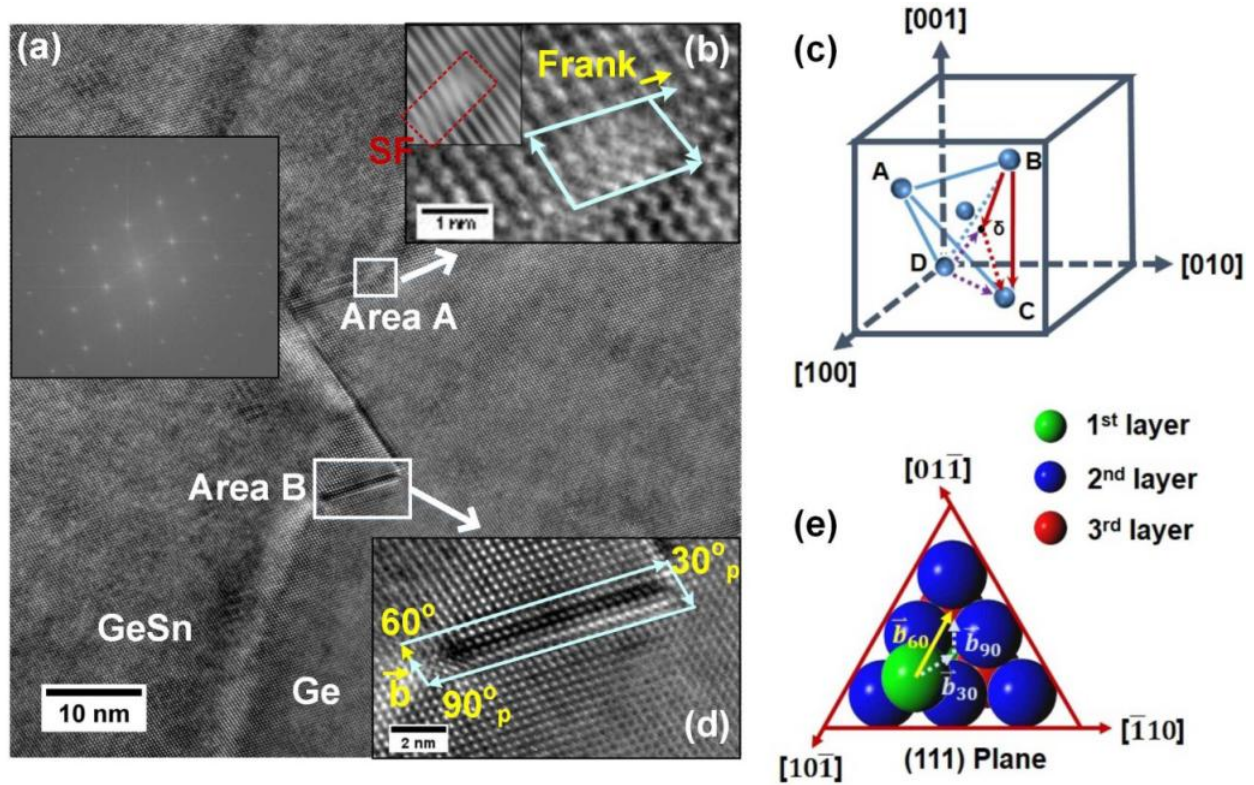
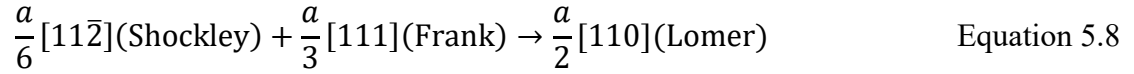


Figure 5.4 (a) Zigzagged intrinsic stacking faults at the GeSn/Ge interface of sample B. (b) Zoomed-in TEM image of area A. The insert is inverse FFT images. (c) Thompsons tetrahedron diagram. (d) In zoomed-in image of area B. (e) The glide motion of top atoms.

The zigzagged intrinsic stacking faults were also observed at the GeSn/Ge interface of sample B as shown in Figure 5.4 (a). The stacking faults start from the GeSn/Ge interface, and then wander through both Ge and GeSn along {111} planes, and end at the GeSn/Ge interface. The stretching angle between two stacking faults is  $54.7^\circ$ . The inset shows the corresponding FFT pattern, in which the streaks along [111] direction indicate the formation of stacking faults. In order to investigate the formation mechanism of stacking faults, two areas were specifically studied, as annotated as area A and area B in Figure 5.4 (a). Magnified image of area A shown in Figure 5.4 (b) indicates the presence of Frank partial dislocation at the interface, verified by drawing burger

circuit. The stacking fault associated with Frank partial dislocation was also observed at GeSn alloy in the inserted inverse FFT images of Figure 5.4 (b), which was obtained by masking  $\{(11\bar{1})(\bar{1}\bar{1}1)\}$  planes in FFT pattern. As stacking fault extends into GeSn, a  $90^\circ$  Shockley partial dislocation with burger vector  $\frac{a}{6}[11\bar{2}]$  is formed at the edge of stacking fault. Shockley partial dislocation glides to the interface and reacts with Frank partial dislocation to form a perfect Lomer dislocation. Therefore, stacking fault is terminated after this reaction[114]. The reaction is given as:



On the Thompsons tetrahedron diagram, shown as Figure 5.4 (c), it is marked as,



It should be noted that during the reaction no energy reduction occurs before and after this reaction according to Frank's criteria:  $\frac{a^2}{6} + \frac{a^2}{3} = \frac{a^2}{2}$ . However, there is a significant energy reduction when stacking fault is terminated during the reaction. Therefore, the overall energy of Frank, Shockley partials and stacking faults is greater than the energy of perfect Lomer dislocation, indicating that this process is energetically favorable.

Another mechanism of stacking fault associated with  $60^\circ$  dislocation dissociation was studied as well. The magnified image of area B shown in Figure 5.4 (d) presents the stacking fault extending into Ge buffer along (111) plane with the length of 9 nm. Using burger circuit enclosing the stacking faults, the projected burger vector  $\frac{a}{4}[112]$  is determined on the  $(\bar{1}\bar{1}0)$  plane, referring to  $60^\circ$  mixed dislocation. It indicates that the  $60^\circ$  dislocation dissociates into a pair of glissile  $30^\circ$  and  $90^\circ$  Shockley partial dislocations bound by stacking fault[115]. The reaction could be written as,



$$\frac{a}{2}[101](60^\circ) \rightarrow \frac{a}{6}[2\bar{1}1](30^\circ) + \frac{a}{6}[112](90^\circ) \quad \text{Equation 5.10}$$

$$\text{Or } BC(60^\circ) \rightarrow B\delta(30^\circ) + \delta C(90^\circ) \quad \text{Equation 5.11}$$

on the Thompsons tetrahedron diagram of Figure 5.4 (c).

The total energy after the dissociation is one third lower than that of 60° dislocation, comparing the energy states of pre- and post- reaction. For the dissociation of 60° dislocation, the glide motion of top atoms in (111) plane was illustrated in Figure 5.4 (e) with burger vector  $\vec{b}$  marked. Since the glide of 60° dislocation experiences higher energy barrier than 30° or 90° partial dislocations, it will decompose into the glide of 30° and 90° partial dislocation with the following sequence. The 30° partial dislocation glide takes the lead and 90° partial dislocation closely follows in order to maintain the close packing structure[116].

#### 5.4. Self-organized dislocation network

After the initial nucleation of dislocations at GeSn/Ge interface, the subsequent growth is pseudomorphic within critical thickness. Meanwhile, elastic strain energy accumulates with increasing thickness which impedes the Sn incorporation. Beyond the critical thickness, pseudomorphic epitaxy collapses and dislocations are generated to release the strain energy. As a result, more Sn atoms are incorporated into lattice sites. After the generation of dislocations, a self-organized dislocation network is formed as the result of dislocation propagations and reactions. The typical dark field TEM image of sample B, as shown in Figure 5.5 (a), confirms the formation of self-organized dislocation network, which was marked as the 1<sup>st</sup> layer. The 2<sup>nd</sup> layer is low-defect, suggesting that the majority of dislocations are localized in the 1<sup>st</sup> layer.

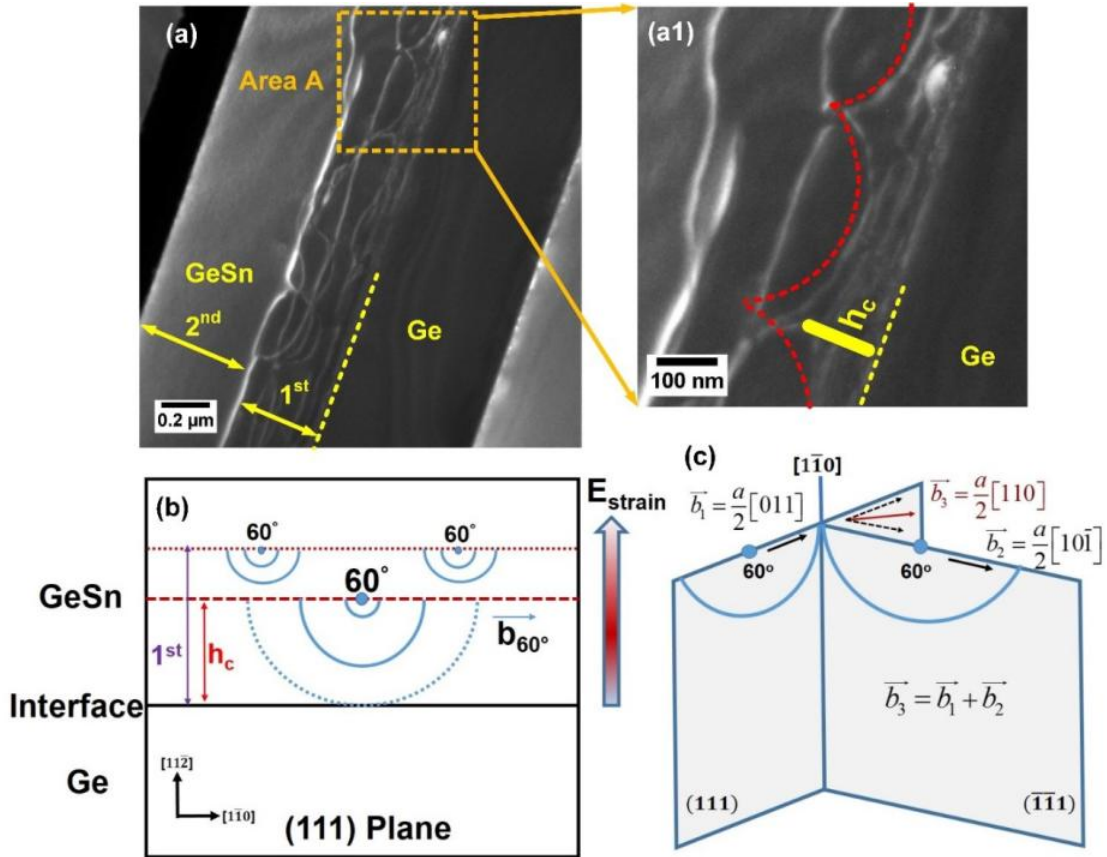


Figure 5.5 (a) Dark field TEM images of sample B. (a1) Zoom-in TEM image of area A. (b) The schematic diagram of half loop nucleation. (c) The formation of Lomer dislocation.

The formation mechanism of dislocation network could be explained by the following process: i) half-loop nucleation of 60° dislocation, ii) half loop propagation and iii) formation of Lomer dislocation. Magnified TEM image of area A shown in Figure 5.5 (a1) exhibits the nucleation of half loops, which is attributed to the generation of 60° dislocation[117]. The schematic diagram of half-loop nucleation of 60° dislocation was drawn in Figure 5.5 (b). In the diagram, the 60° mixed dislocations are dominantly nucleated on the epitaxial surface at critical thickness due to its low activation energy. Afterwards, the 60° dislocations will elongate along {111} planes as semicircular half loops[117][118]. Normally the half loops increase the radius continuously due to the strain field, which would eventually reach the GeSn/Ge interface and then form the linear misfit segments at the interface and two arms travelling upwards as threading dislocations[117].

However, another mechanism occurs before the half loops arrive at the interface: When two 60° dislocations glide along different {111} planes and meet with each other, they will intersect by cross-slipping mechanism in which one of the 60° dislocations climbs to another plane[118]. If two 60° dislocations have appropriate burger vectors, they will react and form Lomer dislocation. The threading components of two 60° mixed dislocations annihilate after the reaction without having to travel through the film. This process facilitates strain relaxation since Lomer dislocation is more efficient of relieving strain energy.

The total eight equivalent reactions on the pair of {111} planes have been studied and summarized in Ref.[119]. One typical reaction was schematically drawn in Figure 5.5 (c). One 60° dislocation on the (111) planes with  $\vec{b}_1 = \frac{a}{2}[011]$  reacts with another 60° dislocation on ( $\bar{1}\bar{1}1$ ) plane with  $\vec{b}_2 = \frac{a}{2}[10\bar{1}]$ , resulting in the formation of Lomer dislocation on (001) plane with  $\vec{b}_3 = \frac{a}{2}[110]$ . It could be expressed as,

$$\frac{a}{2}[011] + \frac{a}{2}[10\bar{1}] = \frac{a}{2}[110] \quad \text{Equation 5.12}$$

Similar process will repeat with the continuous growth to gradually relieve the residual strain energy. After the formation of Lomer dislocation, a self-assembled dislocation network is formed within the 1<sup>st</sup> GeSn layer, efficiently accommodating the lattice mismatch between GeSn and Ge. Therefore, the 1<sup>st</sup> GeSn layer could act as a sacrificial layer with large amount of dislocations, leaving low-defect GeSn in the 2<sup>nd</sup> layer.

## 5.5. Plan-view transmission electron microscopy (TEM) analysis

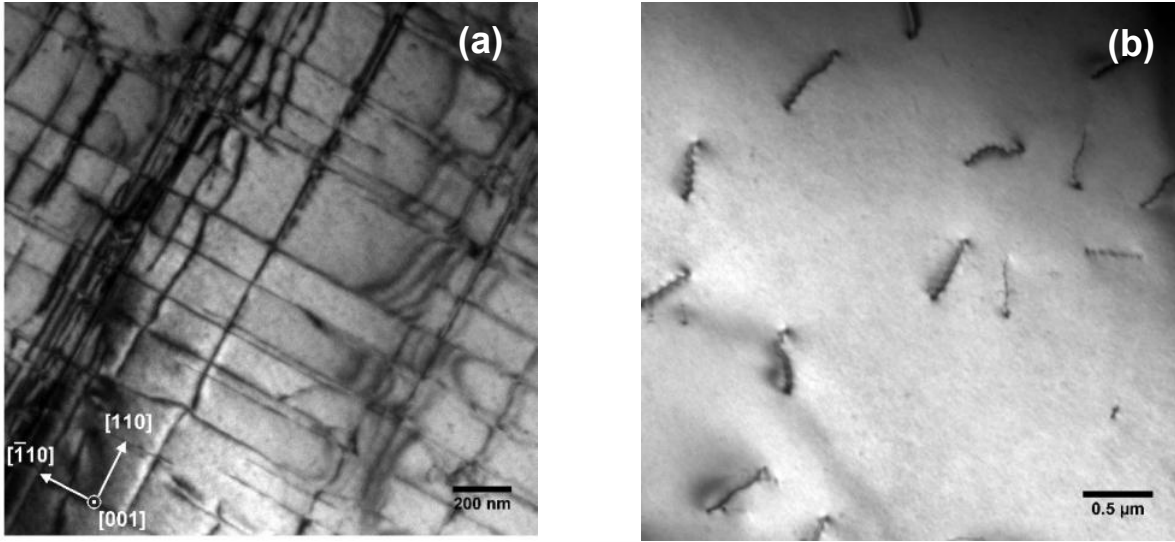


Figure 5.6 (a) Bright field plan-view TEM image of GeSn/Ge interface. (b) Plan view TEM image of the top GeSn layer.

The typical bright field plan-view TEM images of GeSn sample B was shown in Figure 5.6. At the interface of GeSn/Ge interface, a well-ordered dislocation network aligned along the two orthogonal [110] orientation at (001) was clearly observed, which originates from the propagation of 60° mixed dislocations. The results are highly consistent with cross-sectional TEM analysis. Assuming the TEM sample is 100 nm, the threading dislocations could be estimated. The width of plan view imaging shown in Figure 5.6 (a) is 1.9 μm. The number of threading dislocations are counted as 33 under the area of 1.9 μm\*100 nm. The dislocation density could be calculated as  $1.7 \times 10^{10} \text{ cm}^{-2}$ . The plan view TEM image on top of GeSn layer was shown in Figure 5.6 (b). The threading dislocations were explicitly observed as the line segments on the GeSn surface. By counting the number of line segments, the threading dislocation density on top of GeSn layer was estimated as  $9.7 \times 10^7 \text{ cm}^{-2}$ . By comparing the misfit dislocations of between GeSn/Ge interface and at the top of GeSn layer, the dislocation density on top of GeSn layer is two orders of magnitudes lower than that at the GeSn/Ge interface, which agrees well with the cross sectional TEM imaging.

## Chapter 6. Gibbs free energy calculation

In order to in-depth investigate the strain effect on Sn incorporation, especially during the 1<sup>st</sup> GeSn layer growth, the Gibbs free energy was calculated in both completely relaxed and compressively strained systems for comparison. Gibbs free energy was proven to provide good approximation of thermal stability of alloys under equilibrium condition. The minimization of free energy is the thermodynamic driving force of the stable crystallization. The calculation of Gibbs free energy has been used to study the thermal stability of GeSn and SiGeSn alloys[103][120]. In this work, the elastic strain energy was introduced into Gibbs free energy to estimate thermodynamic properties of compressively strained GeSn alloy. It is revealed that although metastable GeSn alloy was grown under nonequilibrium condition, our calculation of Gibbs free energy provides good description of strain effects on Sn incorporation with good agreement of experimental results.

### 6.1. Gibbs free energy calculation

The calculation assumes: i) Thermodynamic equilibrium condition, ii) random distribution of Sn atoms in Ge crystal and vibration of lattice constants due to fluctuation of alloy mixing negligible, , iii) thin film thickness below the critical thickness limit and (iv) Sn oversaturation condition.

The Gibbs free energy could be expressed as

$$\Delta G(x, T) = \Delta H(x, T) - T\Delta S(x, T) + E_s(x) \quad \text{Equation 6.1}$$

where  $x$  and  $T$  are Sn composition and system temperature, respectively,  $\Delta H$  and  $\Delta S$  are mixing enthalpy and entropy while  $E_s$  is elastic strain energy per atom.

The ideal enthalpy and entropy are given as

$$\Delta H(x, T) = \alpha x(1 - x) \quad \text{Equation 6.2}$$

$$T\Delta S(x, T) = -kT[x\ln(x) + (1 - x)\ln(1 - x)] \quad \text{Equation 6.3}$$

where  $\alpha$  is interaction parameter which scales proportionally with the square of bond length between two nearest-neighbor atoms[121]. The value of  $\alpha$  could be obtained experimentally by fitting of liquidus and curves in the  $T - x$  phase diagram of the alloy system.

The elastic strain energy per atom is written as[122]

$$E_s(x) = 2\mu \frac{1 + \nu}{1 - \nu} f^2 \quad \text{Equation 6.4}$$

Hereby,  $\mu$  is shear modulus and  $\nu$  is Poisson's ratio. Within critical thickness, the value of strain  $f$  could be simplified as  $\frac{a_{GeSn} - a_{Ge}}{a_{GeSn}}$ , where  $a_{GeSn}, a_{Ge}$  are lattice constants of GeSn and Ge, respectively. Detailed calculations of the whole range  $f$  were provided in section 5.2. The relevant parameters for GeSn system were listed in Appendix A.

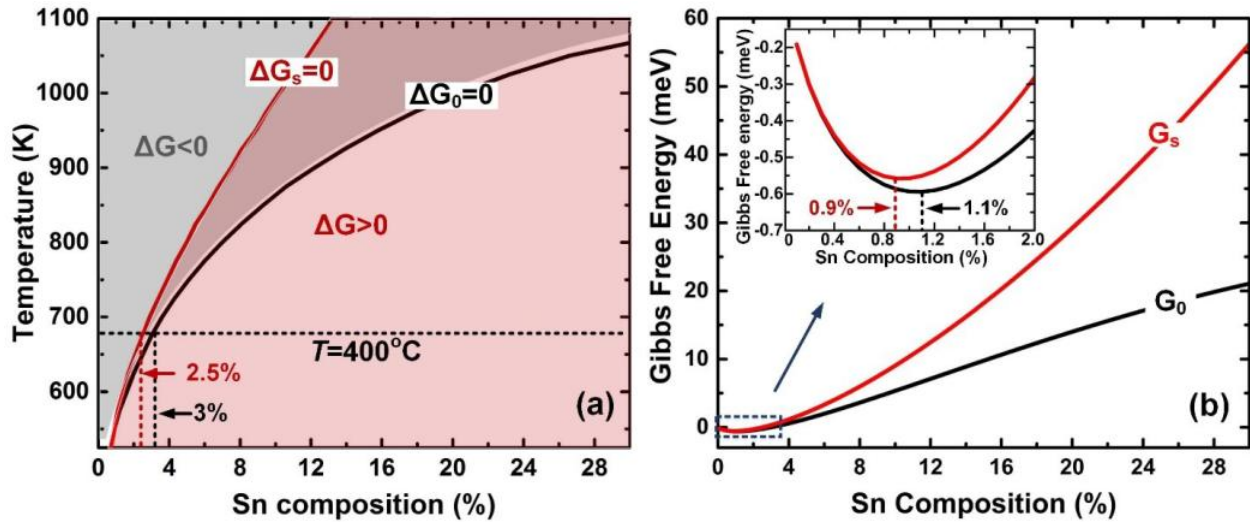


Figure 6.1 (a) Plots of Gibbs free energy  $\Delta G_0 = 0$  and  $\Delta G_s = 0$ . (b) Gibbs free energy plot at  $T=400^\circ\text{C}$  with ( $G_s$ ) and without strain ( $G_0$ ).

The Gibbs free energy  $\Delta G_0 = 0$  and  $\Delta G_s = 0$  are shown in phase diagram of Figure 6.1 (a), representing the stability boundary of unstrained (fully relaxed) and compressively strained GeSn alloy systems, respectively. Hereby, the stability area ( $\Delta G < 0$ ) was marked as grey field while instability area ( $\Delta G > 0$ ) was colored as purple field. Compared with unstrained curve  $\Delta G_0 = 0$ , the whole  $\Delta G_s = 0$  curve shifts to the lower Sn composition range because of elastic strain energy,

thus narrowing the stability area. As a result, the maximum Sn incorporation obtained in stable strained GeSn system decreases compared with unstrained system under the same temperature. For  $T=400^{\circ}\text{C}$ , which is the upper limit temperature of our growth, the maximum Sn composition for strained system is 2.5%, smaller than 3% of unstrained one. More discrepancy of maximum Sn composition appears at higher temperature range. Similar composition-stability relationship was further clarified by the calculation of Gibbs free energy  $G(x, T)$  at  $T=400^{\circ}\text{C}$ , which was plotted in Figure 6.1 (b). As shown in the inserted zoomed-in curves, the minimum free energy for strained and unstrained system occurs at 0.9% and 1.1% Sn composition, respectively. Since  $\Delta G < 0$  is the driving force of stable crystallization, Sn atoms tend to incorporate less in strained GeSn system compared to unstrained one in order to minimize Gibbs free energy. The more strained energy accumulates, the less Sn incorporates into GeSn system.

## 6.2. Bindoal and spinodal curves

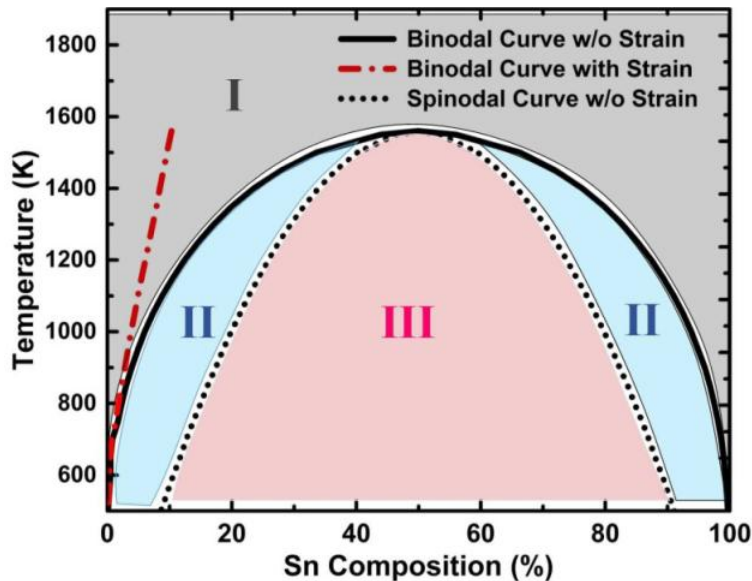


Figure 6.2 Temperature-composition ( $T - x$ ) phase diagram of GeSn.

The  $T - x$  phase diagram was shown in Figure 6.2, in which binodal and spinodal curves for strained system were calculated under equilibrium condition. Binodal curve represents the

equilibrium solubility of Sn at the given temperature, corresponding to Sn composition at the minimum point of Gibbs free energy where  $\frac{\partial G}{\partial x} = 0$ . The spinodal composition was calculated as  $\frac{\partial^2 G}{\partial x^2} = 0$ . Beyond the spinodal composition the system becomes unstable and spinodal decomposition occurs. The critical temperature  $T_c=1560$  K is achieved at the top merging point of both binodal and spinodal curves, above which the alloy becomes miscible for all the compositions with random Sn distribution. Below critical temperature, the miscibility gap occurs. The  $T - x$  diagram is divided into three regions by binodal and spinodal curves: I) Stable region in which GeSn system keeps stable. II) Metastable region. Spontaneous decomposition of GeSn is hampered by the activation energy barrier. III) Unstable region in which GeSn decomposes spinodally. The binodal curve of strained GeSn system is also drawn in the diagram. Comparing to unstrained system, the strained binodal curve shifts to lower Sn composition at the given temperature, which is consistent with the results shown in Figure 6.1.

### **6.3. Interplay between strain and Sn composition**

In the 2<sup>nd</sup> layer of GeSn, the relationship between compressive strain and Sn incorporation are interactive. As discussed above, more Sn could be incorporated with gradual relaxation of compressive strain, leading to the increase of local microscopic lattice constant. Therefore, more compressive strain is introduced for successive epitaxy of several atomic layers, which in turn impedes Sn incorporation. The interplay between strain and Sn incorporation delays the occurrence of maximum Sn incorporation and results in the long Sn-enhanced tail with continuous growth. Although the world-record maximum Sn composition of 22.3 % has been achieved in this study, the steep gradient rates at 2<sup>nd</sup> layer shown in SIMS suggest that Sn incorporation is far from saturation at the end of GeSn growth. The further continuous growth with the same recipe would



lead to the “true” maximum Sn composition which is eventually limited by surface chemical reaction. The detailed analysis is under investigation and will be reported later.

## Chapter 7. High Sn-content GeSn Edge Emitting Laser

### 7.1. Sample growth

Two GeSn samples A and B was investigated in this work which were grown on relaxed Ge buffer on Si substrate using ASM Epsilon<sup>®</sup> 2000 Plus reduced pressure CVD (RPCVD) system. The commercially available precursors of GeH<sub>4</sub> and SnCl<sub>4</sub> were utilized. Detailed growth information could be found somewhere else[44]. For both samples, GeSn virtual substrate (VS) was firstly grown on Ge buffer with the maximum Sn composition of 16.5% achieved. Both samples were then grown using multiple-step Sn-enhanced growth recipe. During each growth step of Sn enhancement the gradient rate of Sn composition was carefully designed to maintain the continuous epitaxy. After the epitaxy the total GeSn thicknesses of sample A and sample B were obtained as 1210 and 1420 nm, respectively. Sample A achieved the maximum Sn composition of 22.3%, an unprecedented value so far for CVD technology while sample B was obtained the maximum Sn content as 20.0%.

Table 7.1 The summary of Sn content, the maximum compressive strain, and the minimum bandgap for sample A and sample B. The experimental bandgap was extracted from PL spectra at 300 K.

Sample	GeSn thickness (nm)	The maximum Sn content (%)	Strain (%)	Theoretical/experimental bandgap (eV)
A	1210	22.3	-0.61	0.359/0.372
B	1420	20.0	-0.52	0.375/0.372

The GeSn thickness and material quality were studied by transmission electron microscopy (TEM). Sn composition was determined by Secondary Ion Mass Spectrometry (SIMS) and cross checked by data fitting of reciprocal space mapping (RSM) of X-ray diffraction (XRD). Strain

information was analyzed by RSM of XRD. Table 7.1 lists the corresponding information of sample A and B.

## **7.2. Structural material characterization**

Cross sectional dark field TEM images in Figure 7.1 (a) and (d) indicate the two layer structure of GeSn for sample A and B, respectively: (i) a highly defective layer (1<sup>st</sup> layer) with thickness of 380 nm for sample A and 450 nm for sample B. The dislocation network forms as the 1<sup>st</sup> layer near GeSn/Ge interface in order to accommodate large lattice mismatch between Ge and GeSn. The majority of misfit dislocations were localized within the 1<sup>st</sup> layer; (ii) a low defect layer (2<sup>nd</sup> layer) with thickness of 830 nm and 970 nm for sample A and B, respectively. The extremely high quality GeSn was obtained at the 2<sup>nd</sup> layer without the propagation of threading dislocations, which is ideal for laser applications. Correspondingly, the two distinct layers observed from TEM images were also marked in SIMS results of sample A and B as shown in Figure 7.1 (b) and Figure 7.1 (e), respectively. SIMS results for sample A and B exhibit the similar behavior of Sn composition. Both the 1<sup>st</sup> and 2<sup>nd</sup> layers exhibit spontaneously Sn enhanced gradient. The 1<sup>st</sup> layer was further divided in two regions bounded by point X in Figure 7.1 (b) and 7.1 (e), respectively: (i) region I of constant low Sn content of 12% (sample A) and 11.9% (sample B); (ii) region II of steep Sn-content grading rate of 21.5%/μm (sample A) and 26.7%/μm (sample B). In contrast of region II, the moderate Sn-content grading rates in the 2<sup>nd</sup> layer of sample A and B were obtained as 6.2%/μm and 3.8%/μm, respectively. The boundary between the 1<sup>st</sup> and 2<sup>nd</sup> layer was marked as point Y. The averaged Sn contents in the 2<sup>nd</sup> layer were calculated as 18.1% for sample A and 17.8% for sample B, which were marked as point Z on SIMS curves. Sn composition associated with compressive strain was also obtained by the data fitting of RSM of XRD. From Sn composition fitting, the point X, Y, Z on SIMS curve were also identified on RSM color contour. The

compressive strain analysis at point X, Y, Z reveals strain relaxation mechanism of GeSn along the growth direction. To take sample A as an example, the point X and Y on RSM exhibit strain relaxation degree of 94% and 70%, respectively. The line X-Y represents crystallization process at 1<sup>st</sup> layer of GeSn. The fact that X-Y line follows the trend of relaxation line suggests that the 1<sup>st</sup> layer is quasi-relaxed. It was attributed to the formation of dislocation network near the GeSn/Ge interface observed from TEM images shown in Figure 7.1 (a). Large amounts of dislocations were introduced in the 1<sup>st</sup> layer in order to release accumulated strain energy, leading to the high degree of relaxation. Point Z represents the 2<sup>nd</sup> layer and shows highly compressive strain of -0.62%. The vertical line Y-Z indicates the pseudomorphic growth of the 2<sup>nd</sup> layer, which shows high consistency with TEM result. The 2<sup>nd</sup> layer in TEM image shows few misfit dislocations, suggesting the pseudomorphic growth of GeSn. The RSM of sample B exhibits the similar behavior of sample A, further confirming the quasi-relaxed 1<sup>st</sup> layer and pseudomorphic 2<sup>nd</sup> layer of GeSn.

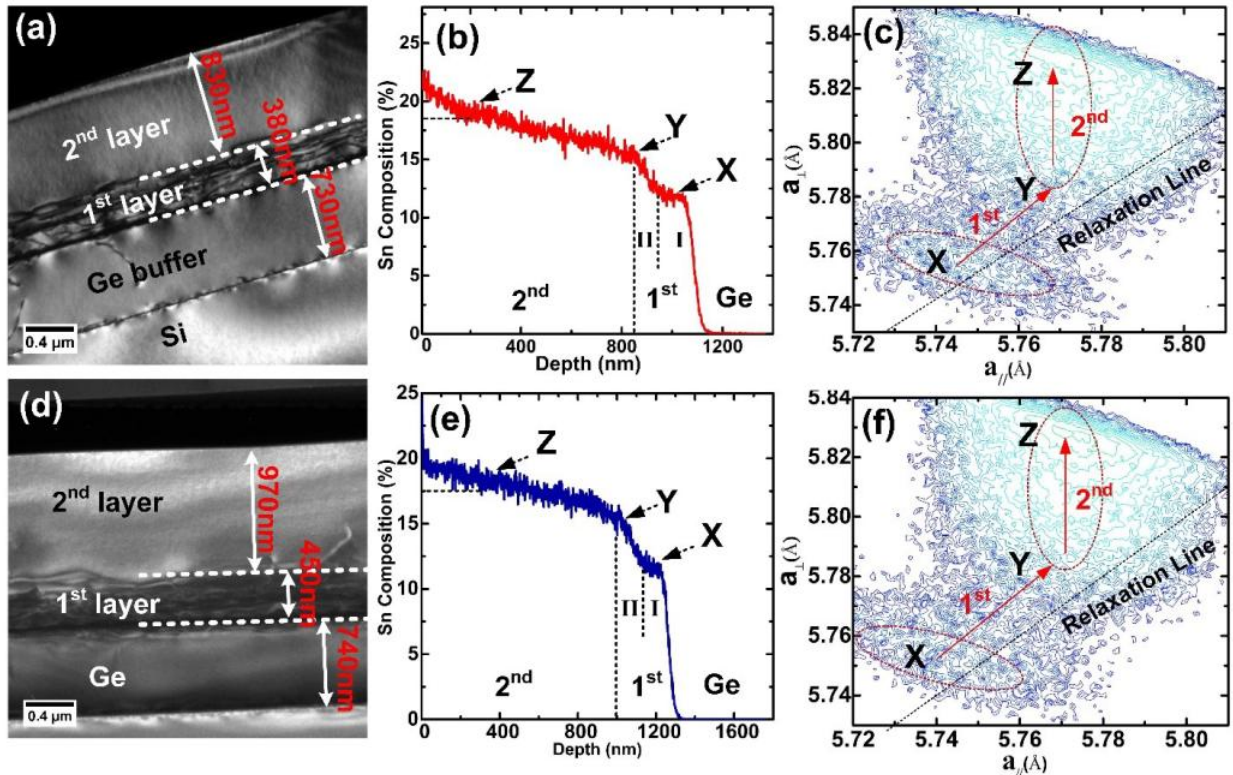


Figure 7.1 Cross sectional dark field TEM images of (a) sample A and (d) sample B viewed from  $[\bar{1}10]$  direction. SIMS plots as a function of depth for (b) sample A and (e) sample B. RSM contour plots of (c) sample A and (f) sample B.

### 7.3. The bandgap diagram calculation

The bandgap diagram along growth direction was calculated based on deformation potential theory[123], in which the relevant parameters such as bandgap energy, deformation potentials and elastic constants could be found in Appendix A. The result of bandgap diagram was plotted in Figure 7.2 (b). Four subbands were considered including indirect ( $E_{cL}$ ) and direct ( $E_{c\Gamma}$ ) valleys in conduction band and heavy hole ( $E_{vHH}$ ) and light hole ( $E_{vLH}$ ) in valence band, respectively. The uncertainty of  $E_{cL}$  and  $E_{c\Gamma}$  originates from different adoption of bandgap bowing parameters of indirect ( $b_L$ ) and direct ( $b_\Gamma$ ) band edge, which are crucial and have been predicted by various research team [97][98][99]. However, none of these reach an experimental agreement on the value of bowing parameters. For the best description of band diagram, the upper limits of  $b_L=1.23$  eV[98],  $b_\Gamma=2.49$  eV[124] and lower limits of  $b_L=0.68$  eV[97],  $b_\Gamma=1.94$ eV[98] were adopted, respectively. Ge buffer undergoes tensile strain as 0.19% after high temperature annealing due to the difference of thermal expansion coefficients between Si substrate and Ge. The tensile strain results in the decrease of energy difference between  $E_{cL}$  and  $E_{c\Gamma}$  and the energy splitting between  $E_{vHH}$  and  $E_{vLH}$ . In contrast, GeSn grown on Ge buffer is under compressive strain, resulting in the  $E_{vHH}$  band lifting above  $E_{vLH}$  band. The whole GeSn layer exhibits the direct bandgap characteristics as the result of competition between Sn incorporation and compressive strain. At region I of the 1<sup>st</sup> layer, the constant low Sn composition and high strain relaxation result in the small change of the bands. At region II, Sn content increase rapidly, leading to the sharp decrease of both direct and indirect bandgap. Meanwhile, the compressive strain accumulates during the epitaxy, resulting in the continuous increase of energy difference between  $E_{vHH}$  and  $E_{vLH}$ . The 2<sup>nd</sup>

layer continues the change of band edge in region II. On the top of the 2<sup>nd</sup> layer of GeSn the minimum bandgap was obtained between 0.275 and 0.360 eV.

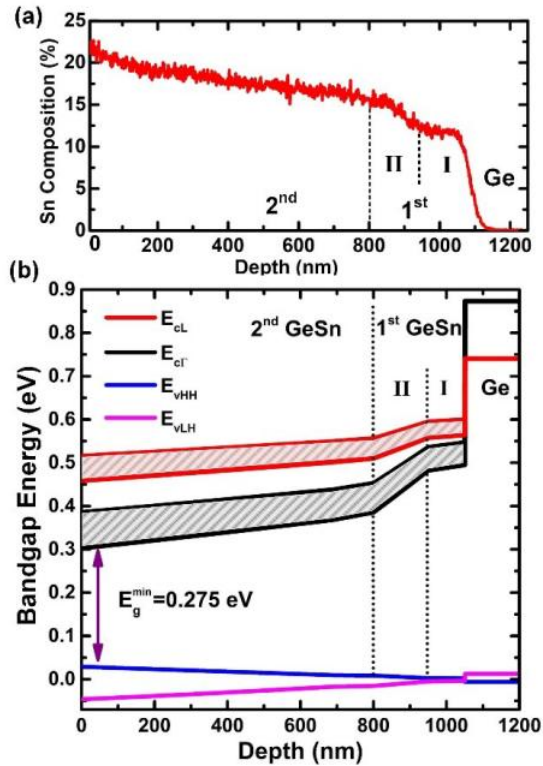


Figure 7.2 (a) SIMS profile of sample A. (b) The band diagram calculation of sample A with Sn compositional graded GeSn structure.

#### 7.4. Photoluminescence (PL) measurement

In order to evaluate the optical properties and the bandgap directness of GeSn, the temperature-dependent photoluminescence (PL) of sample A was measured, as shown in Figure 7.3 (a1) and (a2). A continuous wave (CW) laser emitting at 532 nm wavelength was used as optical-pumping source. The beam size was 100  $\mu\text{m}$  in diameter. PL emission was spectrally analyzed by the combination of iHR320 spectroscopy and liquid nitrogen cooled Indium Antimonide (InSb) detector with the wavelength detection cut-off at 5  $\mu\text{m}$ . A SR830 DSP lock-in system along with a chopper was applied to amplify the PL signal. The blue shift of PL peak following Varshni empirical model was clearly observed in PL spectra as the temperature decreases from 300 to 10

K. The PL intensity increases dramatically as the sample cools down. As Figure 7.3 (a2) shows, the peak PL intensity increases 65 times from 300 to 10 K. Meanwhile, the full width half maximum (FWHM) decreases rapidly. All the evidences suggest that PL emission originates from radiative recombination of the true direct bandgap between  $E_{c\Gamma}$  and  $E_{vHH}$ . The PL position at 300 K was extracted as 3340 nm (0.371 eV) by Gaussian data fitting. Using the equation:  $E_g = h\nu - \frac{1}{2}kT$ , The direct bandgap energy was calculated as 0.358 eV, which is consistent with the band diagram calculation in Figure 7.2 (b). Note that the light absorption from ambient environment was observed in room-temperature PL spectrum at  $\sim 3400$  nm wavelength. The integrated PL intensity and peak position at each temperature were extracted, as plotted in Figure 7.3 (b). The main peak in PL spectra shifts from 0.371 to 0.411 eV and the integrated PL intensity increases 50 times from 300 to 10 K. The power-dependent PL was also investigated, as shown in Figure 7.3 (c). The PL intensity increases significantly with the increase of excitation power density, as expected. The main peak of spectra exhibits a clear blue shift with high excitation power. The corresponding wavelength shifts from 3130 to 3032 nm when the pumping power density increases from 32 to 960 W/cm<sup>2</sup>. Meanwhile, the FWHM of PL spectra increases dramatically as the pumping power increases. The clear blue shift of wavelength could be explained by the typical band-filling effects, which is more pronounced in the tilted band diagram as a result of graded Sn composition. On the surface region of GeSn layer, the  $E_{c\Gamma}$  conduction band and  $E_{vHH}$  valence band could be simplified as the triangular potential model. The  $E_{c\Gamma}$  band energy as the function of depth was drawn in Figure 7.3 (d). When the excitation rate of carriers exceeds the instantaneous recombination rate, the photogenerated carriers are spatially distributed within the penetration depth into GeSn for a laser source. Then the excess carriers redistribute and transport towards the top of GeSn layer where the narrowest energy band edge locates. At low excitation power, the

majority of carriers accumulate at the surface region of GeSn and the interband optical transition mainly occurs at the narrowest energy band edge. As the excitation power increases, a large proportion of carriers populate at the wider energy band edge which spatially locates at the inner region of GeSn layer as a result of Pauli Exclusion Principle. Therefore, the light emissions occur at the wider band edge, leading to the blue shift of the main PL peak. The broad spatial population of carriers also results in the increase of FWHM. The theoretical spontaneous emission of the triangular potential model was calculated in the inset of Figure 7.3 (d), further confirming the blue shift of PL under high excitation power.

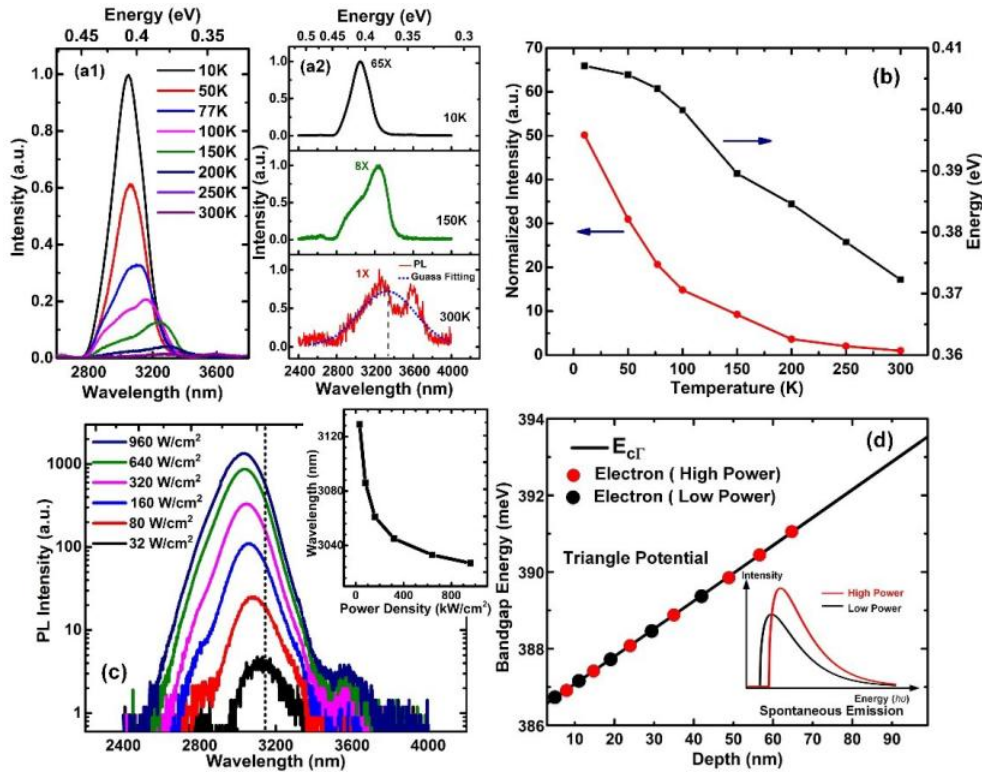


Figure 7.3 (a1), (a2) Temperature-dependent PL spectra. (b) The integrated PL intensity and peak position as a function of temperature. (c) Power-dependent PL spectra at 10 K. Inset: Blue shift of wavelength with increasing power density. (d) Band filling effect in triangular potential model. Inset: calculation of spontaneous emission in triangular potential well.

### 7.5. Optically pumped GeSn edge emitting laser

The GeSn sample was fabricated to the 5  $\mu\text{m}$ -width and 1.25 mm-length strip waveguide as optical pumped edge emitting devices to investigate the temperature-dependent lasing performance. The depth of side wall was etched as 800 nm. The wet chemical etching process at low temperature 0°C was employed using chemical mixture of  $\text{HCl}:\text{H}_2\text{O}_2:\text{H}_2\text{O}=1:1:10$ . The average etching rate was controlled as 20 nm/min and etching depth was measured as 1  $\mu\text{m}$ . After the etching, the sample was back lapped down to 70  $\mu\text{m}$  and the cleavage process was followed to form the Fabry-Perot facets. The optical pumped lasing performance was investigated using a 1060 nm pulsed laser with 45 kHz repetition rate and 6 ns pulse width. The laser beam was collimated to a 20  $\mu\text{m}$ -width and 3.2 mm-length pumping strip on to GeSn waveguide structure by a cylindrical lens. The samples was first mounted on a Si chip carrier and put into a liquid nitrogen cold-finger cryostat. Figure 7.4 shows the schematic diagram of GeSn laser devices and the optically pumped lasing setup. A computer-controlled variable attenuator was used to automatically measure typical laser-input versus laser-output (L-L) curve. Through rotating the motor-controlled  $\frac{1}{2} \lambda$  wave plate sandwiched by two linear polarizers, the continuous power change of pumping laser could be obtained with the automatic control.

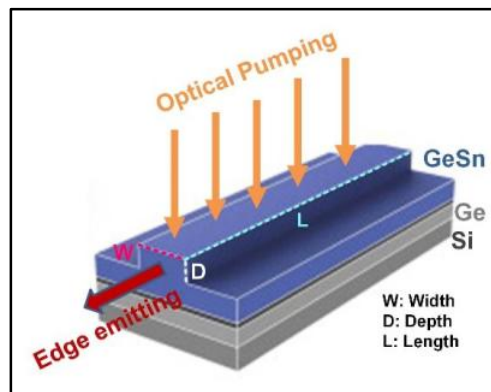


Figure 7.4 The schematic diagram of GeSn laser devices and optically pumped lasing setup.



The laser devices of sample A and B with 5  $\mu\text{m}$  width were named as sample A-5 $\mu\text{m}$  and sample B-5 $\mu\text{m}$ , respectively. The temperature-dependent laser-input versus laser-output (L-L) curves for sample A-5 $\mu\text{m}$  and B-5 $\mu\text{m}$  were plotted in Figure 7.5 (a) and (b), respectively. The “kink” behavior of L-L curves for both samples features the typical lasing behavior with distinct lasing threshold power density. The sharp slope of integrated intensity above the “kink” indicates that the lasing emission dominates over spontaneous emission. Through linear data fitting around the “kink” area on the curve, the threshold power density at 77 K for sample A, B-5 $\mu\text{m}$  were obtained as 203, 168  $\text{kW}/\text{cm}^2$ , respectively. The higher lasing threshold of sample A-5 $\mu\text{m}$  compared to sample B-5 $\mu\text{m}$  is likely due to the degraded material quality as it features the world-record high Sn incorporation. The characteristic temperature of lasing  $T_o$  was also investigated with sample A-5 $\mu\text{m}$  as an example, as shown in the inset of Figure 7.5 (a). The  $T_o$  could be determined by fitting the data of lasing threshold versus temperature. The lasing threshold could be expressed as[93]:

$$P_{th}(T) = P_0 e^{\frac{T-T_1}{T_0}} \quad \text{Equation 7.1}$$

where  $P_{th}(T)$  is the lasing threshold,  $P_0$  is the constant,  $T_1$  is the absolute temperature and  $T_0$  is the characteristic temperature which is often used to measure the temperature sensitivity of threshold. The high characteristic temperature  $T_0$  indicates the good temperature performance of lasing.

Through the data fitting of temperature-dependent lasing threshold the  $T_o$  was extracted as 70 K, which is comparable with the previously demonstrated GeSn laser[41][43]. Figure 7.5(c) and (d) show the temperature-dependent lasing spectra at 1.5 times of lasing threshold for sample A and B-5 $\mu\text{m}$ , respectively. The multimode characteristics of longitudinal Fabry-Perot resonances were clearly observed. Unfortunately the free spectral range (FSR) of spectra could not be exactly extracted due to the long cavity length (1.25 mm) and the limited resolution of spectrometer (up

to  $>0.1$  nm). The typical red shift of lasing peak with increase of temperature was observed for both spectra, which follows the temperature-dependent shift of optical gain. At the maximum lasing temperature of 150 K (sample A- $5\mu\text{m}$ ) and 130 K (sample B- $5\mu\text{m}$ ), both lasing peaks achieve 3000 nm.

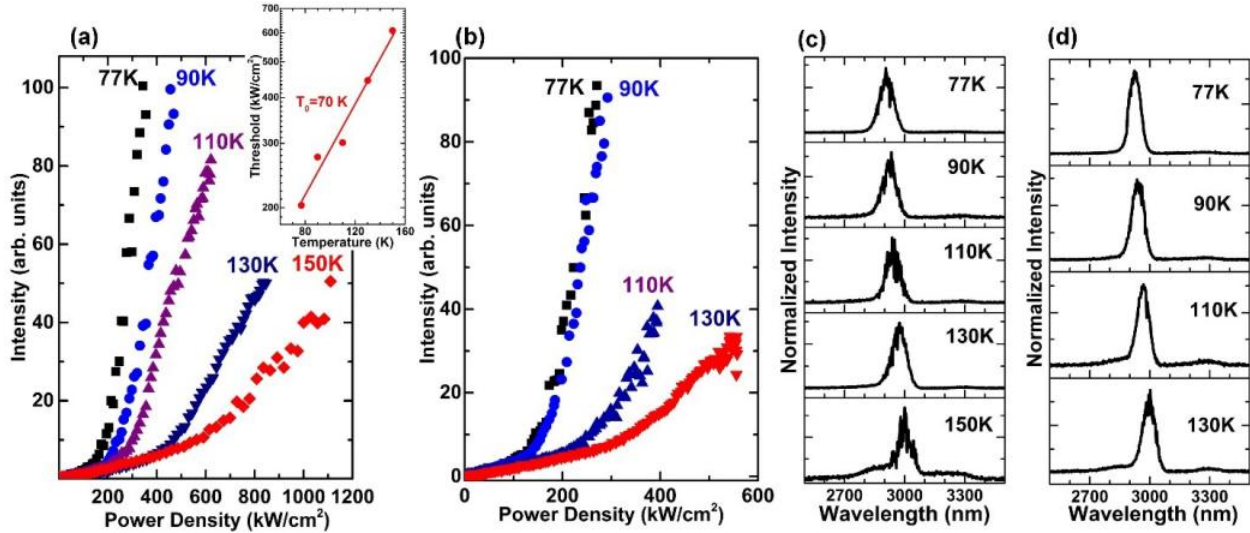


Figure 7.5 The temperature-dependent L-L curves of the edge emitting devices for (a) sample A- $5\mu\text{m}$  and (b) sample B- $5\mu\text{m}$ . Inset: characteristic temperature  $T_0$  was extracted as 70 K. Lasing spectra at different temperature for devices of (c) sample A- $5\mu\text{m}$  and (d) sample B- $5\mu\text{m}$ . kkkk

The comparison of lasing at 1.5 times of lasing threshold and PL spectra at 77 K temperature for sample A- $5\mu\text{m}$  was conducted, as plotted in Figure 7.6. The FWHMs of lasing and spontaneous PL spectra were fitted as 85 nm (12.5 meV) and 305 nm (40 meV), respectively. The clear blue-shift of lasing peak compared to PL peak was observed as 165 nm. It could also be explained on the basis of the band filling effect. The peak power density per pulse of 1064 nm pumping source for GeSn lasing was calculated four orders of magnitude higher than that of 532 nm continuous wave pumping source for PL. Such a high pumping rate of GeSn results in the huge number of carrier accumulation and the pronounced blue shift of lasing peaks, as explicitly shown in Figure 7.3 (c) and (d). Note that the ultra-high carrier accumulation on the band edge will also cause the narrowing of intrinsic band-gap, a typical band-gap renormalization by down-shift of conduction

band edge and up-shift of valence band edge due to the self-energy effects[125]. However, the corresponding red-shift by band-gap renormalization was highly overcompensated by the blue-shift of band filling effects. The inset shows pattern of fundamental transverse electric ( $TE_0$ ) mode at the lasing wavelength of 2900 nm which was calculated by Lumerical 2D mode solver. The effective refractive index was calculated as 4.31. The optical confinement factor of the low-defect 2<sup>nd</sup> GeSn layer was obtained as 74.6%, suggesting the majority of generated light was strongly confined inside the waveguide. The superior optical confinement favors high modal gain at the active region of waveguide.

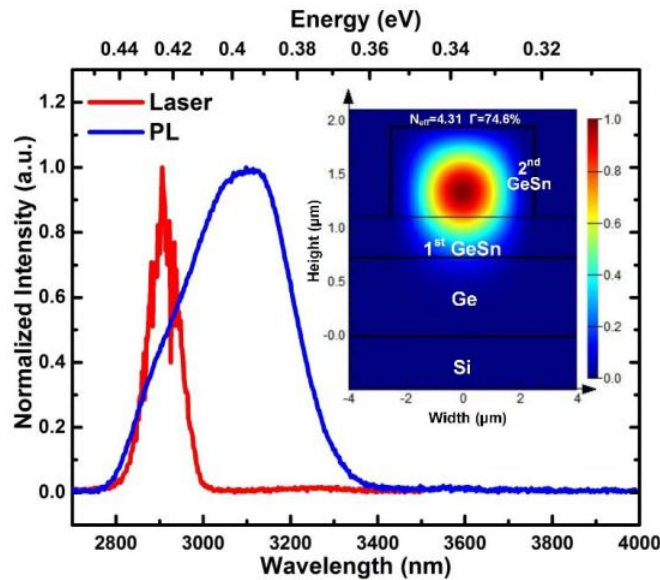


Figure 7.6 Comparison of Lasing and PL spectra for sample A-5 $\mu$ m at temperature of 77 K. Inset: The pattern of  $TE_0$  mode at the lasing wavelength of 2900 nm.

### 7.6. Room temperature GeSn laser

Although the GeSn laser has achieved 3  $\mu$ m lasing wavelength with the high Sn content of 20% (Sample A) and 22.3% (Sample B), the operating temperature is limited within 150 K due to the severe heating effects induced by the 1064 nm pumping laser. In order to reduce the heating effect and increase the operating temperature of GeSn laser, three potential solutions were proposed as follows:

1) The first is to decrease the duty cycle of optically pumped laser. By increasing the “cooling down” time of optical pumping, the heating effects could be minimized. The current frequency and pulsed width of the 1064 nm pumping laser is 45 kHz and 6 ns, respectively. The corresponding duty cycle is 0.027%. For the 1064 nm pumping laser, the duty cycle could be tuned by changing the laser frequency. For example, if the frequency of 1064 nm pumping laser decreases to the minimum of 10 kHz, the pulse width reduces to 3 ns. Therefore, the duty cycle could be tuned down to 0.003%, which is nine times smaller than the current one.

2) The second is to choose the large size of GeSn lasing devices. The large dimension of GeSn devices helps reduce the equivalent surface recombination from the side wall. Therefore, the large size of device is supposed to have high operating temperature and low lasing threshold.

3) The third is to use the longer-wavelength optically pumped laser. In this section, the 1950 nm laser with the frequency of 10 kHz and the pulse width of 10 ns was also employed for GeSn lasing study. The 1950 nm pumping laser could reduce the heating effects significantly. Since the photon energy of 1064 nm pumping (1.17 eV) is higher than the bandgap energies of Ge buffer (0.8 and 0.66 eV for direct and indirect bandgap, respectively), large numbers of photons could be absorbed by Ge buffer, which results in the severe local heating. In contrast, the photon energy of 1950 nm pumping (0.64 eV) is smaller than bandgap energies of Ge and therefore the photons could only be absorbed by GeSn layer, resulting in no heating factor from Ge buffer. Additionally, the carriers at the Ge buffer excited by 1064 nm pumping have a transport process towards GeSn layer, which generates the heating during the interaction between carriers and phonons via the lattice scattering mechanism. While under the 1950 pumping, no carrier transport process from Ge buffer to GeSn is expected.

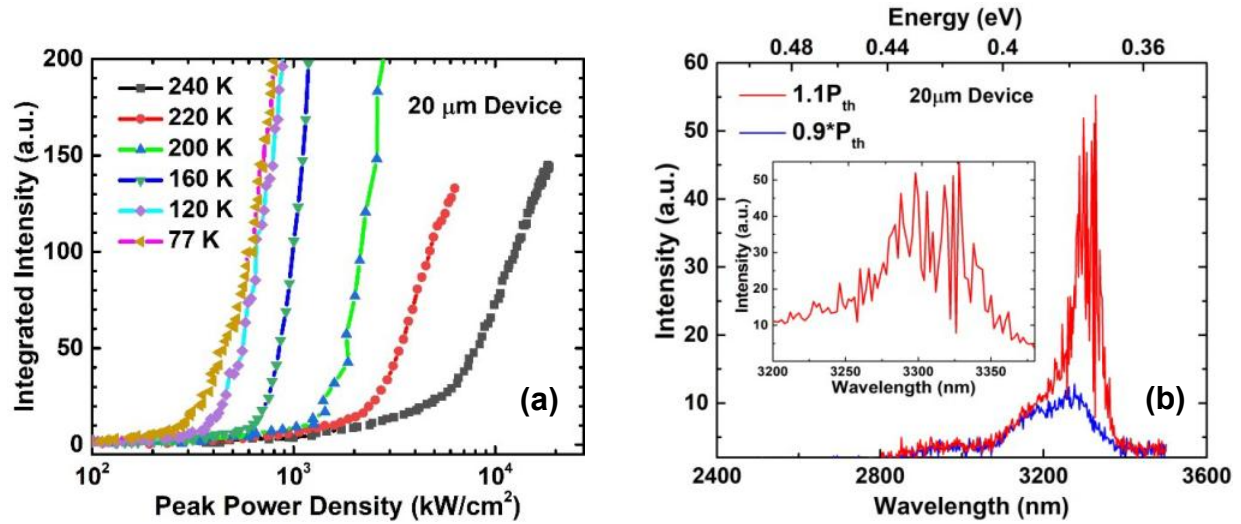


Figure 7.7 (a) The temperature-dependent L-L curves of sample B-20  $\mu\text{m}$  devices. The 1064 nm pumping laser was utilized. (b) The lasing spectra at the temperature of 200K. The inset: Zoomed-in lasing spectra.

We investigated the lasing behavior of sample B-20  $\mu\text{m}$  devices with 2.6 mm length using 1064 nm pumping laser. The frequency and duty cycle of the pumping laser are 10 kHz and 0.003%, respectively. The temperature-dependent L-L curves were shown in Figure 7.7 (a). The “knee” behavior were clearly observed, suggesting the lasing characteristics. The lasing threshold at 77 K temperature was extracted 268  $\text{kW}/\text{cm}^2$ . The operating temperature was significantly extended to 240 K. The significant increase of operating temperature is attributed to the reduction of heating effects by reducing the duty cycle of pumping laser. The typical multiple mode of lasing at 200 K was shown in Figure 7.7 (b). At 0.9 times power density of lasing threshold ( $0.9 \cdot P_{\text{th}}$ ) only spontaneous PL spectrum was observed with the peak position of 3236 nm. At  $1.1 \cdot P_{\text{th}}$  power density the multimode of lasing was clearly shown. The corresponding amplified PL peak position is 3310 nm. The zoomed-in lasing spectrum was shown in the inset of Figure 7.7 (b). The fully width of half maximum (FWHM) of single mode lasing was measured as 2 nm (0.23 meV), which is 94 times smaller than the FWHM of spontaneous PL as 188 nm (22.3 meV) at  $0.9 \cdot P_{\text{th}}$  power density.

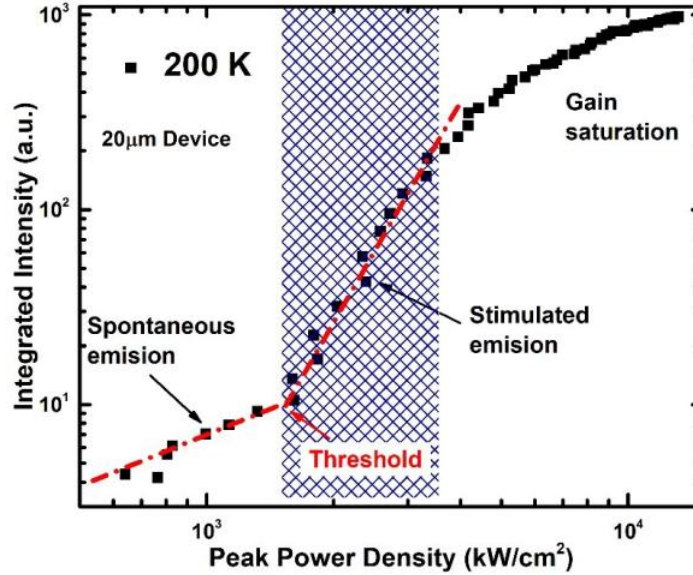


Figure 7.8 The L-L curve of sample B-20µm at the temperature of 200 K. Note: The logarithmic scales of both x and y axis

The L-L curve of sample B-20µm at the temperature of 200 K was drawn in Figure 7.8. By the linear data fitting of the curve, the lasing threshold could be determined as 1610 kW/cm<sup>2</sup>. Below the lasing threshold, the spontaneous emission dominates the light output. Above the threshold, the condition of population inversion is satisfied and the intensity of light emission increases dramatically via the stimulated emission process. Meanwhile, since the majority of carriers recombine via stimulated emission, the carrier density in GeSn devices is pinned at the threshold power density. As a result, the intensity of spontaneous emission was clamped at the threshold power density as well. When the input power density exceeds 350 kW/cm<sup>2</sup> the saturation of light output occurs due to the heating effect, Auger process and non-linear optical effect introduced by the high carrier density.

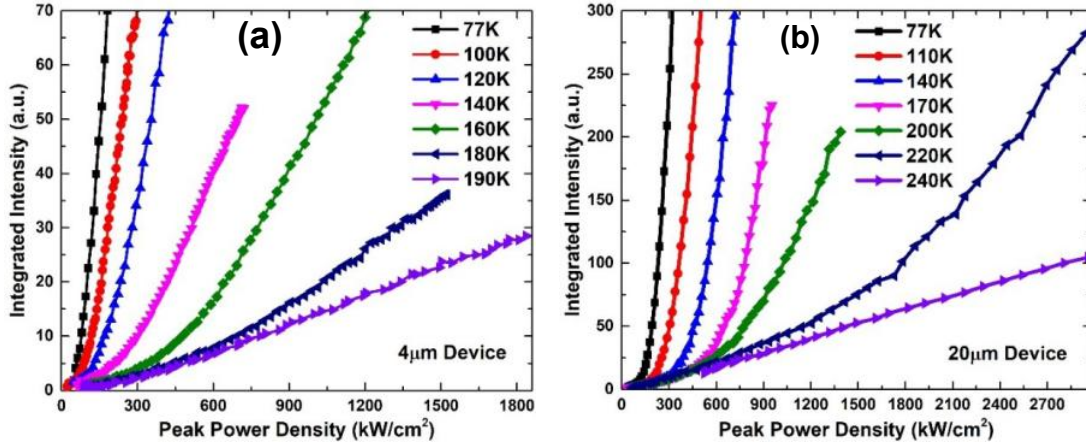


Figure 7.9 (a) The temperature-dependent L-L curves of sample A-4 $\mu$ m devices. (b) The temperature-dependent L-L curves of sample A-20 $\mu$ m devices.

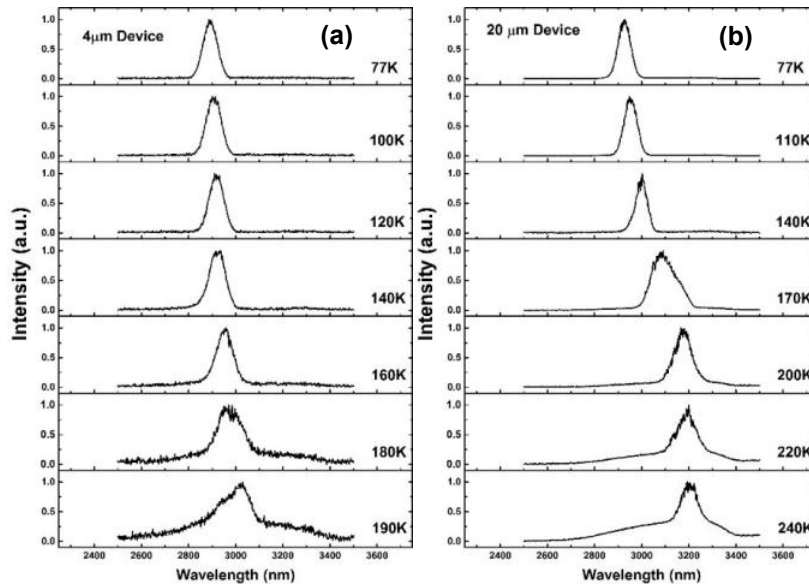


Figure 7.10 (a) The temperature-dependent lasing spectra of sample A-4 $\mu$ m devices. (b) The temperature-dependent lasing spectra of sample A-20 $\mu$ m devices.

In order to further improve the GeSn lasing temperature, the 1950 nm-wavelength pumping laser was used for the investigation of GeSn laser behavior. Two GeSn laser devices of sample A with the width of 4 and 20  $\mu$ m were employed for lasing measurements. The temperature-dependent L-L curves for both sample A-4 $\mu$ m and -20 $\mu$ m were shown in Figure 7.9 (a) and (b), respectively. The GeSn device of sample A-4  $\mu$ m has a lasing temperature up to 180 K by adopting the 1950 nm pumping laser. In contrast, the lasing temperature of sample A-5  $\mu$ m device is 150 K by using



1064 nm pumping laser. The increase of operation temperature using 1950 nm laser is attributed to the reduced heating effect. Under the same temperature the lasing threshold of sample A-4  $\mu\text{m}$  device is lower than the one of sample A-20  $\mu\text{m}$  device. For example, at 77 K, the lasing thresholds of the devices of sample A-4  $\mu\text{m}$  and -20  $\mu\text{m}$  are 150 and 184  $\text{kW}/\text{cm}^2$ , respectively. The highest lasing temperature of sample A-4  $\mu\text{m}$  device is 180 K while the one of sample A-20  $\mu\text{m}$  is 240 K, confirming that the wider device has higher lasing temperature. The lasing spectra of sample A-4  $\mu\text{m}$  and -20  $\mu\text{m}$  were shown in Figure 7.10 (a) and (b), respectively. Both devices exhibit a clear red shift of lasing peak with the increase of temperature. From 77 to 180 K, the lasing peak of sample A-4  $\mu\text{m}$  device shifts from 2890 to 2954 nm. In contrast, the lasing peak of sample A-20  $\mu\text{m}$  device shifts from 2928 to 3204 nm.

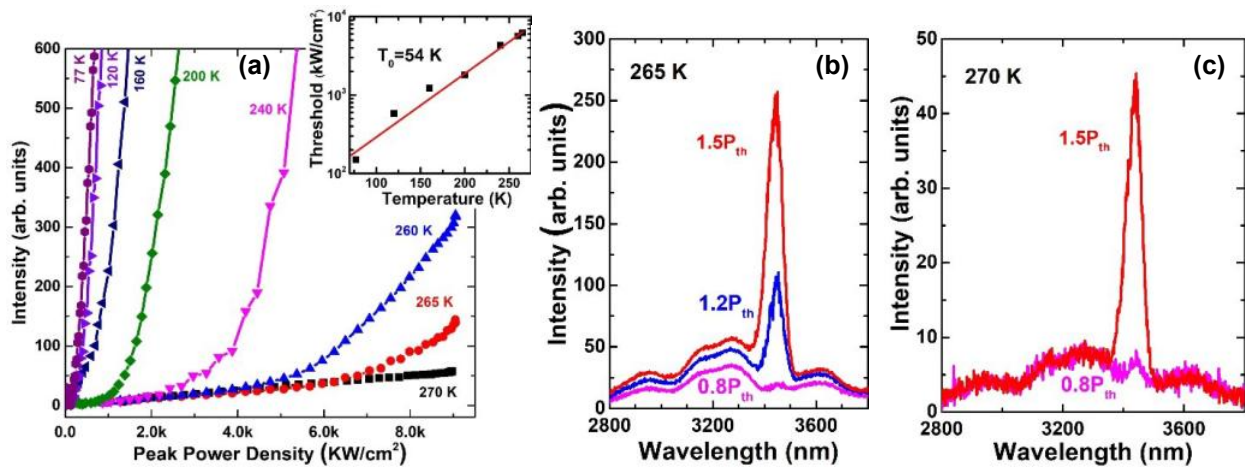


Figure 7.11 (a) The temperature-dependent L-L curves of lasing devices of sample B with 80  $\mu\text{m}$  width by using the 1950 nm pumping laser. The power-dependent lasing spectra at the temperature of (b) 265 K and (c) 270 K.

By optimizing the GeSn laser devices and optically pumped lasing setup, the near room lasing temperature was eventually achieved by the lasing devices of sample B with the width of 80  $\mu\text{m}$  under 1950 nm pumping laser. The temperature-dependent L-L curves were drawn in Figure 7.11 (a). The highest lasing temperature could extend up to 270 K, which is near room temperature. The power density of lasing threshold was extracted as 150  $\text{kW}/\text{cm}^2$  at the temperature of 77 K. The



lasing thresholds at the different temperatures were also extracted. Through the data fitting, the characteristic temperature could be determined as 54 K. The power-dependent lasing spectra at the temperature of 265 and 270 K was shown in Figure 7.11 (a) and (b), respectively. Below the threshold, the spontaneous PL spectra were observed for both operating temperatures of 265 and 270 K. At the 1.5 times of lasing threshold ( $P_{th}$ ), the clear multimode lasing spectra were shown. At the maximum lasing temperature of 270 K, the lasing wavelength extends up to 3442 nm, an unprecedented worldwide achieved lasing wavelength so far. Table 7.2 summarizes the lasing results of GeSn lasing devices studied in this chapter. The near room-temperature lasing behavior demonstrates that GeSn laser has a huge potential towards commercialized mid- infrared laser which could monolithically integrate on Si platform.

Table 7.2 The summary of GeSn lasing results.

Sample	Dimension of laser device			Lasing performance			
	Width ( $\mu\text{m}$ )	Length (mm)	Depth (nm)	Pumping laser (nm)	Lasing threshold @77 K ( $\text{kW}/\text{cm}^2$ )	Maximum lasing wavelength (nm)	Maximum operation temperature (K)
A	4	1.25	800	1950	150	2890	180
	5	1.25		1064	203	3000	150
	20	1.25		1950	184	3204	240
B	5	1.25		1064	168	3000	130
	20	2.6		1064	268	3266	240
	80	2.9		1950	150	3442	270

## Chapter 8. Advanced GeSn/GeSn/GeSn Quantum Well (QW)

### 8.1. Initial GeSn/GeSn/GeSn QW structure

Single quantum well (SQW) and multiple quantum wells (MQWs) have been widely investigated in the optoelectronic devices due to their advantage in the improvement of electrical and optical confinement and the reduction of threshold current density of lasers. Numerous efforts have been exerted to explore the optical properties of GeSn QWs. The polarization-dependent optical gain of SiGeSn/GeSn/SiGeSn MQWs was theoretically calculated for the GeSn laser application[103][71]. Micro-PL study of GeSn microdisk resonator for Ge/GeSn/Ge QWs was performed and revealed sharp whispering-gallery-mode resonances[52]. The electroluminescence of Ge/GeSn/Ge MQWs light emitting diode (LED) was also demonstrated[126]. However due to the lack of sufficient carrier confinement in GeSn well region, the use of Ge as barrier layer is questionable.

In this section, we report the study on  $\text{Ge}_{0.95}\text{Sn}_{0.05}/\text{Ge}_{0.91}\text{Sn}_{0.09}/\text{Ge}_{0.95}\text{Sn}_{0.05}$  single QW and double QWs as a potential alternative solution for Ge/GeSn QWs. The samples were grown on Ge-buffered Si substrate with a single run epitaxy process using a reduced-pressure chemical vapor deposition (RPCVD) system with commercially available low-cost precursors. The QW structures as well as optical characteristics were studied. Cross sectional transmission electron microscopy (XTEM) was performed to probe the crystal quality of QW structures of each layer. Both X-ray diffraction (XRD) rocking curve and reciprocal space mapping were carried out to quantify thicknesses, strain values and Sn compositions in each layer. Temperature-dependent PL was performed to identify both direct bandgap and indirect bandgap transitions. The electronic band structure and energy level quantization were calculated using effective mass approximation and propagation matrix method. Type-I band alignments for both QWs were achieved, which provided insights for future to obtain a favorable carrier confinement in the QW region.

The QW structures were grown in an industry standard RPCVD (ASM Epsilon<sup>®</sup> 2000) system using a single run epitaxy process. Commercially available GeH<sub>4</sub>, and SnCl<sub>4</sub> precursors were used. The growth temperature was kept below 400°C, which is compatible with complementary metal–oxide–semiconductor (CMOS) process. Strain-relaxed Ge buffer layer with ~ 700 nm thickness was first grown on (100) Si wafer, followed by the growth of QW structures. The original QW structure design is schematically depicted in Figure 8.1. The single QW and double QWs are labeled as Sample A and Sample B, respectively. Sample A consists of a 35.2/37.1-nm thick Ge<sub>0.95</sub>Sn<sub>0.05</sub> barrier, 8.2-nm thick Ge<sub>0.91</sub>Sn<sub>0.09</sub> well and a 9.6-nm Ge interlayer between well and barrier. While sample B contains two stacked single QWs. Both QWs have 16.5-nm thick Ge cap on the top.

Sample A		Sample B	
Ge Cap	16.5 nm	Ge Cap	16.5 nm
Ge <sub>0.95</sub> Sn <sub>0.05</sub>	37.1 nm	Ge <sub>0.95</sub> Sn <sub>0.05</sub>	39.0 nm
Ge interlayer	9.6 nm	Ge interlayer	9.0 nm
Ge <sub>0.9</sub> Sn <sub>0.1</sub> QW	8.2 nm	Ge <sub>0.9</sub> Sn <sub>0.1</sub> QW	8.3 nm
Ge <sub>0.95</sub> Sn <sub>0.05</sub>	35.2 nm	Ge <sub>0.95</sub> Sn <sub>0.05</sub>	40.3 nm
Ge Buffer	700.0 nm	Ge interlayer	9.5 nm
(a)		Ge <sub>0.9</sub> Sn <sub>0.1</sub> QW	9.3 nm
		Ge <sub>0.95</sub> Sn <sub>0.05</sub>	38.7 nm
		Ge Buffer	700.0 nm
		(b)	

Figure 8.1 Schematic diagram of Ge<sub>0.95</sub>Sn<sub>0.05</sub>/Ge<sub>0.91</sub>Sn<sub>0.09</sub>/Ge<sub>0.95</sub>Sn<sub>0.05</sub> (a) SQW (Sample A) and (b) DQW (Sample B) (not to scale).

### 8.1.1. Transmission electron microscopy (TEM) characterization

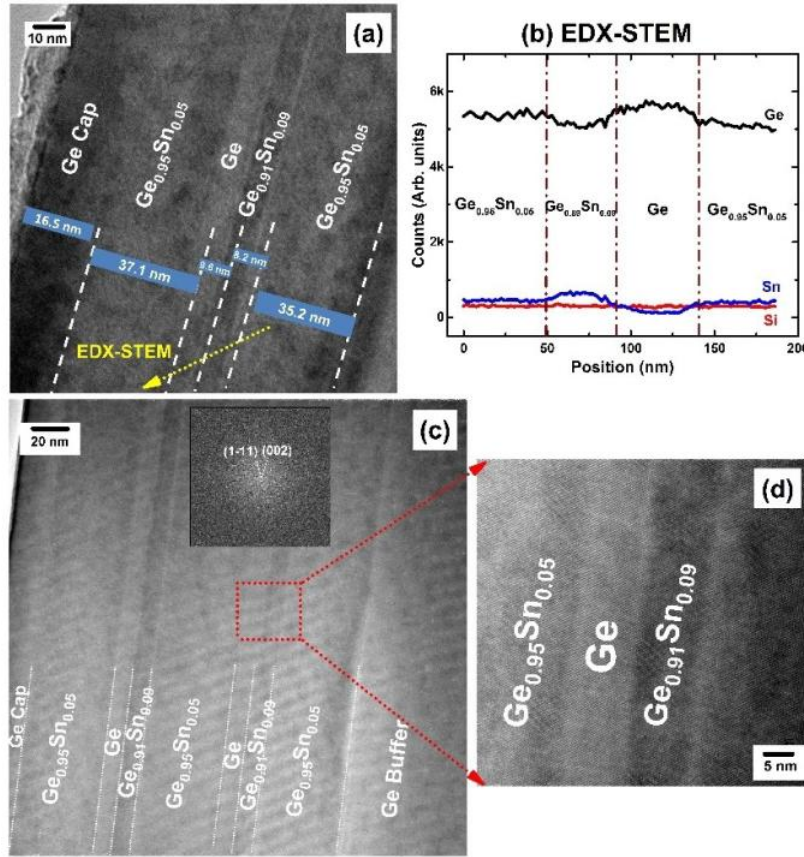


Figure 8.2 (a) Cross-sectional TEM image of Sample A and (b) EDX line scanning. (c) TEM image of Sample B. Inset: FTP. The smooth boundaries at the atomic level was highlighted in (d) zoomed-in TEM image.

The bright field TEM images are shown in Figure 8.2 (a) and (c) for samples A and B, respectively, which indicate a high crystalline quality without noticeable dislocation and stacking faults at the interfaces between each layer. Each epitaxy layer is well resolved. In Figure 8.2 (b), the energy-dispersive X-ray spectroscopy (EDX) line scan further confirms QW structure with sharp elemental boundaries. The smooth interfaces between each layer suggest the pseudomorphic growth for the QW structure. A 9.6-nm thick Ge interlayer was clearly observed between the GeSn well and barrier layers, whose role will be discussed in Section IV. In Figure 8.2 (c), two stacked single QWs are separated by a 40-nm thick  $\text{Ge}_{0.95}\text{Sn}_{0.05}$  barrier layer, partially for the purpose to

exam the machine controllability for the growth of such a complicated structure. The zoomed-in TEM image in Figure 8.2 (d) well identifies sharp interfaces between each layer at the atomic scale. Fourier transformed pattern (FTP), as shown in the insert of Figure 8.2 (c), shows a pseudo hexagonal symmetry reflecting cubic crystal structure. The TEM images shown in Figure 8.2 indicate that the defect-free complex GeSn QW structures could be successfully grown in a single run epitaxy process, which reflects the well-controlled growth capability at low-temperature using CVD reactor.

### 8.1.2. X-ray diffraction (XRD) analysis

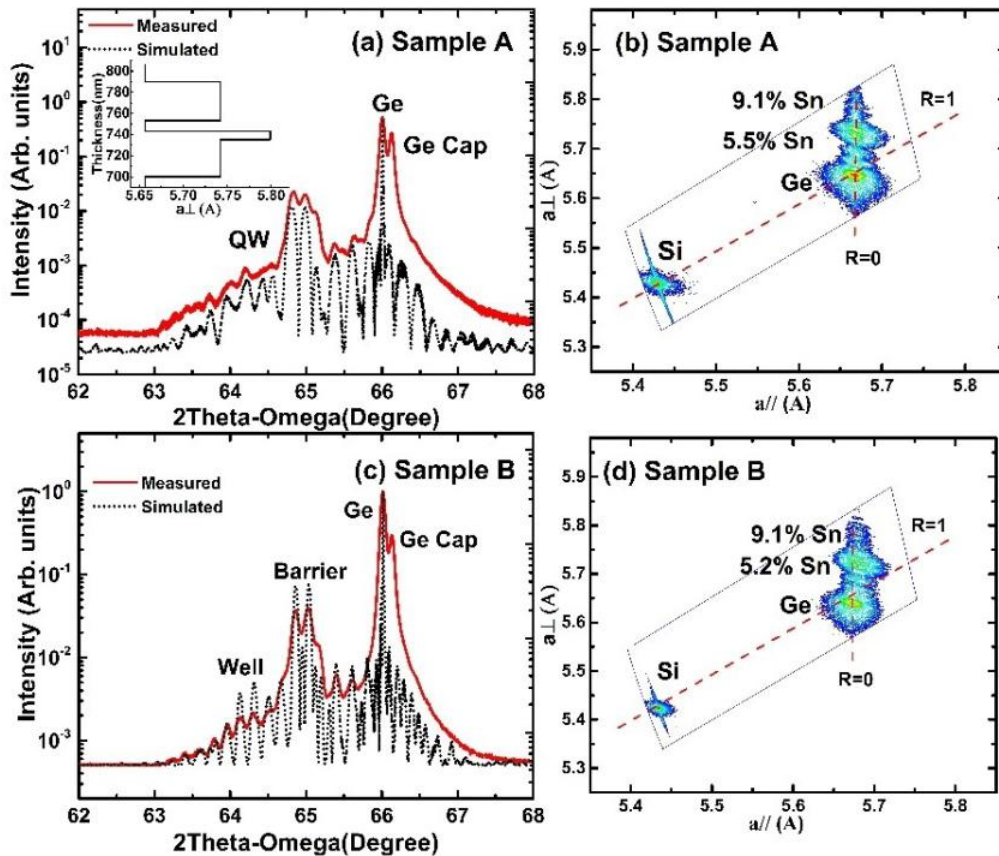


Figure 8.3 The XRD  $2\theta-\omega$  scan (black line) and the XRD simulation (red line) and RSM measurements were carried out on Sample A (a and b) and Sample B (c and d).

The Sn composition, strain value and thickness of each layer were investigated by high-resolution Phillips X'pert PRO XRD system. In Figure 8.3 (a), the black and red curves are measured data and simulated results of  $2\theta-\omega$  scan for sample A, respectively. The out-of-plane lattice constant and thickness for each layer of QW structure can be calculated by the simulated  $2\theta-\omega$  scan curve, as plotted in the insert of Figure 8.3 (a). The simulated thickness of each layer matches very well with TEM results. Figure 8.3 (b) shows the reciprocal space mapping (RSM) of sample A, which indicates that all the layers feature the same in-plane lattice constant with relaxed Ge buffer due to pseudomorphicity, corresponding to the vertical non-relaxation line ( $R=0$ ). The average in-plane lattice constant of each layer could be extracted from the peaks of RSM. Moreover, using elastic constants and bowing parameters of lattice constant in Appendix A, the residual compressive strain and composition for each layer were calculated.

Table 8.1 Summary of material characterization results for sample A.

Layer	Thickness (nm)	Sn (%)	Strain (%)
Ge Cap	16.5	0	0.01
Ge <sub>0.95</sub> Sn <sub>0.05</sub> Barrier	37.1	4.8	-0.84
Ge interlayer	9.6	0	0.01
Ge <sub>0.91</sub> Sn <sub>0.09</sub> Well	8.2	9.1	-1.39
Ge <sub>0.95</sub> Sn <sub>0.05</sub> Barrier	35.2	4.8	-0.84
Ge Buffer	700.0	0	0.01

Table 8.2 Summary of material characterization results for sample B.

Layer	Thickness (nm)	Sn (%)	Strain (%)
Ge Cap	16.5	0	0.01
Ge <sub>0.95</sub> Sn <sub>0.05</sub> Barrier	39.0	5.1	-0.79
Ge interlayer	9.0	0	0.01
Ge <sub>0.91</sub> Sn <sub>0.09</sub> Well	8.3	9.1	-1.35
Ge <sub>0.95</sub> Sn <sub>0.05</sub> Barrier	40.3	5.2	-0.79
Ge interlayer	9.5	0	0.01
Ge <sub>0.91</sub> Sn <sub>0.09</sub> Well	9.3	9.1	-1.35
Ge <sub>0.95</sub> Sn <sub>0.05</sub> Barrier	38.7	5.2	-0.79
Ge Buffer	700.0	0	0

The  $2\theta-\omega$  scan curve and RSM contour plot of sample B are shown in Figure 8.3 (c) and (d), respectively. Compared to sample A, more reflection fringe oscillations are shown in  $2\theta-\omega$  scan of

Sample B, suggesting that more layers with smooth interfaces are involved. The RSM of sample B shows the same pseudomorphic feature as sample A, as can be seen in Figure 8.3 (d). The material characterization results based on XRD analysis are summarized in Table 8.1 and 8.2.

### 8.1.3. Photoluminescence (PL) characterization

Temperature-dependent photoluminescence (PL) measurement was performed on both Sample A and B using a standard off-axis PL setup. A 532 nm continuous wave laser was utilized as a pumping source. The laser spot size was measured as 100  $\mu\text{m}$  in diameter and the pumping power was 500 mW. Samples were mounted in a helium-cooled cryostat and temperature was controlled from 10 to 300 K. Temperature-dependent PL spectra of sample A are shown in Figure 8.4 (a). Since each GeSn layer in QW structure experiences the compressive strain, the heavy hole (HH) and light hole (LH) bands in valance band (VB) are split with the maximum point of HH band is higher than that of LH band, resulting in the majority optical transitions occurring between the conduction band (CB) to the HH band. The PL spectra show a clear blue shift with decreasing temperature. The peak shift follows the typical Varshni's empirical expression which describes the temperature-dependence of the bandgap energy of semiconductors. At room temperature, two peaks can be observed: 1) The shorter wavelength peak at  $\sim 1950$  nm is attributed to the indirect bandgap transition in GeSn barrier that sandwiched between Ge interlayer and Ge cap, since the photo-generated carriers could be partially confined in GeSn barrier layer. This peak reduces rapidly with decreasing temperature as the emission from GeSn well dominates the PL at the temperatures from 300 to 150 K. 2) The longer wavelength peak located at  $\sim 2100$  nm corresponds to the direct bandgap transition in the GeSn well region, which agrees well with theoretical band structure calculation (which will be explained in section IV). As temperature decreases, the intensity of direct peak decreases, which is attributed to the reduced number of carriers populating



the direct  $\Gamma$  valley in conduction band. At 150 K, a PL peak at  $\sim 2150$  nm was observed, and the peak features monotonic increase at temperatures from 150 to 10 K. This peak is assigned to the indirect bandgap transition in the GeSn well region. This is because the decrease in non-radiative recombination at lower temperature leads to band filling in the indirect L valley in CB, resulting in the enhanced PL emission. Therefore at lower temperature, the indirect peak dominates the PL. Moreover, the line width of the peak is narrower at lower temperature, indicating the less emissions that are contributed from the defects. The temperature-dependent PL spectra of sample B are shown in Figure 8.4 (b). The PL characteristic is very similar to that of sample A. The optical transitions between the  $\Gamma$  (L) valley and the HH band can be observed. However, since the double QW structure complicates the transition mechanism, the corresponding PL peaks are overlapped and therefore they cannot be identified separately. The detailed PL study of GeSn DQW will be reported elsewhere. The features shown at longer wavelength ( $> 2200$  nm) at low temperature might be related to the defects. Further studies will be conducted to identify the defect characteristics.

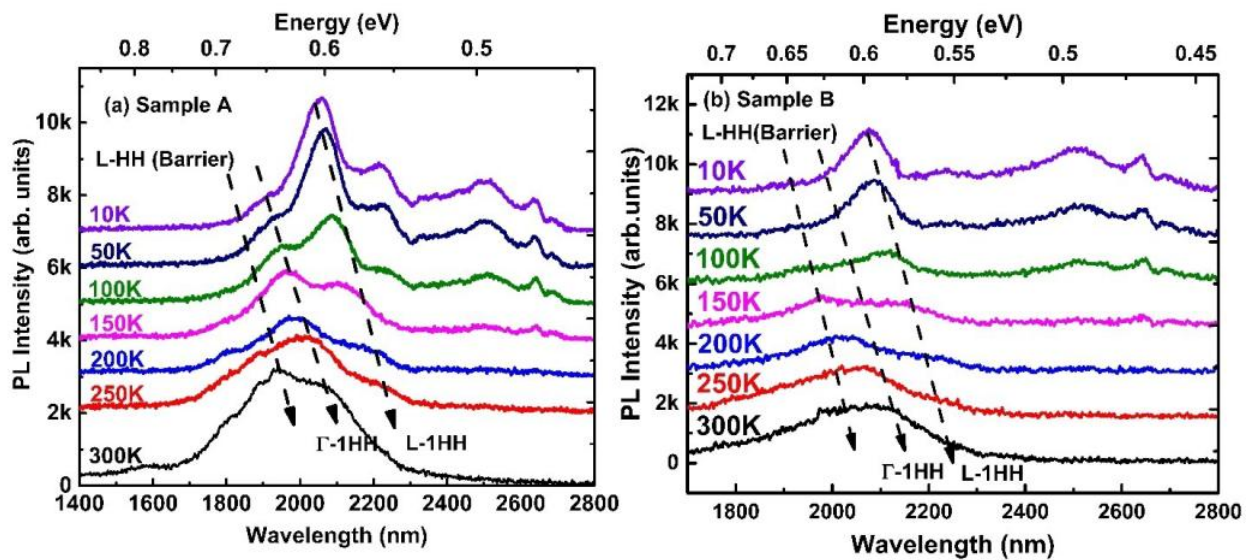


Figure 8.3 Temperature-dependent PL for (a) Sample A and (b) Sample B shows direct bandgap transition is dominant for both QWs at room temperature.



In order to further understand the PL characteristics, the electronic band structure and quantized energy levels of sample A were calculated using effective mass approximation and propagation matrix approach with the selected material parameters at room temperature. Parameters including the bandgap, deformation potential and effective masses of Si, Ge, and Sn were taken from Appendix A and valence band offset method discussed in Reference[127] was followed in our calculations. Four subbands was considered including  $\Gamma$  and L valleys in CB and heavy hole and light hole in VB, respectively. Figure 8.5 shows the band structure diagram of sample A. The bandgap energies of GeSn well and barrier were calculated suggesting that they both are indirect bandgap materials. For the  $\text{Ge}_{0.91}\text{Sn}_{0.09}$  well, the energy separation between  $\Gamma$  and L valley of 18 meV was obtained, which is smaller than thermal energy at room temperature ( $1 \text{ kT} \sim 26 \text{ meV}$ ). Such a small energy separation leads to the enhanced direct bandgap transition between  $\Gamma$  and 1HH (ground state of HH) band edge, resulting in the direct PL peak dominates the PL spectrum at 300 K. The band offset shows that the type-I band alignment is achieved, in which both electrons in the CB and holes in the VB are spatially confined in the GeSn well region. The barrier heights in CB are  $\Delta E_{c\Gamma} = 76 \text{ meV}$  and  $\Delta E_{cL} = 15 \text{ meV}$  at  $\Gamma$  and L valleys, respectively, indicating that the better electron confinement was obtained in  $\Gamma$  valley in comparison with L valley. The introduction of Ge interlayer provides larger barrier height of 152 meV in  $\text{Ge}_{0.91}\text{Sn}_{0.09}$  well-Ge interface compared to  $\text{Ge}_{0.91}\text{Sn}_{0.09}$  well-  $\text{Ge}_{0.95}\text{Sn}_{0.05}$  barrier interface (76 meV in  $\Gamma$  valley), which could affect the carrier confinement in  $\text{Ge}_{0.91}\text{Sn}_{0.09}$  well region as well as the carriers flowing towards the surface, and therefore affect the QW PL emission and the surface recombination. It is worth to point out that the insertion of Ge layer indicates the capability of optimizing the QW structure by using the well-developed growth method demonstrated in this work. The barrier heights in HH and LH bands were calculated as 36 and 5 meV, respectively. At lower temperature, due to the reduced

thermal energy, the improved carrier confinement at L valley in CB was obtained, resulting in the indirect peak dominating the PL at the temperatures lower than 150 K, as shown in Figure 8.4 (a). Table 8.3 summarizes the calculation results of band structures of sample A at room temperature. In the  $\text{Ge}_{0.91}\text{Sn}_{0.09}$  well region the quantized energy levels in CBs and VBs were calculated, as shown in Figure 8.5, which indicates the quantum effect.

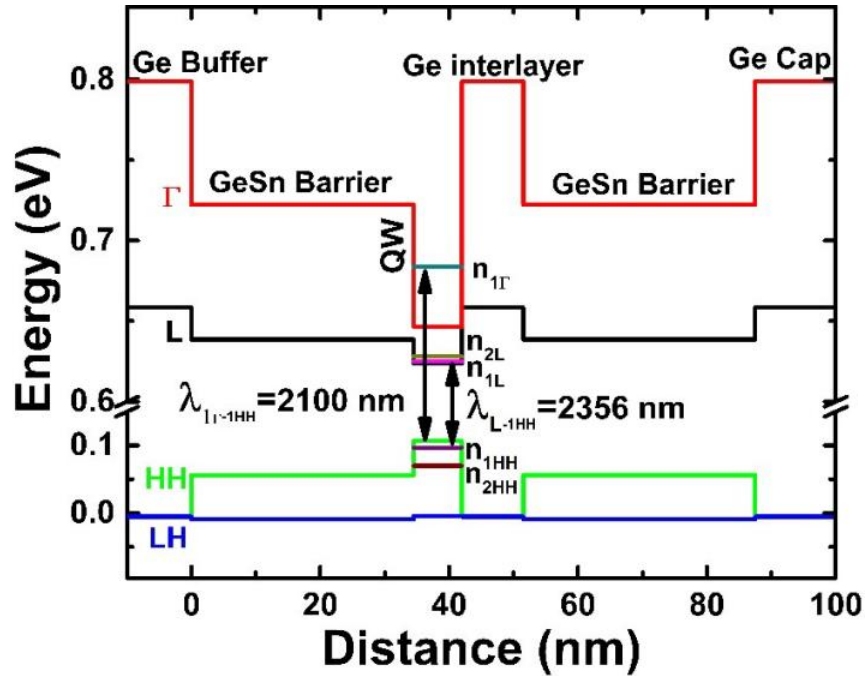


Figure 8.4 The calculated band structure of Sample A indicates type-I band alignment.

As a result, the HH and LH subbands become nonparabolic because of valance mixing effect while the CBs stay parabolic, which makes HH effective mass smaller than the bulk counterpart[93]. Furthermore, the compressive strain leads to split of HH and LH bands with the 113 meV of HH maximum higher than that of LH. Since HH becomes the dominate band for hole population, it favors the transverse electric mode of light emission. Moreover, the introduction of compressive strain reduces the hole effective mass at HH bands compared to the unstrained counterpart. Thus the population inversion condition could be achieved at relative low carrier injection level.

Table 8.3 The calculated band structure of Sample A

Sample A	$\Delta E_{c\Gamma}$ (meV)	$\Delta E_{cL}$ (meV)	$\Delta E_{vHH}$ (meV)	$\Delta E_{vLH}$ (meV)	$\Delta E_{1\Gamma-1HH}$ (meV)	$\Delta E_{1L-1HH}$ (meV)	$\Delta E_g = E_{g\Gamma} - E_{gL}$ (meV)
Value	76	15	36	5	590	527	18

#### 8.1.4. Discussion of optical properties of QW

In order to deeply understand the optical transition mechanism of Sample A, the electron occupation ratio between  $\Gamma$  and L valley and lifetime of Shockley-Read-Hall (SRH) process were calculated, as shown in Figure 8.6. Single electron-temperature electron transferring model was utilized to calculate electron occupation between conduction valleys[128]. The lifetime of SRH was estimated using the following equation[129],

$$\tau_{SRH} = \tau_{n0} \left[ 1 + \cosh\left(\frac{E_T - E_F}{kT}\right) \right] \quad \text{Equation 8.1}$$

where  $E_T$  is trap energy level and  $E_F$  is intrinsic Fermi level. The constant  $\tau_{n0}$  is estimated using Ge parameters.

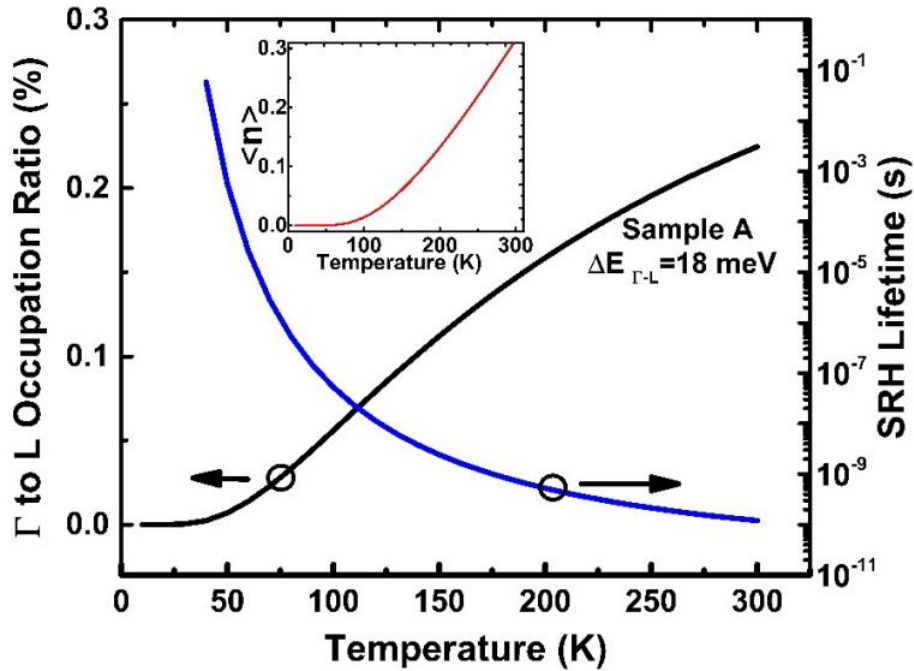


Figure 8.5 The electron occupation ratio between  $\Gamma$  and L valley, lifetime of SRH process and statistical number of phonons (insert) verse temperature.

As observed in the PL measurements, the direct bandgap transition is dominant at room temperature despite the indirect bandgap nature of  $\text{Ge}_{0.91}\text{Sn}_{0.09}$  well. This can be explained as following: Since the energy separation between  $\Gamma$  and L valley is small (less than 1 kT) at room temperature, a large number of electrons at L valley could gain sufficient thermal energy and leap into  $\Gamma$  valley. As a result, 0.22% of carriers populates the  $\Gamma$  valley. Considering the relative high recombination rate of direct bandgap, the enhanced light emission from direct bandgap is obtained. As temperature decreases, the electrons occupation ratio between  $\Gamma$  and L valley decreases, resulting in the decreased direct peak intensity. On the other hand, at the temperature below 150 K, most non-radiative trap states within bandgap are frozen and the lifetime of SRH recombination is dramatically increased, therefore the indirect bandgap transition dominates the PL at lower temperature. At the temperatures between 150 and 50 K, the considerable number of phonon may be responsible for the phonon-assisted emission of indirect bandgap. At temperature below 50 K, the indirect bandgap emission may be mainly supported by no-phonon (NP)-assisted recombination process of free excitons[130].

According to the band structure calculation, the barrier heights offered by  $\text{Ge}_{0.95}\text{Sn}_{0.05}$  barriers are insufficient in both CB and VB. From the QW design perspective, it is desirable to have a barrier layer with separate tuning of bandgap and lattice constant. Based on our theoretical study, the ternary alloy SiGeSn could be the ideal candidate for the barrier layer. By tuning the incorporations of Si and Sn into Ge, the lattice and bandgap energy of SiGeSn alloy can be engineered separately. We have grown SiGeSn/GeSn/SiGeSn QWs with different Si and Sn compositions using the same CVD growth method. The detailed characterization results will be reported elsewhere.

## 8.2. Optimized GeSn/GeSn/GeSn QW structure

While the GeSn/GeSn/GeSn QW shows the promising optical performance, the Ge interlayer between barrier and well region was unintentionally introduced. The Ge interlayer features the indirect energy bandgap, prohibiting the realization of type-I quantum well structure. The introduction of Ge interlayer also complicates the QW structure and blocks carrier transportation from barrier to well region. The physics mechanism underlying the formation of Ge interlayer was firstly explored in order to eliminate unintentional Ge layer. Based on the previous discussion of spontaneous-relaxation-enhanced (SRE) mechanism[104], the built-in compressive strain in QW was proposed to be responsible for the formation of Ge interlayer. Since the Sn atoms exhibit larger radius and lower free energy than Ge atoms, the Sn atoms tend to escape the high-compressive-strain zone[44]. If the accumulated elastic strain energy reaches the threshold, the Sn atoms in Ge lattice sites would be driven away, leaving the pure Ge in lattice sites. The excess Sn will float on the surface or evaporate off the surface.

### 8.2.1. Strain balanced growth of QW

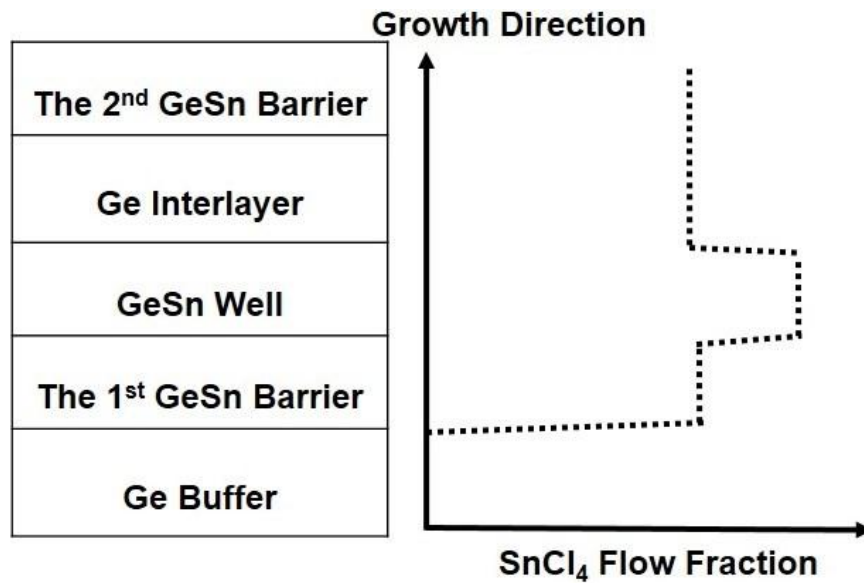


Figure 8.6 The schematic diagram of QW structure and the change of SnCl<sub>4</sub> flow fraction during the CVD epitaxy process of QW structure.

The schematic diagram of QW structure and change of Sn flow fraction during the growth were drawn in Figure 8.7 in order to explain the formation of unintentional Ge layer. The overall GeSn QW structure was pseudomorphically grown on Ge buffer. Therefore, the highly compressive strain remains in the QW, which inhibits the Sn incorporation into both barrier and well region. After the Ge buffer growth, SnCl<sub>4</sub> was delivered into the reactor chamber with GeH<sub>4</sub> and carrier gas to start the 1<sup>st</sup> GeSn barrier epitaxy. Under the SnCl<sub>4</sub> oversaturation condition, Sn atoms are forced to incorporation into the Ge lattice sites. The Sn incorporation is balanced by the competition between pressure oversaturation of SnCl<sub>4</sub> and compressive strain. Meanwhile, the compressive strain accumulates during the growth of the 1<sup>st</sup> GeSn barrier because of the pseudomorphic epitaxy. The growth of GeSn well region was initiated by increasing the SnCl<sub>4</sub> flow fraction compared with the 1<sup>st</sup> barrier. Although the more compressive strain builds up during the epitaxy, more Sn atoms are pushed into Ge lattice matrix with a higher supersaturated pressure of SnCl<sub>4</sub>, forming a higher Sn-content thin GeSn layer as the well region of QW. A new growth equilibrium was reached during the epitaxy of GeSn well region. After the growth of well region, the compressive strain remains high. In order to grow the 2<sup>nd</sup> GeSn barrier, the SnCl<sub>4</sub> flow fraction was reduced after GeSn well epitaxy, resulting in the decrease of SnCl<sub>4</sub> supersaturated pressure. Therefore, the balance between Sn oversaturation condition and compressive strain was broken. The large compressive strain in high Sn-content GeSn well repels the subsequent Sn incorporation at the onset of the 2<sup>nd</sup> barrier growth. As a result, the pure Ge interlayer was formed after GeSn well layer. Then a new growth equilibrium begins to build up. Sn atoms start to incorporate into Ge lattice sites. The final Sn incorporation remains constant after the epitaxy balance between SnCl<sub>4</sub> oversaturated pressure and compressive strain is achieved. The 2<sup>nd</sup> GeSn barrier was then grown on top of Ge interlayer.

Table 8.4 Design of Sample structures after RP-CVD growth in order to remove the Ge interlayer of GeSn QW.

Sample	Buffer Sn (%)	Ge(Sn) Interlayer		Barrier		Well	
		Sn (%)	Thickness (nm)	Sn (%)	Strain (%)	Sn (%)	Strain (%)
A	0	<b>0</b>	<b>9.6</b>	4.8/4.8	-0.84/-0.84	9.1	-1.39
B	7.1	<b>0</b>	<b>4.8</b>	5.6 / 4.8	0.22/0.34	9.4	-0.33
C	8.5	<b>3.5</b>	<b>7.2</b>	8.5 / 7.3	0/0.17	13.7	-0.75
D	9.7			9.7 / 11.2	0/-0.22	15.5	-0.83

In order to ease the compressive strain in QW structure and eliminate the Ge interlayer, strain-balanced QW was investigated by using GeSn with variable Sn content as a buffer instead of Ge[131]. After the Ge buffer on Si the thick GeSn layer was further grown on Ge as the second buffer layer. The GeSn buffer layer undergoes small compressive strain with high material quality. The compressive strain in QW could be tuned by changing the Sn composition at the GeSn buffer layer. Table 8.4 summarized the design of QW structures in order to remove the Ge interlayer. For Sample A the Ge buffer was adopted while for sample B, C, and D GeSn buffers with different Sn compositions were exploited.

### 8.2.2. Secondary ion mass spectrometry (SIMS) analysis

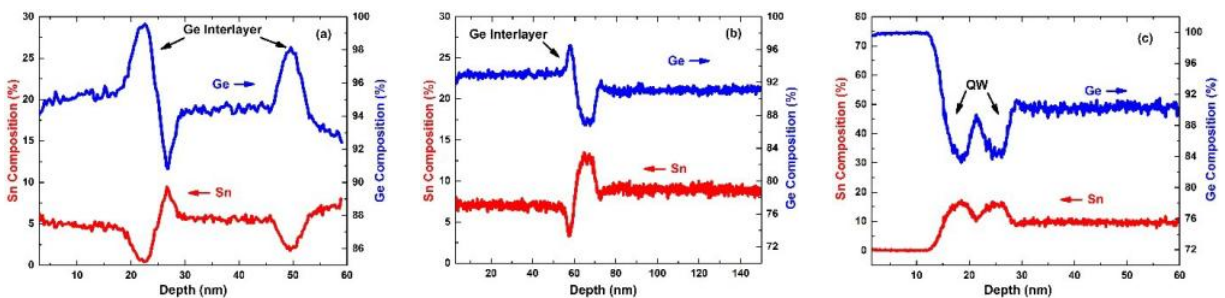


Figure 8.7 The SIMS profiles of sample B, C, and D were shown in (a), (b), and (c), respectively. The Ge interlayer was removed gradually from sample B to D.

Figure 8.8 shows the SIMS profiles of QW structures for sample B, C, D for comparison. Sample A is the pseudomorphic QW which was grown on the Ge buffer. Therefore, the high compressive strain accumulated in the QW structure. The compressive strain in the barriers and well region is

-0.84% and -1.39%, respectively. As a result, the unintentional Ge layer is 9.6 nm. Combining with Table 8.4 and Figure 8.8, the QW of sample B was grown on GeSn buffer with 7.1 % Sn content. In this case, the barriers of QW was under tensile strain of 0.22% and 0.34% while the well region is under compressive strain of -0.33% which is 76% less of the strain in well region of sample A. As a result, the Ge interlayer is narrowed down to 4.8 nm, half of the thickness of sample A. For sample C, the GeSn layer with 8.5% Sn content was used as the buffer. At the same time, the GeSn buffer acts as one of the barrier and the other barrier is on the top of well region with 7.3% Sn content. The Sn incorporation in well region increases up to 13.7% and the compressive strain in well region is -0.75%. The GeSn interlayer with 3.5% Sn content instead of the Ge interlayer forms between the barrier and well region. The corresponding thickness is 7.2 nm. The double QW structure of Sample D was grown on GeSn buffer with 9.7% Sn content. The GeSn buffer acts as one of the barriers as well. From the SIMS of sample D, the Ge interlayer was totally eliminated in QW, indicating that the GeSn buffer layer effectively eases the compressive strain. The Sn incorporation in well region reaches up to 15.5% with compressive strain of -0.83%. The Ge cap layer with the thickness of 13 nm was grown on top of well region. The final remedy of unintentional interlayer of sample D justifies the effectiveness of compressive strain on the interlayer formation. It also shows that by applying the GeSn buffer layer the compressive strain could be reduced. The Sn incorporation in well region increases as well via tuning the compressive strain.



### 8.2.3. PL measurement

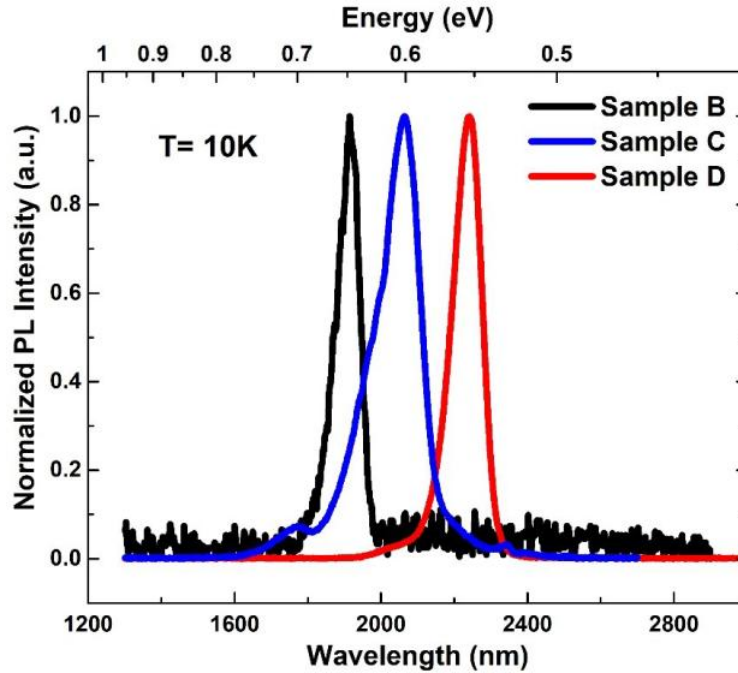


Figure 8.8 The comparison of PL spectra of sample B, C, and D at the temperature of 10 K.

By introducing the GeSn buffer, the compressive strain in QW structure was mitigated, leading to the increase of Sn incorporation for both barrier and well region. Meanwhile, the decrease of compressive strain increases the directness of energy bandgap and the true type I direct bandgap QW of GeSn could be realized. The PL spectra of sample B, C, and D at the temperature of 10 K were performed for comparison, as shown in Figure 8.9. Since the PL was conducted at the temperature of 10 K, the majority of carriers are condensed in well region. Therefore, the PL spectra in Figure 8.9 represent the light emission from well regions. The Sn incorporations of GeSn buffer for sample B, C, and D are 7.1%, 8.5%, and 9.7%, respectively. As a result, the Sn incorporations of GeSn well region for sample B, C, and D are 9.4%, 13.7%, and 15.5%, respectively. The increase of Sn incorporation from sample B to D results from the reduced compressive strains in QWs by increasing the Sn contents of GeSn buffers. On the PL spectra, a red peak shift was observed from sample B to D. The PL peaks of sample B, C, and D are 1914

nm (0.648 eV), 2066 nm (0.6 eV) and 2242 nm (0.553 eV), respectively. The red shift of PL spectra from B to D is due to the increase of Sn contents in well regions of QWs.

#### 8.2.4. Band diagram calculation

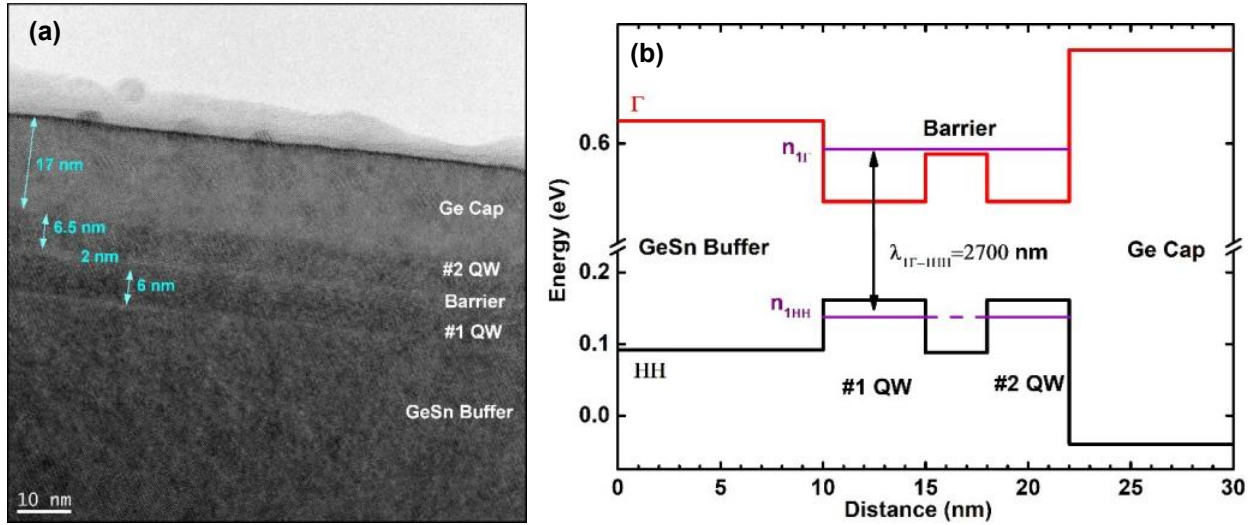


Figure 8.9 (a) The bright field TEM image of sample D. (b) The band diagram of QW structure of sample D, showing the type-I band alignment of QW.

The cross sectional TEM imaging of sample D was performed, as shown in Figure 8.10 (a). Each layer of QW structure on top of GeSn buffer was resolved with sharp interfaces. The thicknesses of QWs are 6 and 6.5 nm, sandwiching a narrow barrier layer with the thickness of 2 nm. The Ge cap was measured as 17 nm. From the TEM imaging, no unintentional interlayer was observed between barrier and well region of QW, furthering confirming the remedy of interlayer due to the decrease of compressive strain by adopting the GeSn buffer. The band diagram of QW structure at the temperature of 300 K was calculated using the effective mass approximation and propagation matrix approach[93], which was shown in Figure 8.10 (b). The bowing parameters of direct ( $\Gamma$  valley) and indirect (L valley) bandgap energy was chosen as  $b_{\Gamma}=1.95$  eV and  $b_L=0.68$  eV, respectively. The  $\Gamma$  valley of conduction band and the heavy hole (HH) of valence band were drawn in the band diagram. The type-I band alignment was clearly revealed for QW structure of sample D, which is advantageous for optoelectronics applications. The first quantized energy

levels in the well region  $n_{1\Gamma}$  and  $n_{1HH}$  were drawn in the diagram. The  $n_{1\Gamma}$  and  $n_{1HH}$  lie 26 meV above the  $\Gamma$ -valley band and 24 meV below the HH band, respectively. The interband transition between  $n_{1\Gamma}$  and  $n_{1HH}$  was calculated as 2700 nm (0.459 eV) at room temperature (300 K).

## **Chapter 9. Summary and Future work**

### **9.1. Summary**

For customer-designed UHV-CVD system, the low/high temperature two-step Ge on Si substrate was firstly investigated in order to explore the CVD machine ability. The Ge on Si could also be used as a buffer of GeSn growth. After the Ge growth, the thicknesses were measured by Ellipsometry and the activation energy of epitaxy was extracted as  $E_a=1.07$  eV. The 972 nm Thick Ge buffer with smooth surface and high quality was eventually obtained. The PL measurements exhibits the good optical properties of Ge layer. The etch pit method determines the good crystal properties of Ge with average threading dislocation density of  $1.94 \times 10^7 \text{ cm}^{-2}$ . High quality of Ge with low surface roughness acts as a buffer layer for the subsequent GeSn growth. Hot-filament assisted CVD growth of Ge was also investigated. With the help of hot filament, the thick Ge sample as well as high quality could be achieved, which is a benchmark of the future GeSn growth. Plasma enhanced CVD growth of GeSn on Si substrate was conducted in order to testify the machine ability for GeSn epitaxy with plasma. The GeSn was successfully grown on Si substrate. However, the overall GeSn on Si wafer is not uniform because of the different of decomposition energy between  $\text{SnCl}_4$  and  $\text{GeH}_4$ . The thickest GeSn as 1154 nm was obtained at the edge of the wafer. The corresponding Sn composition was achieved as 6.2%. GeSn growth on Ge buffer by the standard UHV-CVD was also explored. The  $\text{SnCl}_4$  was proven to have an important effect on the quality of GeSn material. High quality of GeSn with mirror-like surface was achieved when decreasing the  $\text{SnCl}_4$  flow fraction down to  $1.4 \times 10^{-4}$ , which is the minimum limitation of mass

flow controllers. With the minimum SnCl<sub>4</sub> flow fraction, the highest Sn incorporation was 8.1% at the temperature of 250°C, corresponding to the wavelength of light emission as 2080 nm at room temperature which was verified by PL measurements.

For commercial RP-CVD system, the main goal is to obtain the high quality, high Sn incorporation thick GeSn film. To serve this purpose, two growth strategies were investigated to analyze strain relaxation, high Sn incorporation, and their relationship. Compressive strain has a strong effect on Sn incorporation, which is well explained by Gibbs free energy calculation including elastic strain energy. The gradual strain relaxation results in spontaneous formation of gradient GeSn. Step graded GeSn structure relaxes compressive strain more smoothly and the final Sn incorporation of 22.3% was achieved, which is unprecedented so far for CVD technology. Different dislocation arrangements are revealed at GeSn/Ge interface. The mixed type 60° dislocations are dominant at the interface over Lomer dislocations. Intrinsic stacking faults are associated with two different reactions: 60° dislocation dissociation and Lomer dislocation formation. Beyond critical thickness half loops of 60° dislocations are nucleated and expanded outwards as threading dislocations. Spontaneous gradient GeSn helps terminating threading dislocations by the Hagen-Strunk multiplication. The well-ordered dislocation network was formed at gradient layer, leading to the low-defect GeSn on the top. This work provides the thorough analysis of strain relaxation mechanism of GeSn and offers an essential guidance for low defect GeSn growth with high Sn content.

The recent progress of group IV GeSn laser has opened up a complete new route towards the efficient laser source for monolithic integration of Si photonics. The GeSn laser with high Sn content is highly desirable to cover mid-infrared wavelength. This work demonstrated optically pumped edge-emitting GeSn lasers with the maximum Sn content of 22.3%. The whole device

structures were Sn compositional graded, leading to the gradual narrowing of band edge along growth direction. Using the 1064 nm pumping laser with the duty cycle of 0.027%, the first batch of GeSn lasing device with 5  $\mu\text{m}$  width and 1.25 mm length achieves up to 150 K lasing temperature. The 77 K lasing threshold was measured as low as 168  $\text{kW}/\text{cm}^2$  and lasing characteristic temperature was extracted as 70 K. The longest lasing wavelength was achieved as 3000 nm. For the second batch of GeSn lasing devices, the larger lasing devices with 20  $\mu\text{m}$  width and 2.6 mm length were used. The duty cycle of the 1064 nm pumping laser was changed to 0.003%. The decrease of duty cycle of pumping laser helps suppress the local heating effects introduced by pumping laser. As a result, the operating temperature increases up to 240 K and the corresponding lasing wavelength is 3266 nm. For the third batch of GeSn laser devices, the lasing device with 100  $\mu\text{m}$  width and 2.9 mm length was employed. The 1950 nm laser was used as the optically pumping source. The local heating effects induced by the pumping laser were significantly reduced. As a result, the near room temperature GeSn laser was achieved. The maximum operating temperature is up to 270 K, which is the world record lasing performance of GeSn lasing devices. The longest lasing wavelength is extended up to 3442 nm. The excellent GeSn lasing achievement in this work with high Sn composition is an essential path towards Si-based laser with high performance and board coverage of mid infrared wavelength range.

The more advanced GeSn structure of quantum well was also investigated. For the first batch of QW samples, The  $\text{Ge}_{0.95}\text{Sn}_{0.05}/\text{Ge}_{0.91}\text{Sn}_{0.09}/\text{Ge}_{0.95}\text{Sn}_{0.05}$  single QW and double QWs were pseudomorphically grown using industry standard RPCVD reactor in a single run epitaxy process. Atomic-scale high resolution TEM and Fourier transform pattern revealed high crystalline quality of QW samples, which also reflected the capability of complex structure growth using CVD at low temperature. An unintentional Ge interlayer was observed between well and barrier regions. The

thicknesses, compositions and strain values for each layer were measured by XRD. The temperature-dependent PL spectra showed that the direct and indirect bandgap transitions dominate the PL at high and low temperatures, respectively. Theoretical calculation of band structure at room temperature showed that the type-I band alignment was achieved. In order to get rid of the unintentional Ge interlayer and achieve high Sn incorporation at the well region, the strain-balanced GeSn/GeSn structure was grown on the variable Sn-content GeSn buffer. The Ge interlayer was eventually eliminated by introducing GeSn buffer with Sn incorporation as high as 9.7%. As a result, the highest Sn incorporation in well region was achieved as 15.5% and the corresponding light emission at 10 K was obtained as 2242 nm which was confirmed by PL measurements.

For the second batch of GeSn QW samples, the Ge interlayer was eliminated by introducing the GeSn buffer layer with variable Sn incorporations. The compressive strain was firstly proposed to be responsible for the formation of Ge interlayer. During the QW epitaxy, the accumulated compressive strain in the well region drives away the Sn atoms from the subsequent GeSn barrier. To ease the strain effects on Sn incorporation, the thick GeSn buffer layer was firstly grown. Then GeSn/GeSn/GeSn single and double QWs were grown on top of GeSn buffer. The compressive strain of QWs could be tuned by varying the Sn content of GeSn buffer. The Ge interlayer of QW samples was removed gradually by increasing the Sn content of GeSn buffer, which was verified by the SIMS profiles. Meanwhile, the Sn incorporation in well region increases, resulting in the direct bandgap characteristics. After the remedy of Ge interlayer, the GeSn/GeSn/GeSn QW structure was demonstrated as the true type-I structure by band diagram calculation, which is advantageous for the optoelectronic devices.

## 9.2. Future work

### 1. GeSn growth on Ge buffer by UHV-CVD

For GeSn growth on Ge, the flow fraction of SnCl<sub>4</sub> has been proven to be critical to obtain the high quality GeSn film with smooth surface. The current flow fraction range for SnCl<sub>4</sub> is 10<sup>-2</sup> – 10<sup>-4</sup>. The flow fraction with 10<sup>-4</sup> order of magnitude enables the effective Sn incorporation at low temperature while maintaining the good material quality. More Sn incorporation could be achieved by further lowering the growth temperature and the flow fraction of SnCl<sub>4</sub>, which is difficult for the current growth condition due to the minimum limitation of mass flow controller. The new gas mixing system was developed successfully in order to extend the flow fraction range of SnCl<sub>4</sub> lower than the current minimum of 10<sup>-4</sup>. Before the CVD growth, all the precursors such as GeH<sub>4</sub>, SnCl<sub>4</sub>, and Ar were delivered into the cylindrical bottle. The molar fraction of precursors could be accurately monitored by Residual Gas Analyzer (RGA). The motor-driven agitator inside the gas bottle assures the uniform mixture of precursors. By employing the gas mixing system the wide range of flow fraction of SnCl<sub>4</sub> could be achieved. High quality GeSn with high Sn incorporation is supposed to be grown by UHV-CVD with gas mixing system.

### 2. Plasma enhanced CVD growth of GeSn

The plasma enhanced CVD growth has been proven to be an efficient method to grow thick GeSn layer on Si substrate. However, due to the huge lattice mismatch between GeSn and Si, large amounts of misfit dislocations were introduced, deteriorating the material quality of GeSn. In addition, the compressive strain limits Sn incorporation. The next growth plan is to grow GeSn on Ge buffer by Plasma enhanced CVD technique in order to accommodate the lattice mismatch between GeSn and Si. Through easing the compressive strain, high quality GeSn layer with high Sn incorporation could be grown. One issue of plasma enhanced CVD growth is the uniformity of

GeSn on the Si wafer due to the difference of decomposition rate between  $\text{SnCl}_4$  and  $\text{GeH}_4$  in plasma. GeSn could only be grown successfully on the edge of wafer. At the center of wafer, pure Ge layer was grown. To address this issue, one method is to reduce the RF power of plasma to ease the discrepancy of decomposition rate of precursors. Another possible solution is to update the gas feeding system into the reactor. The current gas inlet is parallel to the surface of substrate, resulting in the non-uniform deposition of GeSn across the wafer. The showerhead design of gas precursors facing to the wafer could assure the homogenous distribution of gases. Therefore, the uniform GeSn deposition could be improved for plasma enhanced CVD growth.

### 3. High performance GeSn laser

While the optically pumped GeSn lasing devices have shown the bright prospect towards the room temperature laser, the lower threshold density of lasing, continuous wavelength lasing and high power output are the next tasks to achieve the commercialized GeSn laser devices. There are three potential solutions to reach these goals: 1) pursuing high quality of GeSn. Small amounts of dislocations will reduce the carrier loss and thus lower threshold density. 2) Higher Sn composition. More Sn contents could increase the directness of GeSn material, leading to more efficient light emission. 3) More advanced device structure such as heterostructure or quantum well. The more advanced structure will assure better carrier and optical confinement and thus higher lasing performance. The electrically pumped GeSn laser devices is the next step for the commercialized group IV laser which could be monolithically integrated on Si substrate.



## References

- [1] R. S.-I. J. of selected topics in quantum electronics and undefined 2006, “The past, present, and future of silicon photonics,” *ieeexplore.ieee.org*.
- [2] A. E.-J. Lim, Junfeng Song, Qing Fang, Chao Li, Xiaoguang Tu, Ning Duan, Kok Kiong Chen, R. P.-C. Tern, and Tsung-Yang Liow, “Review of Silicon Photonics Foundry Efforts,” *IEEE J. Sel. Top. Quantum Electron.*, vol. 20, no. 4, pp. 405–416, Jul. 2014.
- [3] B. Jalali and S. Fathpour, “Silicon Photonics,” *J. Light. Technol. Vol. 24, Issue 12, pp. 4600-4615*, vol. 24, no. 12, pp. 4600–4615, Dec. 2006.
- [4] S. Wirths, D. Buca, ... S. M. C. G. and C. of, and undefined 2016, “Si–Ge–Sn alloys: From growth to applications,” *Elsevier*.
- [5] G. T. Reed, *Silicon photonics : the state of the art*. Wiley, 2008.
- [6] M. Asghari and A. V. Krishnamoorthy, “Silicon photonics: Energy-efficient communication,” *Nat. Photonics*, vol. 5, no. 5, pp. 268–270, May 2011.
- [7] G. T. Reed and A. P. Knights, *Silicon photonics: an introduction*. John Wiley, 2004.
- [8] R. Soref, D. Buca, and S.-Q. Yu, “Group IV Photonics: Driving Integrated Optoelectronics,” *Opt. Photonics News*, vol. 27, no. 1, p. 32, Jan. 2016.
- [9] Z. Wang, B. Tian, M. Pantouvaki, W. Guo, P. Absil, J. Van Campenhout, C. Merckling, and D. Van Thourhout, “Room-temperature InP distributed feedback laser array directly grown on silicon,” *Nat. Photonics*, vol. 9, no. 12, pp. 837–842, 2015.
- [10] D. Liang and J. E. Bowers, “Recent progress in lasers on silicon,” *Nat. Photonics*, vol. 4, no. 8, pp. 511–517, Aug. 2010.
- [11] K. Tanabe, K. Watanabe, and Y. Arakawa, “III-V/Si hybrid photonic devices by direct fusion bonding,” *Sci. Rep.*, vol. 2, no. 1, p. 349, Dec. 2012.
- [12] H. Rong, R. Jones, A. Liu, O. Cohen, D. Hak, A. Fang, and M. Paniccia, “A continuous-wave Raman silicon laser,” *Nature*, vol. 433, no. 7027, pp. 725–728, Feb. 2005.
- [13] H. Rong, A. Liu, R. Jones, O. Cohen, D. Hak, R. Nicolaescu, A. Fang, and M. Paniccia, “An all-silicon Raman laser,” *Nature*, vol. 433, no. 7023, pp. 292–294, Jan. 2005.
- [14] T. Kippenberg, J. Kalkman, A. Polman, K. V.-P. R. A, and undefined 2006, “Demonstration of an erbium-doped microdisk laser on a silicon chip,” *APS*.
- [15] J. Liu, X. Sun, R. Camacho-Aguilera, L. C. Kimerling, and J. Michel, “Ge-on-Si laser operating at room temperature,” *Opt. Lett.*, vol. 35, no. 5, p. 679, Mar. 2010.
- [16] J. Liu, X. Sun, L. C. Kimerling, and J. Michel, “Direct-gap optical gain of Ge on Si at room

- temperature,” *Opt. Lett.*, vol. 34, no. 11, p. 1738, Jun. 2009.
- [17] R. E. Camacho-Aguilera, Y. Cai, N. Patel, J. T. Bessette, M. Romagnoli, L. C. Kimerling, and J. Michel, “An electrically pumped germanium laser,” *Opt. Express*, vol. 20, no. 10, p. 11316, May 2012.
- [18] R. S.-N. photonics and undefined 2010, “Mid-infrared photonics in silicon and germanium,” *nature.com*.
- [19] K. P. Homewood and M. A. Lourenço, “The rise of the GeSn laser,” *Nat. Photonics*, vol. 9, no. 2, pp. 78–79, Feb. 2015.
- [20] W. Du, S. A. Ghetmiri, B. R. Conley, A. Mosleh, A. Nazzal, R. A. Soref, G. Sun, J. Tolle, J. Margetis, H. A. Naseem, and S.-Q. Yu, “Competition of optical transitions between direct and indirect bandgaps in  $\text{Ge}_{1-x}\text{Sn}_x$ ,” *Appl. Phys. Lett.*, vol. 105, no. 5, p. 051104, Aug. 2014.
- [21] S. A. Ghetmiri, W. Du, J. Margetis, A. Mosleh, L. Cousar, B. R. Conley, L. Domulevicz, A. Nazzal, G. Sun, R. A. Soref, J. Tolle, B. Li, H. A. Naseem, and S.-Q. Yu, “Direct-bandgap GeSn grown on silicon with 2230 nm photoluminescence,” *Appl. Phys. Lett.*, vol. 105, no. 15, p. 151109, Oct. 2014.
- [22] C. D. Thurmond, F. A. Trumbore, and M. Kowalchik, “Germanium Solidus Curves,” *J. Chem. Phys. J. Appl. Phys. Appl. Phys. Lett.*, vol. 25, no. 81, 1956.
- [23] T. Tsukamoto, N. Hirose, A. Kasamatsu, T. Mimura, T. Matsui, and Y. Suda, “Investigation of Sn surface segregation during GeSn epitaxial growth by Auger electron spectroscopy and energy dispersive x-ray spectroscopy,” *Appl. Phys. Lett.*, vol. 106, no. 5, p. 052103, Feb. 2015.
- [24] E. Kasper, J. Werner, M. Oehme, S. Escoubas, N. Burle, and J. Schulze, “Growth of silicon based germanium tin alloys,” *Thin Solid Films*, vol. 520, no. 8, pp. 3195–3200, Feb. 2012.
- [25] M. Oehme, K. Kosteki, M. Schmid, F. Oliveira, E. Kasper, and J. Schulze, “Epitaxial growth of strained and unstrained GeSn alloys up to 25% Sn,” *Thin Solid Films*, vol. 557, pp. 169–172, Apr. 2014.
- [26] J. Piao and Jie, “Molecular Beam Epitaxial Growth and Characterization of the Modulated Structures for Detector Applications.,” *Thesis (PH.D.)--COLUMBIA Univ. 1991.Source Diss. Abstr. Int. Vol. 52-08, Sect. B, page 4288.*, 1991.
- [27] E. A. Fitzgerald, P. E. Freeland, M. T. Asom, W. P. Lowe, R. A. Macharrie, B. E. Weir, A. R. Kortan, F. A. Thiel, Y.-H. Xie, A. M. Sergent, S. L. Cooper, G. A. Thomas, and L. C. Kimerling, “Epitaxially stabilized  $\text{Ge}_x\text{Sn}_{1-x}$  diamond cubic alloys,” *J. Electron. Mater.*, vol. 20, no. 6, pp. 489–501, Jun. 1991.
- [28] M. T. Asom, E. A. Fitzgerald, A. R. Kortan, B. Spear, and L. C. Kimerling, “Epitaxial growth of metastable SnGe alloys,” *Appl. Phys. Lett.*, vol. 55, no. 6, pp. 578–579, Aug. 1989.

- [29] M. Nakamura, Y. Shimura, S. Takeuchi, O. Nakatsuka, and S. Zaima, "Growth of  $\text{Ge}_{1-x}\text{Sn}_x$  heteroepitaxial layers with very high Sn contents on InP(001) substrates," *Thin Solid Films*, vol. 520, no. 8, pp. 3201–3205, Feb. 2012.
- [30] W. Wegscheider, J. Olajos, U. Menczigar, W. Dondl, and G. Abstreiter, "Fabrication and properties of epitaxially stabilized Ge /  $\alpha$ -Sn heterostructures on Ge(001)," *J. Cryst. Growth*, vol. 123, no. 1–2, pp. 75–94, Sep. 1992.
- [31] R. Ragan and H. A. Atwater, "Measurement of the direct energy gap of coherently strained  $\text{Sn}_x\text{Ge}_{1-x}/\text{Ge}(001)$  heterostructures," *Appl. Phys. Lett.*, vol. 77, no. 21, p. 3418, Nov. 2000.
- [32] R. Hickey, N. Fernando, S. Zollner, J. Hart, R. Hazbun, and J. Kolodzey, "Properties of pseudomorphic and relaxed germanium $_{1-x}$ tin $_x$  alloys ( $x < 0.185$ ) grown by MBE," *J. Vac. Sci. Technol. B, Nanotechnol. Microelectron. Mater. Process. Meas. Phenom.*, vol. 35, no. 2, p. 021205, Mar. 2017.
- [33] J. Taraci, J. Tolle, J. Kouvetakis, M. R. McCartney, D. J. Smith, J. Menendez, and M. A. Santana, "Simple chemical routes to diamond-cubic germanium–tin alloys," *Appl. Phys. Lett.*, vol. 78, no. 23, pp. 3607–3609, Jun. 2001.
- [34] J. Taraci, S. Zollner, M. R. McCartney, J. Menendez, D. J. Smith, J. Tolle, M. Bauer, E. Duda, N. V. Edwards, and J. Kouvetakis, "Optical Vibrational and Structural Properties of  $\text{Ge}_{1-x}\text{Sn}_x$  alloys by UHV-CVD," *MRS Proc.*, vol. 692, p. H11.4.1, Jan. 2001.
- [35] R. Soref, J. Kouvetakis, J. Tolle, J. Menendez, and V. D'Costa, "Advances in SiGeSn technology," *J. Mater. Res.*, vol. 22, no. 12, pp. 3281–3291, Dec. 2007.
- [36] N. von den Driesch, D. Stange, S. Wirths, G. Mussler, B. Holländer, Z. Ikonik, J. M. Hartmann, T. Stoica, S. Mantl, D. Grützmacher, and D. Buca, "Direct Bandgap Group IV Epitaxy on Si for Laser Applications," *Chem. Mater.*, vol. 27, no. 13, pp. 4693–4702, Jul. 2015.
- [37] J. D. Gallagher, C. L. Senaratne, P. Sims, T. Aoki, J. Menéndez, and J. Kouvetakis, "Electroluminescence from GeSn heterostructure *pin* diodes at the indirect to direct transition," *Appl. Phys. Lett.*, vol. 106, no. 9, p. 091103, Mar. 2015.
- [38] J. P. Gupta, N. Bhargava, S. Kim, T. Adam, and J. Kolodzey, "Infrared electroluminescence from GeSn heterojunction diodes grown by molecular beam epitaxy," *Appl. Phys. Lett.*, vol. 102, no. 25, p. 251117, Jun. 2013.
- [39] J. Aubin, J. M. Hartmann, A. Gassenq, J. L. Rouviere, E. Robin, V. Delaye, D. Cooper, N. Mollard, V. Reboud, and V. Calvo, "Growth and structural properties of step-graded, high Sn content GeSn layers on Ge," *Semicond. Sci. Technol.*, vol. 32, no. 9, p. 094006, Sep. 2017.
- [40] G. Grzybowski, R. T. Beeler, L. Jiang, D. J. Smith, J. Kouvetakis, and J. Menéndez, "Next generation of  $\text{Ge}_{1-y}\text{Sn}_y$  ( $y = 0.01-0.09$ ) alloys grown on Si(100) via  $\text{Ge}_3\text{H}_8$  and  $\text{SnD}_4$ : Reaction kinetics and tunable emission," *Appl. Phys. Lett.*, vol. 101, no. 7, p. 072105, Aug.

2012.

- [41] S. Al-Kabi, S. A. Ghetmiri, J. Margetis, W. Du, A. Mosleh, W. Dou, G. Sun, R. A. Soref, J. Tolle, B. Li, M. Mortazavi, H. A. Naseem, and S.-Q. Yu, “Study of High-Quality GeSn Alloys Grown by Chemical Vapor Deposition towards Mid-Infrared Applications,” *J. Electron. Mater.*, vol. 45, no. 12, pp. 6251–6257, Dec. 2016.
- [42] J. Margetis, A. Mosleh, S. Al-Kabi, S. A. Ghetmiri, W. Du, W. Dou, M. Benamara, B. Li, M. Mortazavi, H. A. Naseem, S.-Q. Yu, and J. Tolle, “Study of low-defect and strain-relaxed GeSn growth via reduced pressure CVD in H<sub>2</sub> and N<sub>2</sub> carrier gas,” *J. Cryst. Growth*, vol. 463, pp. 128–133, Apr. 2017.
- [43] J. Margetis, S. Al-Kabi, W. Du, W. Dou, Y. Zhou, T. Pham, P. Grant, S. Ghetmiri, A. Mosleh, B. Li, J. Liu, G. Sun, R. Soref, J. Tolle, M. Mortazavi, and S.-Q. Yu, “Si-Based GeSn Lasers with Wavelength Coverage of 2–3 μm and Operating Temperatures up to 180 K,” *ACS Photonics*, vol. 5, no. 3, pp. 827–833, Mar. 2018.
- [44] W. Dou, M. Benamara, A. Mosleh, J. Margetis, P. Grant, Y. Zhou, S. Al-Kabi, W. Du, J. Tolle, B. Li, M. Mortazavi, and S.-Q. Yu, “Investigation of GeSn Strain Relaxation and Spontaneous Composition Gradient for Low-Defect and High-Sn Alloy Growth,” *Sci. Rep.*, vol. 8, no. 1, p. 5640, Dec. 2018.
- [45] S. Gupta, R. Chen, B. Magyari-Kope, H. Lin, Bin Yang, A. Nainani, Y. Nishi, J. S. Harris, and K. C. Saraswat, “GeSn technology: Extending the Ge electronics roadmap,” in *2011 International Electron Devices Meeting*, 2011, p. 16.6.1-16.6.4.
- [46] L. Kormoš, M. Kratzer, K. KostECKI, M. Oehme, T. Šikola, E. Kasper, J. Schulze, and C. Teichert, “Surface analysis of epitaxially grown GeSn alloys with Sn contents between 15% and 18%,” *Surf. Interface Anal.*, vol. 49, no. 4, pp. 297–302, Apr. 2017.
- [47] S. Su, B. Cheng, C. Xue, W. Wang, Q. Cao, H. Xue, W. Hu, G. Zhang, Y. Zuo, and Q. Wang, “GeSn p-i-n photodetector for all telecommunication bands detection,” *Opt. Express*, vol. 19, no. 7, p. 6400, Mar. 2011.
- [48] W. Wang, Q. Zhou, Y. Dong, E. S. Tok, and Y.-C. Yeo, “Critical thickness for strain relaxation of Ge<sub>1-x</sub>Sn<sub>x</sub> ( $x \leq 0.17$ ) grown by molecular beam epitaxy on Ge(001),” *Appl. Phys. Lett.*, vol. 106, no. 23, p. 232106, Jun. 2015.
- [49] J. Zheng, W. Huang, Z. Liu, C. Xue, C. Li, Y. Zuo, B. Cheng, and Q. Wang, “Influence of H<sub>2</sub> on strain evolution of high-Sn-content Ge<sub>1-x</sub>Sn<sub>x</sub> alloys,” *J. Mater. Sci.*, vol. 52, no. 1, pp. 431–436, Jan. 2017.
- [50] P. M. Wallace, C. L. Senaratne, C. Xu, P. E. Sims, J. Kouvetakis, and J. Menéndez, “Molecular epitaxy of pseudomorphic Ge<sub>1-y</sub>Sn<sub>y</sub> ( $y = 0.06–0.17$ ) structures and devices on Si/Ge at ultra-low temperatures via reactions of Ge<sub>4</sub>H<sub>10</sub> and SnD<sub>4</sub>,” *Semicond. Sci. Technol.*, vol. 32, no. 2, p. 025003, Feb. 2017.
- [51] F. Gencarelli, B. Vincent, J. Demeulemeester, A. Vantomme, A. Moussa, A. Franquet, A.

- Kumar, H. Bender, J. Meersschaut, W. Vandervorst, R. Loo, M. Caymax, K. Temst, and M. Heyns, "Crystalline Properties and Strain Relaxation Mechanism of CVD Grown GeSn," *ECS J. Solid State Sci. Technol.*, vol. 2, no. 4, pp. P134–P137, Jan. 2013.
- [52] R. Chen, S. Gupta, Y.-C. Huang, Y. Huo, C. W. Rudy, E. Sanchez, Y. Kim, T. I. Kamins, K. C. Saraswat, and J. S. Harris, "Demonstration of a Ge/GeSn/Ge Quantum-Well Microdisk Resonator on Silicon: Enabling High-Quality Ge(Sn) Materials for Micro- and Nanophotonics," *Nano Lett.*, vol. 14, no. 1, pp. 37–43, Jan. 2014.
- [53] S. M. Gates, C. M. Greenlief, D. B. Beach, and P. A. Holbert, "Decomposition of silane on Si(111)-(7×7) and Si(100)-(2×1) surfaces below 500 °C," *J. Chem. Phys.*, vol. 92, no. 5, pp. 3144–3153, Mar. 1990.
- [54] S. M. Gates and S. K. Kulkarni, "Kinetics of surface reactions in very low-pressure chemical vapor deposition of Si from SiH<sub>4</sub>," *Appl. Phys. Lett.*, vol. 58, no. 25, pp. 2963–2965, Jun. 1991.
- [55] D. C. Houghton, "Strain relaxation kinetics in Si<sub>1-x</sub>Ge<sub>x</sub>/Si heterostructures," *J. Appl. Phys.*, vol. 70, no. 4, pp. 2136–2151, Aug. 1991.
- [56] C. Li, S. John, E. Quinones, and S. Banerjee, "Cold-wall ultrahigh vacuum chemical vapor deposition of doped and undoped Si and Si<sub>1-x</sub>Ge<sub>x</sub> epitaxial films using SiH<sub>4</sub> and Si<sub>2</sub>H<sub>6</sub>," *J. Vac. Sci. Technol. A Vacuum, Surfaces, Film.*, vol. 14, no. 1, pp. 170–183, Jan. 1996.
- [57] Y.-W. Mo, D. E. Savage, B. S. Swartzentruber, and M. G. Lagally, "Kinetic pathway in Stranski-Krastanov growth of Ge on Si(001)," *Phys. Rev. Lett.*, vol. 65, no. 8, pp. 1020–1023, Aug. 1990.
- [58] M. Liehr, C. M. Greenlief, M. Offenbergl, and S. R. Kasi, "Equilibrium surface hydrogen coverage during silicon epitaxy using SiH<sub>4</sub>," *J. Vac. Sci. Technol. A Vacuum, Surfaces, Film.*, vol. 8, no. 3, pp. 2960–2964, May 1990.
- [59] C. Roland and G. H. Gilmer, "Growth of germanium films on Si(001) substrates," *Phys. Rev. B*, vol. 47, no. 24, pp. 16286–16298, Jun. 1993.
- [60] J. Holleman, A. E. T. Kuiper, and J. F. Verweij, "Kinetics of the Low Pressure Chemical Vapor Deposition of Polycrystalline Germanium-Silicon Alloys from SiH<sub>4</sub> and GeH<sub>4</sub>," *J. Electrochem. Soc.*, vol. 140, no. 6, p. 1717, Jun. 1993.
- [61] Kazuo Takahashi, Andreas Kunz, and Dirk Woiki, and P. Roth\*, "Thermal Decomposition of Tin Tetrachloride Based on Cl- and Sn-Concentration Measurements," 2000.
- [62] Y. Bogumilowicz, J. M. Hartmann, R. Truche, Y. Campidelli, G. Rolland, and T. Billon, "Chemical vapour etching of Si, SiGe and Ge with HCl; applications to the formation of thin relaxed SiGe buffers and to the revelation of threading dislocations," *Semicond. Sci. Technol.*, vol. 20, no. 2, pp. 127–134, Feb. 2005.
- [63] D. Dick, J.-F. Veyan, R. C. Longo, S. McDonnell, J. B. Ballard, X. Qin, H. Dong, J. H. G.

- Owen, J. N. Randall, R. M. Wallace, K. Cho, and Y. J. Chabal, "Digermane Deposition on Si(100) and Ge(100): from Adsorption Mechanism to Epitaxial Growth," *J. Phys. Chem. C*, vol. 118, no. 1, pp. 482–493, Jan. 2014.
- [64] F. Gencarelli, B. Vincent, L. Souriau, O. Richard, W. Vandervorst, R. Loo, M. Caymax, and M. Heyns, "Low-temperature Ge and GeSn Chemical Vapor Deposition using Ge<sub>2</sub>H<sub>6</sub>," *Thin Solid Films*, vol. 520, no. 8, pp. 3211–3215, Feb. 2012.
- [65] S. Wirths, R. Geiger, N. von den Driesch, G. Mussler, T. Stoica, S. Mantl, Z. Ikonic, M. Luysberg, S. Chiussi, J. M. Hartmann, H. Sigg, J. Faist, D. Buca, and D. Grützmacher, "Lasing in direct-bandgap GeSn alloy grown on Si," *Nat. Photonics*, vol. 9, no. 2, pp. 88–92, Feb. 2015.
- [66] S. Al-Kabi, S. A. Ghetmiri, J. Margetis, T. Pham, Y. Zhou, W. Dou, B. Collier, R. Quinde, W. Du, A. Mosleh, J. Liu, G. Sun, R. A. Soref, J. Tolle, B. Li, M. Mortazavi, H. A. Naseem, and S.-Q. Yu, "An optically pumped 2.5  $\mu\text{m}$  GeSn laser on Si operating at 110 K," *Appl. Phys. Lett.*, vol. 109, no. 17, p. 171105, Oct. 2016.
- [67] D. Stange, S. Wirths, R. Geiger, C. Schulte-Braucks, B. Marzban, N. von den Driesch, G. Mussler, T. Zabel, T. Stoica, J.-M. Hartmann, S. Mantl, Z. Ikonic, D. Grützmacher, H. Sigg, J. Witzens, and D. Buca, "Optically Pumped GeSn Microdisk Lasers on Si," *ACS Photonics*, vol. 3, no. 7, pp. 1279–1285, Jul. 2016.
- [68] V. Reboud, A. Gassenq, N. Pauc, J. Aubin, L. Milord, Q. M. Thai, M. Bertrand, K. Guilloy, D. Rouchon, J. Rothman, T. Zabel, F. Armand Pilon, H. Sigg, A. Chelnokov, J. M. Hartmann, and V. Calvo, "Optically pumped GeSn micro-disks with 16% Sn lasing at 3.1  $\mu\text{m}$  up to 180 K," *Appl. Phys. Lett.*, vol. 111, no. 9, p. 092101, Aug. 2017.
- [69] B. Cunningham, J. O. Chu, and S. Akbar, "Heteroepitaxial growth of Ge on (100) Si by ultrahigh vacuum, chemical vapor deposition," *Appl. Phys. Lett.*, vol. 59, no. 27, pp. 3574–3576, Dec. 1991.
- [70] O. O. Olubuyide, D. T. Danielson, L. C. Kimerling, and J. L. Hoyt, "Impact of seed layer on material quality of epitaxial germanium on silicon deposited by low pressure chemical vapor deposition," *Thin Solid Films*, vol. 508, no. 1–2, pp. 14–19, Jun. 2006.
- [71] G.-E. Chang, S.-W. Chang, and S. L. Chuang, "Strain-Balanced Ge<sub>z</sub>Sn<sub>1-z</sub>/Si<sub>x</sub>Ge<sub>y</sub>Sn<sub>1-x-y</sub> Multiple-Quantum-Well Lasers," *IEEE J. Quantum Electron.*, vol. 46, no. 12, pp. 1813–1820, 2010.
- [72] P. Norton and H. Levinstein, "Thermalization Time of Hot Photoexcited Holes in p-Type Germanium," *Phys. Rev. B*, vol. 6, no. 2, pp. 478–488, Jul. 1972.
- [73] M. Woerner, W. Frey, M. T. Portella, C. Ludwig, T. Elsaesser, and W. Kaiser, "Ultrafast thermalization of nonequilibrium holes in p-type germanium studied by femtosecond infrared spectroscopy," *Phys. Rev. B*, vol. 49, no. 24, pp. 17007–17010, Jun. 1994.
- [74] K. Tanaka, H. Ohtake, and T. Suemoto, "Determination of intervalley scattering time in

- germanium by subpicosecond time-resolved Raman spectroscopy,” *Phys. Rev. Lett.*, vol. 71, no. 12, pp. 1935–1938, Sep. 1993.
- [75] G. Mak and H. M. van Driel, “Femtosecond transmission spectroscopy at the direct band edge of germanium,” *Phys. Rev. B*, vol. 49, no. 23, pp. 16817–16820, Jun. 1994.
- [76] R. Geiger, J. Frigerio, M. J. Süess, D. Chrastina, G. Isella, R. Spolenak, J. Faist, and H. Sigg, “Excess carrier lifetimes in Ge layers on Si,” *Appl. Phys. Lett.*, vol. 104, no. 6, p. 062106, Feb. 2014.
- [77] G. Sun, R. A. Soref, and H. H. Cheng, “Design of a Si-based lattice-matched room-temperature GeSn/GeSiSn multi-quantum-well mid-infrared laser diode,” *Opt. Express*, vol. 18, no. 19, p. 19957, Sep. 2010.
- [78] J. Liu, X. Sun, D. Pan, X. Wang, L. C. Kimerling, T. L. Koch, and J. Michel, “Tensile-strained, n-type Ge as a gain medium for monolithic laser integration on Si,” *Opt. Express*, vol. 15, no. 18, p. 11272, Sep. 2007.
- [79] G. Grzybowski, R. Roucka, J. Mathews, L. Jiang, R. T. Beeler, J. Kouvetakis, and J. Menéndez, “Direct versus indirect optical recombination in Ge films grown on Si substrates,” *Phys. Rev. B*, vol. 84, no. 20, p. 205307, Nov. 2011.
- [80] X. Q. Zhou, H. M. van Driel, and G. Mak, “Femtosecond kinetics of photoexcited carriers in germanium,” *Phys. Rev. B*, vol. 50, no. 8, pp. 5226–5230, Aug. 1994.
- [81] H.-C. Luan, D. R. Lim, K. K. Lee, K. M. Chen, J. G. Sandland, K. Wada, and L. C. Kimerling, “High-quality Ge epilayers on Si with low threading-dislocation densities,” *Appl. Phys. Lett.*, vol. 75, no. 19, p. 2909, Nov. 1999.
- [82] A. S. Kumbhar, D. M. Bhusari, and S. T. Kshirsagar, “Growth of clean amorphous silicon–carbon alloy films by hot-filament assisted chemical vapor deposition technique,” *Appl. Phys. Lett.*, vol. 66, no. 14, pp. 1741–1743, Apr. 1995.
- [83] C. P. Beetz, C. V. Cooper, and T. A. Perry, “Ultralow-load indentation hardness and modulus of diamond films deposited by hot-filament-assisted CVD,” *J. Mater. Res.*, vol. 5, no. 11, pp. 2555–2561, Nov. 1990.
- [84] R. A. Rudder, G. G. Fountain, and R. J. Markunas, “Remote plasma-enhanced chemical-vapor deposition of epitaxial Ge films,” *J. Appl. Phys.*, vol. 60, no. 10, pp. 3519–3522, Nov. 1986.
- [85] G. Isella, J. Osmond, M. Kummer, R. Kaufmann, and H. von Känel, “Heterojunction photodiodes fabricated from Ge/Si (100) layers grown by low-energy plasma-enhanced CVD,” *Semicond. Sci. Technol.*, vol. 22, no. 1, pp. S26–S28, Jan. 2007.
- [86] G. Isella, D. Chrastina, B. Rössner, T. Hackbarth, H.-J. Herzog, U. König, and H. von Känel, “Low-energy plasma-enhanced chemical vapor deposition for strained Si and Ge heterostructures and devices,” *Solid. State. Electron.*, vol. 48, no. 8, pp. 1317–1323, Aug.

2004.

- [87] A. Gassenq, L. Milord, J. Aubin, N. Pauc, K. Guilloy, J. Rothman, D. Rouchon, A. Chelnokov, J. M. Hartmann, V. Reboud, and V. Calvo, “Raman spectral shift versus strain and composition in GeSn layers with 6%–15% Sn content,” *Appl. Phys. Lett.*, vol. 110, no. 11, p. 112101, Mar. 2017.
- [88] H. Tran, W. Du, S. A. Ghetmiri, A. Mosleh, G. Sun, R. A. Soref, J. Margetis, J. Tolle, B. Li, H. A. Naseem, and S.-Q. Yu, “Systematic study of  $\text{Ge}_{1-x}\text{Sn}_x$  absorption coefficient and refractive index for the device applications of Si-based optoelectronics,” *J. Appl. Phys.*, vol. 119, no. 10, p. 103106, Mar. 2016.
- [89] X. W. Lin, Z. Liliental-Weber, J. Washburn, E. R. Weber, A. Sasaki, A. Wakahara, and T. Hasegawa, “Ge/Si heterostructures grown by Sn-surfactant-mediated molecular beam epitaxy,” *J. Vac. Sci. Technol. B Microelectron. Nanom. Struct.*, vol. 13, no. 4, p. 1805, Jul. 1995.
- [90] R. Haydock, V. Heine, and M. J. Kelly, “Electronic structure based on the local atomic environment for tight-binding bands,” *J. Phys. C Solid State Phys.*, vol. 5, no. 20, pp. 2845–2858, Oct. 1972.
- [91] E. Antončík, “Approximate formulation of the orthogonalized plane-wave method,” *J. Phys. Chem. Solids*, vol. 10, no. 4, pp. 314–320, Aug. 1959.
- [92] L. M. Falicov and S. Golin, “Electronic Band Structure of Arsenic. I. Pseudopotential Approach,” *Phys. Rev.*, vol. 137, no. 3A, pp. A871–A882, Feb. 1965.
- [93] S. L. Chuang, *Physics of photonic devices*. John Wiley & Sons, 2009.
- [94] G. Dresselhaus, “Effective mass approximation for excitons,” *J. Phys. Chem. Solids*, vol. 1, no. 1–2, pp. 14–22, Sep. 1956.
- [95] E. O. Kane, “Band structure of indium antimonide,” *J. Phys. Chem. Solids*, vol. 1, no. 4, pp. 249–261, Jan. 1957.
- [96] I. Vurgaftman, J. R. Meyer, and L. R. Ram-Mohan, “Band parameters for III–V compound semiconductors and their alloys,” *J. Appl. Phys.*, vol. 89, no. 11, pp. 5815–5875, Jun. 2001.
- [97] W.-J. Yin, X.-G. Gong, and S.-H. Wei, “Origin of the unusually large band-gap bowing and the breakdown of the band-edge distribution rule in the  $\text{Sn}_x\text{Ge}_{1-x}$  alloys,” *Phys. Rev. B*, vol. 78, no. 16, p. 161203, Oct. 2008.
- [98] V. R. D’Costa, C. S. Cook, A. G. Birdwell, C. L. Littler, M. Canonico, S. Zollner, J. Kouvetakis, and J. Menéndez, “Optical critical points of thin-film  $\text{Ge}_{1-y}\text{Sn}_y$  alloys: A comparative  $\text{Ge}_{1-y}\text{Sn}_y/\text{Ge}_{1-x}\text{Si}_x$  study,” *Phys. Rev. B*, vol. 73, no. 12, p. 125207, Mar. 2006.
- [99] L. Jiang, J. D. Gallagher, C. L. Senaratne, T. Aoki, J. Mathews, J. Kouvetakis, and J. Menéndez, “Compositional dependence of the direct and indirect band gaps in  $\text{Ge}_{1-y}\text{Sn}_y$



- alloys from room temperature photoluminescence: implications for the indirect to direct gap crossover in intrinsic and  $n$ -type materials,” *Semicond. Sci. Technol.*, vol. 29, no. 11, p. 115028, Nov. 2014.
- [100] A. A. Tonkikh, C. Eisenschmidt, V. G. Talalaev, N. D. Zakharov, J. Schilling, G. Schmidt, and P. Werner, “Pseudomorphic GeSn/Ge(001) quantum wells: Examining indirect band gap bowing,” *Appl. Phys. Lett.*, vol. 103, no. 3, p. 032106, Jul. 2013.
- [101] A. R. Adams, “Band-structure engineering for low-threshold high-efficiency semiconductor lasers,” *Electron. Lett.*, vol. 22, no. 5, p. 249, 1986.
- [102] E. Yablonovitch and E. O. Kane, “Band structure engineering of semiconductor lasers for optical communications,” *J. Light. Technol.*, vol. 6, no. 8, pp. 1292–1299, 1988.
- [103] J. Xie, A. V. G. Chizmeshya, J. Tolle, V. R. D’Costa, J. Menendez, and J. Kouvetakis, “Synthesis, Stability Range, and Fundamental Properties of Si–Ge–Sn Semiconductors Grown Directly on Si(100) and Ge(100) Platforms,” *Chem. Mater.*, vol. 22, no. 12, pp. 3779–3789, Jun. 2010.
- [104] J. Margetis, S. Al-Kabi, W. Du, W. Dou, Y. Zhou, T. Pham, P. Grant, S. Ghetmiri, A. Mosleh, and B. Li, “Si-based GeSn lasers with wavelength coverage of 2 to 3  $\mu\text{m}$  and operating temperatures up to 180 K,” *arXiv Prepr. arXiv1708.05927*, 2017.
- [105] R. People and J. C. Bean, “Calculation of critical layer thickness versus lattice mismatch for  $\text{Ge}_x\text{Si}_{1-x}/\text{Si}$  strained-layer heterostructures,” *Appl. Phys. Lett.*, vol. 47, no. 3, pp. 322–324, Aug. 1985.
- [106] R. Beeler, R. Roucka, A. V. G. Chizmeshya, J. Kouvetakis, and J. Menéndez, “Nonlinear structure-composition relationships in the  $\text{Ge}_{1-y}\text{Sn}_y/\text{Si}(100)$  ( $y < 0.15$ ) system,” *Phys. Rev. B*, vol. 84, no. 3, p. 035204, Jul. 2011.
- [107] J. Kouvetakis, J. Menendez, and A. V. G. Chizmeshya, “TIN-BASED GROUP IV SEMICONDUCTORS: New Platforms for Opto- and Microelectronics on Silicon,” *Annu. Rev. Mater. Res.*, vol. 36, no. 1, pp. 497–554, Aug. 2006.
- [108] Y. Chibane and M. Ferhat, “Electronic structure of  $\text{Sn}_x\text{Ge}_{1-x}$  alloys for small Sn compositions: Unusual structural and electronic properties,” *J. Appl. Phys.*, vol. 107, no. 5, p. 053512, Mar. 2010.
- [109] J. W. Matthews and A. E. Blakeslee, “Defects in epitaxial multilayers: I. Misfit dislocations,” *J. Cryst. Growth*, vol. 27, pp. 118–125, Dec. 1974.
- [110] R. Beanland, D. J. Dunstan, and P. J. Goodhew, “Plastic relaxation and relaxed buffer layers for semiconductor epitaxy,” *Adv. Phys.*, vol. 45, no. 2, pp. 87–146, Apr. 1996.
- [111] F. Nabarro, “Theory of crystal dislocations,” 1967.
- [112] Y. B. Bolkhovityanov and L. V. Sokolov, “Ge-on-Si films obtained by epitaxial growing:

- edge dislocations and their participation in plastic relaxation,” *Semicond. Sci. Technol.*, vol. 27, no. 4, p. 043001, Apr. 2012.
- [113] P. M. J. Marée, J. C. Barbour, J. F. van der Veen, K. L. Kavanagh, C. W. T. Bulle-Lieuwma, and M. P. A. Vieggers, “Generation of misfit dislocations in semiconductors,” *J. Appl. Phys.*, vol. 62, no. 11, pp. 4413–4420, Dec. 1987.
- [114] Y. Chen, X. W. Lin, Z. Liliental-Weber, J. Washburn, J. F. Klem, and J. Y. Tsao, “Dislocation formation mechanism in strained  $\text{In}_x\text{Ga}_{1-x}\text{As}$  islands grown on GaAs(001) substrates,” *Appl. Phys. Lett.*, vol. 68, no. 1, p. 111, Jun. 1998.
- [115] J. Narayan, “Recent progress in thin film epitaxy across the misfit scale (2011 Acta Gold Medal Paper),” *Acta Mater.*, vol. 61, no. 8, pp. 2703–2724, May 2013.
- [116] P. J. Simmonds and M. Larry Lee, “Tensile-strained growth on low-index GaAs,” *J. Appl. Phys.*, vol. 112, no. 5, p. 054313, Sep. 2012.
- [117] J. W. Matthews, A. E. Blakeslee, and S. Mader, “Use of misfit strain to remove dislocations from epitaxial thin films,” *Thin Solid Films*, vol. 33, no. 2, pp. 253–266, Apr. 1976.
- [118] E. A. Fitzgerald, G. P. Watson, R. E. Proano, D. G. Ast, P. D. Kirchner, G. D. Pettit, and J. M. Woodall, “Nucleation mechanisms and the elimination of misfit dislocations at mismatched interfaces by reduction in growth area,” *J. Appl. Phys.*, vol. 65, no. 6, pp. 2220–2237, Mar. 1989.
- [119] R. S. Goldman, K. L. Kavanagh, H. H. Wieder, S. N. Ehrlich, and R. M. Feenstra, “Effects of GaAs substrate misorientation on strain relaxation in  $\text{In}_x\text{Ga}_{1-x}\text{As}$  films and multilayers,” *J. Appl. Phys.*, vol. 83, no. 10, p. 5137, Apr. 1998.
- [120] J. Xie, J. Tolle, V. R. D’Costa, A. V. G. Chizmeshya, J. Menéndez, and J. Kouvetakis, “Direct integration of active  $\text{Ge}_{1-x}(\text{SiSn})_x$  semiconductors on Si(100),” *Appl. Phys. Lett.*, vol. 95, no. 18, p. 181909, Nov. 2009.
- [121] J. L. Martins and A. Zunger, “Bond lengths around isovalent impurities and in semiconductor solid solutions,” *Phys. Rev. B*, vol. 30, no. 10, pp. 6217–6220, Nov. 1984.
- [122] E. Kasper and H.-J. Herzog, “Elastic strain and misfit dislocation density in  $\text{Si}_{0.92}\text{Ge}_{0.08}$  films on silicon substrates,” *Thin Solid Films*, vol. 44, no. 3, pp. 357–370, Aug. 1977.
- [123] C. G. Van de Walle, “Band lineups and deformation potentials in the model-solid theory,” *Phys. Rev. B*, vol. 39, no. 3, p. 1871, 1989.
- [124] P. Moontragoon, R. A. Soref, and Z. Ikonik, “The direct and indirect bandgaps of unstrained  $\text{Si}_x\text{Ge}_{1-x-y}\text{Sn}_y$  and their photonic device applications,” *J. Appl. Phys.*, vol. 112, no. 7, p. 073106, Oct. 2012.
- [125] A. Walsh, J. L. F. Da Silva, and S.-H. Wei, “Origins of band-gap renormalization in degenerately doped semiconductors,” *Phys. Rev. B*, vol. 78, no. 7, p. 075211, Aug. 2008.

- [126] D. Stange, N. von den Driesch, D. Rainko, C. Schulte-Braucks, S. Wirths, G. Mussler, A. T. Tiedemann, T. Stoica, J. M. Hartmann, Z. Ikonik, S. Mantl, D. Grützmacher, and D. Buca, “Study of GeSn based heterostructures: towards optimized group IV MQW LEDs,” *Opt. Express*, vol. 24, no. 2, p. 1358, Jan. 2016.
- [127] M. Jaros, “Simple analytic model for heterojunction band offsets,” *Phys. Rev. B*, vol. 37, no. 12, pp. 7112–7114, Apr. 1988.
- [128] C. Hilsum, “Transferred Electron Amplifiers and Oscillators,” *Proc. IRE*, vol. 50, no. 2, pp. 185–189, Feb. 1962.
- [129] E. F. Schubert, T. Gessmann, and J. K. Kim, “Light Emitting Diodes,” in *Kirk-Othmer Encyclopedia of Chemical Technology*, Hoboken, NJ, USA: John Wiley & Sons, Inc., 2005.
- [130] W. D. A. M. de Boer, D. Timmerman, K. Dohnalová, I. N. Yassievich, H. Zhang, W. J. Buma, and T. Gregorkiewicz, “Red spectral shift and enhanced quantum efficiency in phonon-free photoluminescence from silicon nanocrystals,” *Nat. Nanotechnol.*, vol. 5, no. 12, pp. 878–884, Dec. 2010.
- [131] P. C. Grant, J. Margetis, Y. Zhou, W. Dou, G. Abernathy, A. Kuchuk, W. Du, B. Li, J. Tolle, J. Liu, G. Sun, R. A. Soref, M. Mortazavi, and S.-Q. Yu, “Direct bandgap type-I GeSn/GeSn quantum well on a GeSn- and Ge- buffered Si substrate,” *AIP Adv.*, vol. 8, no. 2, p. 025104, Feb. 2018.
- [132] E. A. Fitzgerald, “GeSi/Si NANOSTRUCTURES,” *Annu. Rev. Mater. Sci.*, vol. 25, pp. 417–54, 1995.

## Appendix A

Table A.1 The relevant parameters of GeSn for the calculation in this dissertation.

Parameters	Ge	Sn
Lattice constant $a$ (nm)	0.56573[71]	0.64892[71]
Bowing parameter $b$ (nm)	-0.0066[106]	
Effective mass $m_c$ (m0)	0.038[71]	0.058[71]
Effective mass $m_{t,L}$ (m0)	0.0807[71]	0.075[71]
Effective mass $m_{l,L}$ (m0)	1.57[71]	1.478[71]
Luttinger's parameters $\gamma_1$	13.38[71]	-14.97[71]
Luttinger's parameters $\gamma_2$	4.24[71]	-10.61[71]
Luttinger's parameters $\gamma_3$	5.69[71]	-8.52[71]
Bandgap $E_g^F$ (eV)	0.7985[71]	-0.413[71]
Bandgap $E_g^L$ (eV)	0.664[71]	0.092[71]
Deformation potentials $a_c$ (eV)	-8.24[71]	-6[71]
Deformation potentials $a_L$ (eV)	-1.54[71]	-2.14[71]
Deformation potentials $a_v$ (eV)	1.24[71]	1.58[71]
Deformation potentials $b_v$ (eV)	-2.9[71]	-2.7[71]
Elastic constants $C_{11}$ (GPa)	128.53[71]	69.00[71]
Elastic constants $C_{12}$ (GPa)	48.26[71]	29.30[71]
Elastic constants $C_{44}$ (GPa)	68.30[71]	36.20[71]
Calculated Poisson ratio $v = \frac{C_{12}}{C_{11} + C_{12}}$	0.27	0.30
Shear modulus $\mu$ (GPa)[132] $\mu = C_{44} - \frac{(2C_{44} + C_{12} - C_{11})}{3}$	49.52	25.30
Interaction parameter $\alpha$ (eV)	0.27[121][103]	

## Appendix B

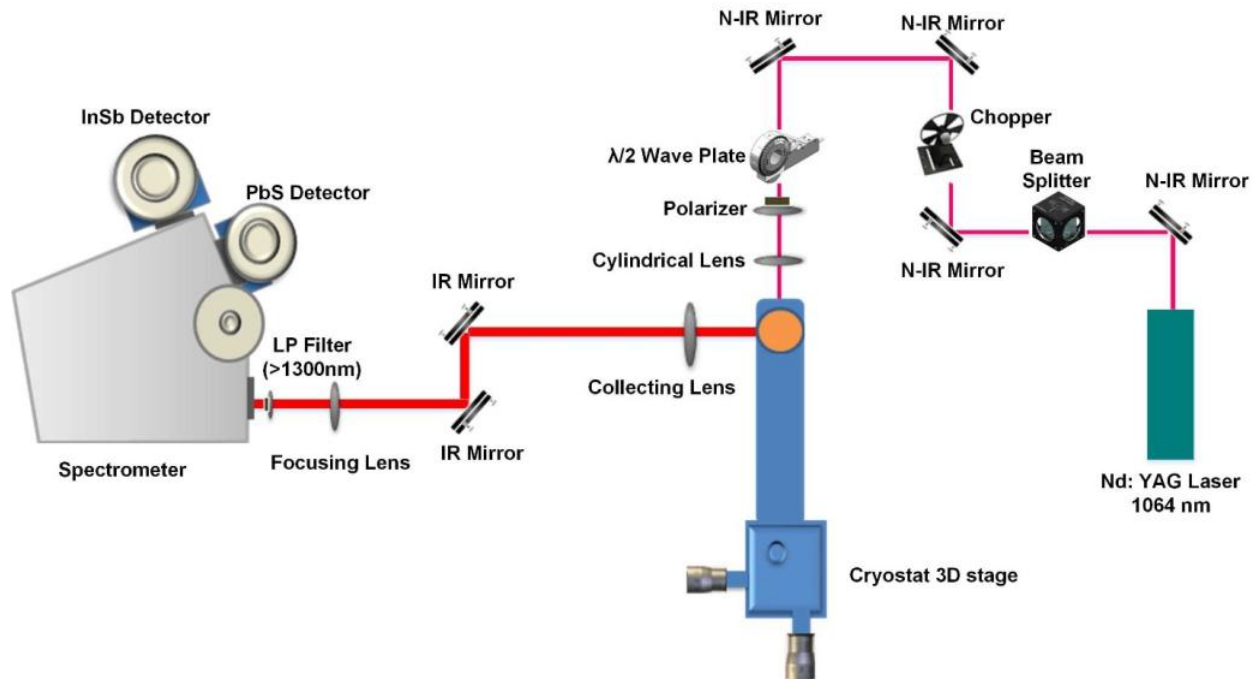


Figure B.1 The schematic diagram of the setup of optically pumped edge emitting GeSn laser.

The optical pumped lasing performance was investigated using a two pumping sources: 1) A 1064 nm pulsed laser with 45 kHz repetition rate and 6 ns pulse width; 2) A 1950 nm pulsed laser with 10 kHz repetition rate and 10 ns pulse width. The lasing spectra was spectrally analyzed by the combination of iHR320 spectroscopy. Two infrared detectors were utilized for lasing spectra: 1) A liquid nitrogen cooled Indium Antimonide (InSb) detector with the wavelength detection cut-off at 5.0  $\mu\text{m}$ ; 2) A thermoelectric-cooled lead sulfide (PbS) detector with the cut-off at 3.0  $\mu\text{m}$ . A SR830 DSP lock-in system along with a chopper was applied to amplify the lasing signal. The laser beam was collimated to a 20  $\mu\text{m}$ -width and 3.2 mm-length pumping strip on to GeSn waveguide structure by a cylindrical lens. The samples were first mounted on a Si chip carrier and put into a liquid nitrogen cold-finger cryostat. A computer-controlled variable attenuator was used to automatically measure typical laser-input versus laser-output (L-L) curve. Through rotating the

motor-controlled  $\frac{1}{2} \lambda$  wave plate sandwiched by two linear polarizers, the continuous power change of pumping laser could be obtained with the automatic control.

## Appendix C

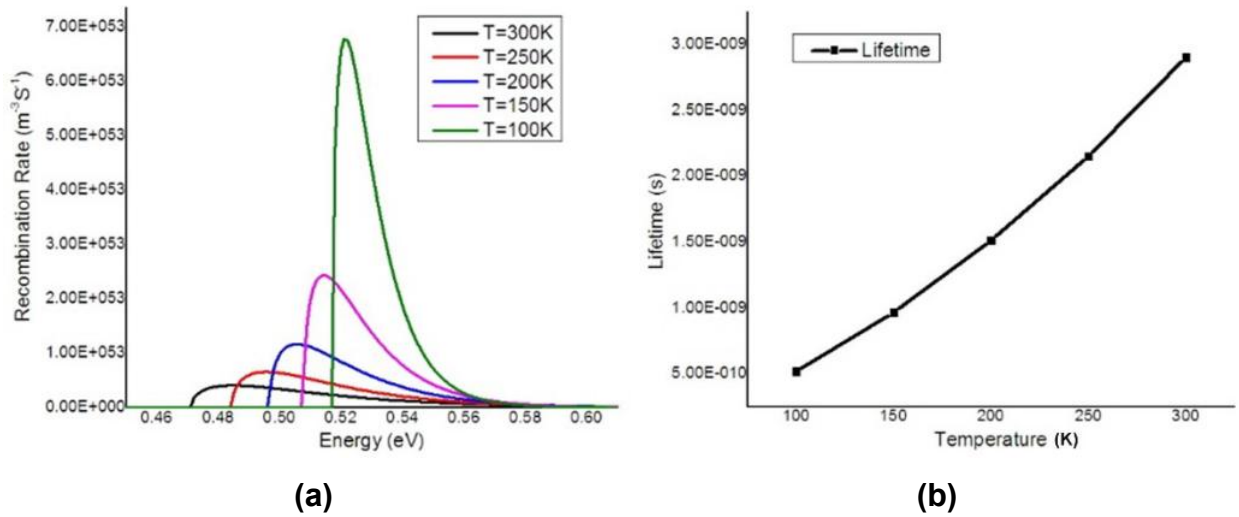


Figure C.1 (a) The temperature-dependent recombination rate of direct bandgap of  $\text{Ge}_{0.88}\text{Sn}_{0.12}$ . The temperature-dependent carrier lifetime of direct bandgap of  $\text{Ge}_{0.88}\text{Sn}_{0.12}$ .

The theoretical radiative recombination rate of direct bandgap of  $\text{Ge}_{0.88}\text{Sn}_{0.12}$  was calculated with the temperature from 100 to 300 K, as shown in Figure C.1 (a). As expected, a blue shift of emission peaks was observed when the temperature decreases from 300 to 100 K. Meanwhile, the intensity of emission increases dramatically with the decrease of temperature. The temperature-dependent lifetime of direct bandgap of  $\text{Ge}_{0.88}\text{Sn}_{0.12}$  was also calculated in Figure C.1 (b). With the decrease of temperature from 300 to 100 K, the lifetime decreases as well. The lifetime ranging from 500 ps to 3 ns was obtained.

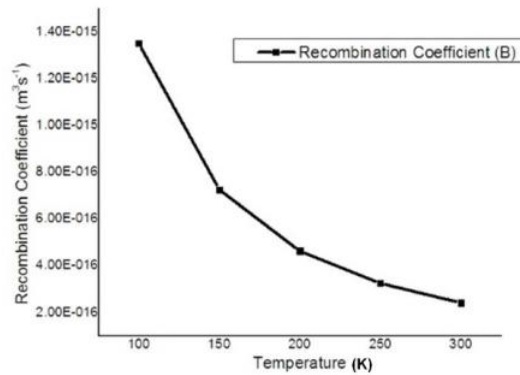


Figure C.2 The calculation recombination coefficient  $B$  of direct bandgap of  $\text{Ge}_{0.88}\text{Sn}_{0.12}$ .

The total recombination rate of carriers  $R(n)$  is[93]

$$R(n) = An + Bn^2 + Cn^3 = \frac{n}{\tau(n)} \quad \text{Equation C.1}$$

where  $An$  is the non-radiative (SRH) recombination rate;  $Bn^2$  is the radiative recombination rate and  $Cn^3$  is the non-radiative Auger processes. The carrier lifetime can be calculated as

$$\tau(n) = \frac{1}{A + Bn + Cn^2} \quad \text{Equation C.2}$$

where  $\tau(n)$  the carrier lifetime; B is called the recombination coefficient, which could be calculated as

$$B = \frac{1}{n * \tau_r} \quad \text{Equation C.3}$$

The recombination coefficient B of direct bandgap of  $\text{Ge}_{0.88}\text{Sn}_{0.12}$  was calculated as the function of temperature, as shown in Figure C.2. With the decrease of temperature, the recombination coefficient B decreases monolithically.



## Appendix D

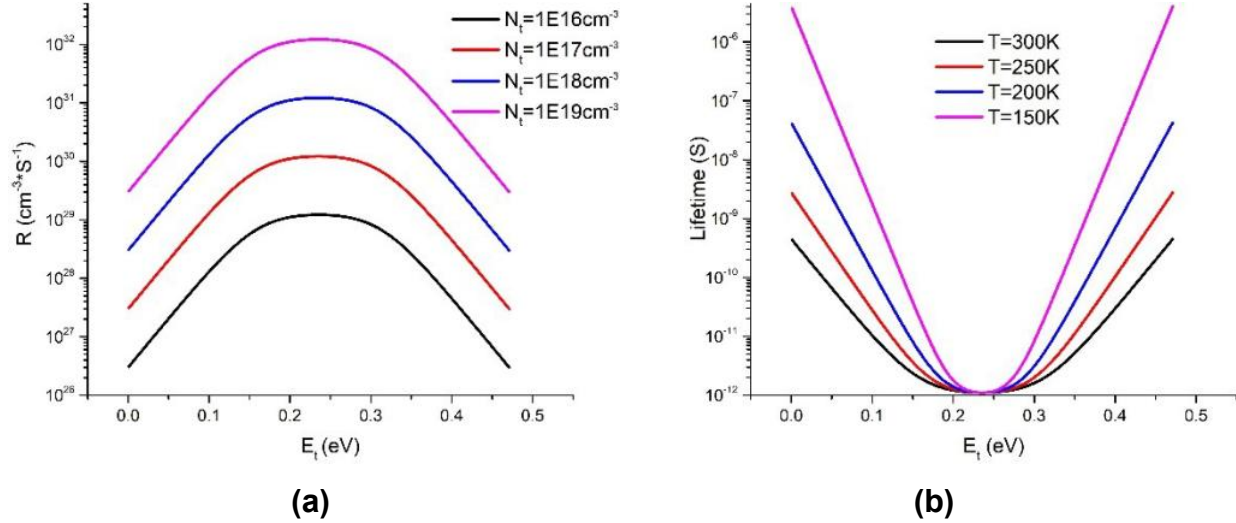


Figure D.1 (a) The recombination rate of Shockley-Read-Hall (SRH) process as a function of energy position of traps states within bandgap energy ( $E_t$ ) under different densities of trap states ( $N_t$ ). (b) The temperature-dependent carrier lifetime by SRH process with the  $N_t=10^{16} \text{ cm}^{-3}$  as an example.

The  $\text{Ge}_{0.88}\text{Sn}_{0.12}$  was chosen as an example. The non-radiative recombination rate of Shockley-Read-Hall (SRH) process as the function of the energy position of trap states which are introduced by dislocations. The range of densities of trap energy states ( $N_t$ ) between  $10^{16} \text{ cm}^{-3}$  to  $10^{19} \text{ cm}^{-3}$  was considered. The recombination rates achieve the maximum when the trap energy ( $E_t$ ) was located in the middle of direct bandgap energy. With increasing the density of trap states the recombination rate increases, as expected. The temperature-dependent carrier lifetimes by SRH process with the  $N_t=10^{16} \text{ cm}^{-3}$  were also calculated under different temperatures. The SRH lifetimes reach the minimum when  $E_t$  locates in the middle. At room temperature (300 K), the lifetime of SRH ranges from 1 ps to 1 ns.

## Appendix E

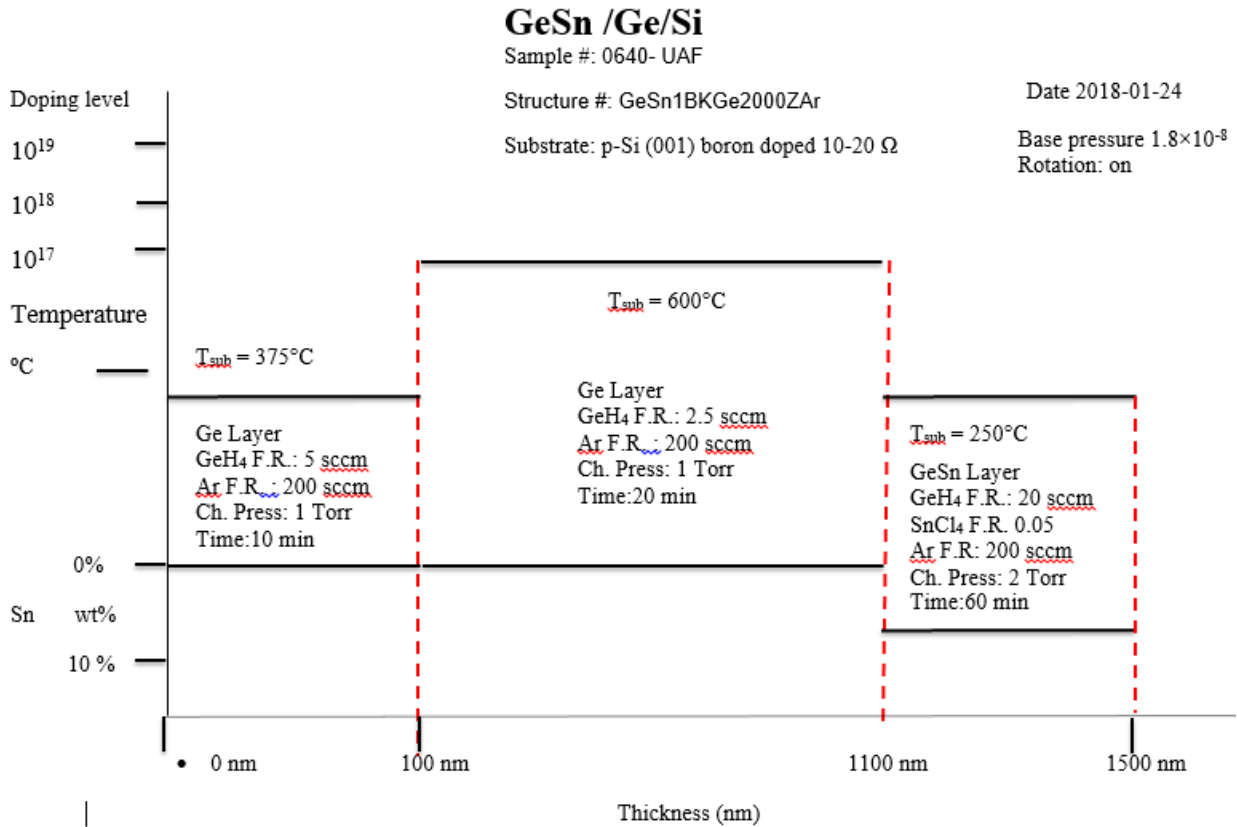


Figure E.1 The typical cross section of CVD growth of GeSn on Ge buffered Si.

One of the typical example of cross-section design was shown in Figure E.1. The GeSn sample on Ge buffered Si substrate was firstly designed prior to the UHV-CVD growth. The Si substrate is a 4-inch P-type (Boron doped) wafer. The base pressure of reaction chamber is  $1.8 \times 10^{-8}$  Torr. In order to improve the uniformity of CVD growth, the substrate is rotated which is driven by servo motor during the CVD epitaxy. The low/high temperature (375/600°C) two step Ge buffer was firstly grown on Si substrate. The precursor of GeH<sub>4</sub> and carrier gas of Ar were used. The pressure was kept as 1 Torr during the Ge buffer growth. The target thickness of Ge buffer is 1100 nm. After the Ge buffer growth, the temperature was reduced to 250°C for GeSn growth. The precursors of GeH<sub>4</sub> and SnCl<sub>4</sub> were employed. During the GeSn epitaxy the pressure was kept 2 Torr. The target thickness of GeSn epitaxy is 400 nm.

## Appendix F: All Publications Published, Submitted, and Planned

Chapter 4, 5, 6 were largely reproduced from publications in Scientific Reports. Chapter 7 was partly reproduced from the papers which is ready for the submission of Optica. Chapter 8 was partly reproduced from the publication in Journal of Electronic Materials.

Chapter 4, 5, 6 were originally published as:

1. **Wei Dou**, Mourad Benamara, Aboozar Mosleh, Joe Margetis, Perry Grant, Yiyin Zhou, Sattar Al-Kabi et al. "Investigation of GeSn Strain Relaxation and Spontaneous Composition Gradient for Low-Defect and High-Sn Alloy Growth." Scientific reports 8, no. 1 (2018): 5640.

Part of chapter 7 was originally published as:

2. **Wei Dou**, Yiyin Zhou, Joe Margetis, Wei Du, Jifeng Liu, Greg Sun, Richard A. Soref, John Tolle, Baohua Li, Mansour Mortazavi, and Shui-Qing Yu, "Investigation of lasing at 3  $\mu\text{m}$  from GeSn with the compositional graded Sn content up to 22.3%", ready to submit to Optica.

Part of chapter 8 was originally published as:

3. **Wei Dou**, Seyed Ghetmiri, Sattar Al-Kabi, Aboozar Mosleh, Yiyin Zhou, Bader Alharthi, Wei Du, Joe Margetis, John Tolle, Andrian Kuchuk, Mourad Benamara, Baohua Li, Hameed Naseem, Mansour Mortazavi, and Shui-Qing Yu, Structural and Optical Characteristics of GeSn Quantum Wells for Silicon-Based Mid-Infrared Optoelectronic Applications, Journal of Electronic Materials (2016), 10.1007/s11664-016-5031-2.

### F.1 List of peer reviewed published works

1. **Wei Dou**, Mourad Benamara, Aboozar Mosleh, Joe Margetis, Perry Grant, Yiyin Zhou, Sattar Al-Kabi et al. "Investigation of GeSn Strain Relaxation and Spontaneous Composition Gradient for Low-Defect and High-Sn Alloy Growth." Scientific reports 8, no. 1 (2018): 5640.
2. Grant, Perry C., Joe Margetis, Yiyin Zhou, **Wei Dou**, Grey Abernathy, Andrian Kuchuk, Wei Du et al. "Direct bandgap type-I GeSn/GeSn quantum well on a GeSn-and Ge-buffered Si substrate." AIP Advances 8, no. 2 (2018): 025104.
3. Bader Alharthi, Joshua M. Grant, **Wei Dou**, Perry C. Grant, Aboozar Mosleh, Wei Du, Mansour Mortazavi, Baohua Li, Hameed Naseem, and Shui-Qing Yu, Heteroepitaxial Germanium-on-Silicon Using RF Plasma Enhancement for Ultra-High Vacuum Chemical Vapor Deposition, accepted by Journal of Electronic Materials.
4. Margetis, Joe, Sattar Al-Kabi, Wei Du, **Wei Dou**, Yiyin Zhou, Thach Pham, Perry Grant et al. "Si-based GeSn lasers with wavelength coverage of 2 to 3  $\mu\text{m}$  and operating temperatures up to 180 K." ACS Photonics (2017).

5. J. Margetis, A. Mosleh, S. Al-Kabi, S. Ghetmiri, W. Du, **Wei Dou**, M. Benamara, B. Li, M. Mortazavi, H. Naseem, S.-Q. Yu and J. Tolle, Study of low-defect and strain-relaxed GeSn growth via reduced pressure CVD for mid-infrared applications, Journal of Crystal Growth, Accepted, In Press (2017).
6. Seyed A. Ghetmiri, Yiyin Zhou, Joe Margetis, Sattar Al-Kabi, **Wei Dou**, Aboozar Mosleh, Wei Du, Andrian Kuchuk, Jifeng Liu, Greg Sun, Richard A. Soref, John Tolle, Hameed A. Naseem, Baohua LI, Mansour Mortazavi, and Shui-Qing Yu, Study of SiGeSn/GeSn/SiGeSn structure towards direct bandgap type-I quantum well for all group-IV-optoelectronics, Optics Letters, Vol. 42, No. 3 (2017), pp 387- 390.
7. Margetis, Joe, Aboozar Mosleh, Seyed Amir Ghetmiri, Sattar Al-Kabi, **Wei Dou**, Wei Du, Nupur Bhargava et al. "Fundamentals of Ge<sub>1-x</sub>Sn<sub>x</sub> and Si<sub>y</sub>Ge<sub>1-x-y</sub>Sn<sub>x</sub> RPCVD epitaxy." Materials Science in Semiconductor Processing 70 (2017): 38-43.
8. Alharthi, Bader, Joe Margetis, Huong Tran, Sattar Al-kabi, **Wei Dou**, Seyed Amir Ghetmiri, Aboozar Mosleh et al. "Study of material and optical properties of Si<sub>x</sub>Ge<sub>1-xy</sub>Sn<sub>y</sub> alloys for Si-based optoelectronic device applications." Optical Materials Express 7, no. 10 (2017): 3517-3528.
9. Grant, Perry C., **Wei Dou**, Bader Alharthi, Joshua M. Grant, Aboozar Mosleh, Wei Du, Baohua Li, Mansour Mortazavi, Hameed A. Naseem, and Shui-Qing Yu. "Comparison study of the low temperature growth of dilute GeSn and Ge." Journal of Vacuum Science & Technology B, Nanotechnology and Microelectronics: Materials, Processing, Measurement, and Phenomena 35, no. 6 (2017): 061204.
10. Sattar Al-Kabi, Seyed Ghetmiri, Joe Margetis, Thach Pham, Yiyin Zhou, **Wei Dou**, Bria Collier, Randy Quinde, Wei Du, Aboozar Mosleh, Jifeng Liu, Greg Sun, Richard Soref, John Tolle, Baohua Li, Mansour Mortazavi, Hameed Naseem, and Shui-Qing Yu, An optically pumped 2.5 μm GeSn laser on Si operating at 110 K, Applied Physics Letters 109, 171105 (2016); doi: 10.1063/1.4966141
11. Sattar Al-Kabi, Seyed Ghetmiri, Joe Margetis, Wei Du, Aboozar Mosleh, **Wei Dou**, Greg Sun, Richard Soref, John Tolle, Baohua Li, Mansour Mortazavi, Hameed Naseem, Shui-Qing Yu, Study of High Quality GeSn Alloys Grown by Chemical Vapor Deposition towards Mid-Infrared Applications, Journal of Electronic Materials (2016), 10.1007/s11664-016-5028-x.
12. **Wei Dou**, Seyed Ghetmiri, Sattar Al-Kabi, Aboozar Mosleh, Yiyin Zhou, Bader Alharthi, Wei Du, Joe Margetis, John Tolle, Andrian Kuchuk, Mourad Benamara, Baohua Li, Hameed Naseem, Mansour Mortazavi, and Shui-Qing Yu, Structural and Optical Characteristics of GeSn Quantum Wells for Silicon-Based Mid-Infrared Optoelectronic Applications, Journal of Electronic Materials (2016), 10.1007/s11664-016-5031-2.
13. Yiyin Zhou, **Wei Dou**, Wei Du, Thach Pham, Seyed Amir Ghetmiri, Sattar Al-Kabi, Aboozar Mosleh, Joe Margetis, John Tolle, Greg Sun, Richard Soref, Baohua Li, Mansour Mortazavi,

Hameed Naseem, and Shui-Qing Yu, Systematic study of Si-based GeSn light-emitting diodes towards mid-infrared applications, *Journal of Applied Physics* 120, 023102 (2016)

14. A. Mosleh, M. Alher, L. C. Cousar, W. Du, S. A. Ghetmiri, S. Al-Kabi, **Wei Dou**, P. C. Grant, G. Sun, R. A. Soref, B. Li, H. A. Naseem, and S.-Q. Yu, Buffer-free GeSn and SiGeSn growth on Si substrate using in-situ SnD<sub>4</sub> gas mixing, *J. Electron. Mater.*, April 2016, Volume 45, Issue 4, pp 2051-2058.
15. A. Mosleh, M. Alher, W. Du, L. C. Cousar, S. A. Ghetmiri, S. Al-Kabi, **Wei Dou**, P. C. Grant, G. Sun, R. A. Soref, B. Li, H. A. Naseem, and S.-Q. Yu, Si<sub>y</sub>Ge<sub>1-x-y</sub>Sn<sub>x</sub> films grown on Si using a cold-wall ultrahigh-vacuum chemical vapor deposition system, *J. Vac. Sci. Technol. B*, 34, 011201 (2016). Selected as the editor's pick and the most read paper in the month.
16. A. Mosleh, M. Alher, L. Cousar, H. Abu-safe, **Wei Dou**, P. C. Grant, S. Al-Kabi, S. A. Ghetmiri, B. Alharthi, H. Tran, W. Du, M. Benamara, B. Li, M. Mortazavi, S.-Q. Yu, and H. Naseem, Enhancement of Material Quality of (Si)GeSn Films Grown By SnCl<sub>4</sub> Precursor, *ECS Transactions*, 69 (5) 279-286 (2015).
17. M. Alher, A. Mosleh, L. Cousar, **Wei Dou**, P. C. Grant, S. A. Ghetmiri, S. Al-Kabi, W. Du, M. Benamara, B. Li, M. Mortazavi, S.-Q. Yu, and H. A. Naseem, CMOS Compatible Growth of High Quality Ge, SiGe and SiGeSn for Photonic Device Applications, *ECS Transactions*, 69 (5) 269-278 (2015).
18. S. Al-Kabi, S. A. Ghetmiri, J. Margetis, W. Du, A. Mosleh, M. Alher, **Wei Dou**, G. Sun, R. A. Soref, J. Tolle, B. Li, M. Mortazavi, H. A. Naseem, and S.-Q. Yu, Optical characterization of Si-based Ge<sub>1-x</sub>Sn<sub>x</sub> alloys with Sn compositions up to 12%, *J. Electron. Mater.*, 1-9, DOI: 10.1007/s11664-015-4283-6 (2015). Selected as editor's pick.

## F.2 List of conference proceedings and publications

1. **Wei Dou**, Yiyin Zhou, Joe Margetis, Wei Du, Jifeng Liu, Greg Sun, Richard A. Soref, John Tolle, Baohua Li, Mansour Mortazavi, and Shui-Qing Yu, "Optically Pumped GeSn-edge-emitting Laser with Emission at 3 μm for Si Photonics", accepted by Lasers and Electro-Optics (CLEO), 2017 Conference.
2. Margetis, Joe, John Tolle, Wei Du, Seyed Ghetmiri, Mansour Mortazavi, Sattar Al-Kabi, Yiyin Zhou **Wei Dou** et al. "GeSn-based light sources and photoconductors towards integrated photonics for the mid-infrared." In Photonics Society Summer Topical Meeting Series (SUM), 2017 IEEE, pp. 13-14. IEEE, 2017
3. Du, Wei, Seyed Ghetmiri, Sattar H. Al-Kabi, Joe Margetis, Yiyin Zhou, **Wei Dou**, Aboozar Mosleh et al. "Study of SiGeSn/GeSn/SiGeSn quantum well towards all group-IV-optoelectronics." In CLEO: Science and Innovations, pp. STh3I-3. Optical Society of America, 2017.

4. Al-Kabi, Sattar, Seyed Amir Ghetmiri, Joe Margetis, Thach Pham, Yiyin Zhou, **Wei Dou**, Wei Du et al. "Optically pumped Si-based edge-emitting GeSn laser." In Lasers and Electro-Optics (CLEO), 2017 Conference on, pp. 1-2. IEEE, 2017.
5. Zhou, Yiyin, Wei Du, **Wei Dou**, Thach Pham, Aboozar Mosleh, Seyed Amir Ghetmiri, Sattar Al-Kabi et al. "Systematic study of Si-based Ge<sub>0.9</sub>Sn<sub>0.1</sub> light-emitting diodes towards mid-infrared application." In Lasers and Electro-Optics (CLEO), 2016 Conference on, pp. 1-2. IEEE, 2016.
6. **Wei Dou**, Seyed Ghetmiri, Sattar Al-Kabi, Aboozar Mosleh, Yiyin Zhou, Wei Du, Joe Margetis, John Tolle, Andrian Kuchuk, Mourad Benamara, Baohua Li, Hameed A. Naseem, Mansour Mortazavi, Shui-Qing Yu, "Study of CVD Grown Pseudomorphic GeSn/GeSn and SiGeSn/GeSn Quantum Well", accepted by 58th Electronic Material Conference (EMC 2016).
7. Sattar Al-Kabi, Seyed Amir Ghetmiri, Joe Margetis, Wei Du, Aboozar Mosleh, **Wei Dou**, Greg Sun, Richard A. Soref, John Tolle, Baohua Li, Mansour Mortazavi, Hameed A. Naseem, Shui-Qing Yu, "High Quality CVD Grown Thick GeSn Samples with Enhanced Photoluminescence Intensity", accepted by 58th Electronic Material Conference (EMC 2016).
8. P.C. Grant, **W. Dou**, D. Fan, Y.I. Mazur, V.G. Dorogan, S.-Q. Yu, G.J. Salamo, "Band offsets in GaAs<sub>1-x</sub>Bi<sub>x</sub>/GaAs", accepted by 18th International Conference on Molecular Beam Epitaxy (MBE 2014).